



Western Washington University
Western CEDAR

WWU Graduate School Collection

WWU Graduate and Undergraduate Scholarship

2011

Glacial and geothermal dynamics in Sherman Crater, Mount Baker, Washington

Melissa Park
Western Washington University

Follow this and additional works at: <https://cedar.wwu.edu/wwuet>

 Part of the [Geology Commons](#)

Recommended Citation

Park, Melissa, "Glacial and geothermal dynamics in Sherman Crater, Mount Baker, Washington" (2011).
WWU Graduate School Collection. 139.
<https://cedar.wwu.edu/wwuet/139>

This Masters Thesis is brought to you for free and open access by the WWU Graduate and Undergraduate Scholarship at Western CEDAR. It has been accepted for inclusion in WWU Graduate School Collection by an authorized administrator of Western CEDAR. For more information, please contact westerncedar@wwu.edu.

Glacial and geothermal dynamics in Sherman Crater, Mount Baker, Washington

By
Melissa Park

Accepted in Partial Completion
Of the Requirements for the Degree
Master of Science

Moheb A. Ghali, Dean of the Graduate School

ADVISORY COMMITTEE

Chair, Dr. Douglas H. Clark

Dr. Jackie Caplan-Auerbach

Dr. Bernard Housen

MASTER'S THESIS

In presenting this thesis in partial fulfillment of the requirements for a master's degree at Western Washington University, I grant to Western Washington University the non-exclusive royalty-free right to archive, reproduce, distribute, and display the thesis in any and all forms, including electronic format, via any digital library mechanisms maintained by WWU.

I represent and warrant this is my original work, and does not infringe or violate any rights of others. I warrant that I have obtained written permissions from the owner of any third party copyrighted material included in these files.

I acknowledge that I retain ownership rights to the copyright of this work, including but not limited to the right to use all or part of this work in future works, such as articles or books.

Library users are granted permission for individual, research and non-commercial reproduction of this work for educational purposes only. Any further digital posting of this document requires specific permission from the author.

Any copying or publication of this thesis for commercial purposes, or for financial gain, is not allowed without my written permission.

Signature: _____

Date: _____

Glacial and geothermal dynamics in Sherman Crater,
Mount Baker, Washington

A Thesis
Presented to
The Faculty of
Western Washington University

In Partial Fulfillment
Of the Requirements for the Degree
Master of Science

By
Melissa Park
June 2011

ABSTRACT

Although quiescent since a significant thermal event in 1975, Mount Baker, in Washington, continues degassing from fumaroles in Sherman Crater, indicating the presence of a connection to an active magmatic system at depth. The apparent equilibrium condition of the crater glacier between 2003 and 2008, despite lying well above the regional equilibrium line altitude, suggests that melting of basal ice by heat flux from fumaroles and heated ground must balance the glacier's positive surface mass-balance.

My investigation of glacial and geothermal dynamics in Sherman Crater between 2009 and 2010 provides the first rigorous quantitative assessment of the Sherman Crater glacier: ice volume, flow direction and velocity, annual mass balance and characteristics of the material below its base. Heat flux is derived from these constraints by two methods: the glacier calorimetry method of Welch et al. (2007) and the thermal grounds method of Frank et al. (1977).

Ground-Penetrating Radar (GPR) transects across the crater glacier yield a maximum ice thickness of ~ 40 m W.E. and volume of ~ 1.3 million m^3 W.E. for 2009 and ~ 66 m W.E. and volume of ~ 2.1 million m^3 W.E. for 2010, assuming a standard velocity of EM-waves through ice of 0.151 m/ns and an average ice density of 700 kg/m^3 . The measured annual mass balance in 2009 of ~ 4.0 m of snow and ice and derived heat flux range of ~ 18 to ~ 28 W/m^2 are comparable to values at active but quiescent volcanoes. The glacier flows northward at a rate of ~ 3 cm/day and rests on a base of hydrothermally altered regolith with thin meltwater layers.

Because the glacier's total volume in 2009 is $\sim 2/3$ of the inferred volume of ice melted during the 1975 unrest event (which did not produce a debris flow), the risk from meltwater-induced debris flow from Sherman Crater is low. The large fluctuation in calculated glacier volume between 2009 and 2010, however, highlights the potential for this situation to change rapidly. An increase in annual-mass balance or decrease in heat flux could affect both ice volume and the distribution of thermally exposed surfaces in the crater. The present glacier mass-gradient driving the flow of ice northward towards large areas of thermally exposed ground could be overwhelmed by an eastward directed mass-gradient, towards the East Breach, a source of debris flows since the mid-Holocene. Sherman Crater might therefore become more of a threat if volcanic activity subsides.

ACKNOWLEDGEMENTS

I would like to thank my adviser, Dr. Douglas Clark, for providing me with guidance and encouragements on such a unique and interesting project. Thanks to my committee members, Dr. Jackie Caplan-Auerbach and Dr. Bernard Housen, for their support, patience and insightful reviews.

I would like to thank the following organizations for providing funding for this research: the National Science Foundation, the Geological Society of America, Western Washington University Department of Geology and Western Washington University Graduate School.

I would like to thank Dave Tucker of the Mount Baker Volcano Research Center (MBVRC) for his assistance with fieldwork logistics and generously shared intimate knowledge of Mount Baker, David Frank and Gene Kiver for demystifying published articles related to Sherman Crater's 1975 unrest event, Brendan Hodge for introducing me to the joys of fieldwork on Mount Baker, John Scurlock for reconnaissance flights and on-demand aerial photographs of the crater, Graham Clark for lending me his ArcGIS skills, everyone at Geophysical Survey Systems, Inc. (GSSI) for detailed answers to my many questions about ground penetrating radar and Radan 6.0, the University of Minnesota for lending me a quiet space in which to write the final draft of this thesis and the Northwest Riders for providing my spring fieldwork team with fast and safe snowmobile transportation to Sherman Crater.

I am also indebted and forever grateful to my field assistants, who willingly and enthusiastically carried heavy equipment across treacherous crevasse fields, up a tall mountain and into the toxic fumes of Sherman Crater: Lauren Hogan, Evan Larsell, Neil Bush, Nicole Boweman, Stephen Veitch, Ben Baugh, Brendan Hodge, Maija Robinson, Aaron Fitts, Levi Gose, Nigel Davies, Brendan Raftery, Jim Fitzpatrick, Dacia Grayber, Keith Kemplin, Doug McKeever, Mike Ruark, Leesa Duncan, to name but a few.

Last, but not least, I thank my friends and fellow students, graduate and undergraduate, for the support and encouragements they have provided during this project and for balancing my scientific life with a healthy dose of outdoor adventures. I could not have done it without you.

TABLE OF CONTENTS

| | |
|---|----|
| Abstract | iv |
| Acknowledgements | v |
| List of Figures..... | ix |
| List of Tables..... | x |
| Introduction..... | 1 |
| 1.1 - Geologic background | 1 |
| 1.2 - Sherman Crater | 2 |
| 1.2.1 - Pre-1975 | 2 |
| 1.2.2 - The 1975 unrest event..... | 3 |
| 1.2.3 - Sherman Crater today | 4 |
| 1.3 - Previous studies of ice-volcano interaction in craters and calderas | 5 |
| 1.3.1 - Welch et al.'s (2007) calorimetry model | 6 |
| 1.3.2 - Frank et al.'s (1977) thermal surface area method..... | 7 |
| 2 - Data collection and data processing..... | 16 |
| 2.1 - Data collection | 16 |
| 2.1.1 - Glacier mass balance and motion..... | 16 |
| 2.1.2 - Ground-penetrating Radar (GPR) | 17 |
| 2.1.3 - Global positioning system (GPS) and altitude measurements | 19 |
| 2.2 - Data processing..... | 19 |
| 2.2.1 - Glacier mass balance and motion..... | 19 |
| 2.2.2 - GPS points processing | 20 |
| 2.2.3 - GPR CMP data analysis..... | 20 |
| 2.2.4 - GPR reflection profiling data analysis | 21 |
| 2.2.5 - Glacier characteristics - maps and calculations..... | 23 |
| 2.3 - Heat flux calculations methods..... | 24 |
| 2.3.1 - Glacier crater calorimetry (The Welch model)..... | 24 |
| 2.3.2 - Thermal areas model (The Frank model) | 25 |
| 3 - Field data | 38 |
| 3.1 - Ablation stakes | 38 |
| 3.1.1 - Accumulation | 38 |
| 3.1.2 - Ablation..... | 38 |

| | |
|--|----|
| 3.1.3 – glacier flow..... | 39 |
| 3.2 – GPS data - Surface topography of glacier | 39 |
| 3.3 – Profiling GPR data – signal character..... | 39 |
| 3.3.1 – Basal and englacial reflectors..... | 40 |
| 3.3.2 – Interference signals..... | 40 |
| 3.4 – CMP GPR data – EM wave velocity | 41 |
| 4 – Crater and crater glacier characteristics | 50 |
| 4.1 – Maximum depth, glacier area and ice volume..... | 50 |
| 4.1.1 – maximum depth..... | 50 |
| 4.1.2 – glacier surface area..... | 50 |
| 4.1.3 – Ice volume | 51 |
| 4.2 – Annual mass balance | 51 |
| 4.3 – Basal and englacial reflectors..... | 51 |
| 4.3.1 – Basal reflectors..... | 51 |
| 4.3.2 – Englacial reflectors | 52 |
| 4.3.3 – Interference signals..... | 53 |
| 4.4 – Heat Flux | 54 |
| 4.4.1 – Geothermal ground inventory | 54 |
| 4.4.2 – Heat flux calculations..... | 55 |
| 4.5 – Ice flow..... | 56 |
| 5 - Discussion | 66 |
| 5.1 – Ice motion..... | 66 |
| 5.1.1 – Total station measurement uncertainties..... | 66 |
| 5.1.2 – Ice velocity compared to other glaciers | 67 |
| 5.2 – Ice depth and glacier volume | 67 |
| 5.2.1 – GPR time-to-depth conversions | 67 |
| 5.2.2 – Weather considerations | 68 |
| 5.2.3 – Ice density considerations..... | 69 |
| 5.2.4 – Volume comparisons | 70 |
| 5.2.5 – Recommendations for more accurate volume estimates | 71 |
| 5.3 – Mass balance | 71 |
| 5.3.1 – Comparable accumulation and ablation rates..... | 71 |
| 5.3.2 – Weather considerations | 73 |

| | |
|--|----|
| 5.3.3 – Recommendations for more accurate mass balance estimates | 73 |
| 5.4 – Heat flux | 74 |
| 5.4.1 – Alternate calculations and comparable volcanoes | 74 |
| 5.4.2 – Using the Welch et al. (2007) method – validity of assumptions..... | 76 |
| 5.4.3 – Using the Frank et al. (1977) METHOD – validity of assumptions | 77 |
| 5.4.4 – Recommendations for more accurate heat flux calculations..... | 77 |
| 5.5 – Implications..... | 78 |
| 5.5.1 – Glacier characteristics | 78 |
| 5.5.2 – Heat flux | 79 |
| 6 - Conclusions..... | 83 |
| References | 86 |
| Appendix A - Crater glacier volume using a paraboloid approximation | i |

LIST OF FIGURES

| | |
|---|----|
| Figure 1. 1 – Location of Mount Baker within the Cascade Volcanic Belt | 9 |
| Figure 1. 2 – Photograph of Mount baker, Sherman Crater and Grant Peak..... | 10 |
| Figure 1. 3 – Map of thermal areas in Sherman Crater from 1908 to 1975 | 11 |
| Figure 1. 4 – Comparative aerial photographs from 2006 and 1975..... | 12 |
| Figure 1. 5 – Aerial photographs of Sherman Crater during the 1975 unrest event..... | 13 |
| Figure 1. 6 – Annotated aerial photograph of Sherman Crater in 2007 | 14 |
| Figure 1. 7 – Sketch of expected ice flow based on observed glacier surface topography..... | 15 |
| | |
| Figure 2. 1 – Map of locations of ablation stakes in May and August 2009 | 27 |
| Figure 2. 2 – Sketch of ground penetrating radar (GPR) setup | 28 |
| Figure 2. 3 – Map of GPR survey lines in 2009 and 2010..... | 29 |
| Figure 2. 4 – Map of Global Positioning System (GPS) waypoints collected in 2010 | 30 |
| Figure 2. 5 – GPR CMP data record..... | 31 |
| Figure 2. 6 – Example of GPR profile before and after processing..... | 33 |
| Figure 2. 7 – Example of depth pick processing..... | 35 |
| Figure 2. 8 – Ice thickness map | 36 |
| Figure 2. 9 – Map of thermal grounds in Sherman Crater in 2009 | 37 |
| | |
| Figure 3. 1 – Ablation stake inventory..... | 43 |
| Figure 3. 2 – Ablation stakes movement and modeled ice motion | 44 |
| Figure 3. 3 – Surface topography generated from GPS waypoints..... | 45 |
| Figure 3. 4 – reflector types in original data | 46 |
| Figure 3. 5 – Distribution of reflector types along 2010 GPR transects..... | 48 |
| Figure 3. 6 – Examples of interference signals..... | 49 |
| | |
| Figure 4. 1 - Ice thickness contour map | 61 |
| Figure 4. 2 - Example of englacial reflectors in GPR profiles..... | 62 |
| Figure 4. 3 - Oblique aerial photograph of thermal zones of type A..... | 63 |
| Figure 4. 4 - Thermal zones inventory: Types A, B and C | 64 |
| Figure 4. 5 - Ice flow vector map..... | 65 |
| | |
| Figure 5. 1 – Snow water equivalent accumulation for Mount Baker | 81 |
| Figure 5. 2 – Glacier surface areas in 1972 and 2009..... | 82 |

LIST OF TABLES

| | |
|---|----|
| Table 3. 1 – Summary of ablation stakes and total station data..... | 42 |
| Table 4. 1 – Summary of glacier characteristics | 58 |
| Table 4. 2 – Heat flux calculations using the method of Frank et al. (1977) | 59 |
| Table 4. 3 – Heat flux calculations using the method of Welch et al. (2007) | 60 |

INTRODUCTION

Regular monitoring of heat flux from active but quiescent volcanoes is important both in understanding the evolution of magmatic processes in the interim between potential unrest or explosive events (Dehn et al., 2000) and in identifying changes in heat flux related to renewed activity (Delle-Donne et al., 2010).

Mount Baker, in the Cascades of northwest Washington, is classified as a “Very High Threat Volcano” by the US Geologic Survey (Ewert et al., 2005). Volcanoes in this category require the highest monitoring level (Ewert et al., 2005). Although it is currently quiescent and has been since the unrest event of 1975, recent gravity, deformation, seismic and gas studies suggest the presence of an active magmatic system at depth (Crider et al., 2011). The most recent estimate for the heat flux emanating from Sherman Crater, however, was published by Frank et al. (1977). In order to quantify potential changes in heat flux associated with changes in the magmatic and hydrothermal system or with renewed activity, knowledge of more recent background behavior is essential.

Here I present the results of a geophysical study of Sherman Crater, the main goals of which were to characterize the crater glacier’s dimensions, volume, and behavior and to estimate the heat flux based on these characteristics. Using a combination of ground-penetrating radar surveys and traditional glaciological methods, I determine the crater glacier’s ice volume, depth, and flow direction and the crater’s subglacial topography and character. I estimate the heat flux in the crater based on these constraints using the glacier calorimetry model of Welch et al. (2007), a model developed for large calderas. I assess the applicability of this model by comparing my results to heat flux calculated using a method based on extent and intensity of thermal areas, previously used at Sherman Crater (Frank et al., 1977). My research therefore provides a case-study in the application and adaptation of a calorimetric-based model to small ice-filled volcanic craters.

1.1 - GEOLOGIC BACKGROUND

Ice-mantled Mount Baker, the most recent stratocone in the Mount Baker Volcanic Field (MBVF) (Hildreth et al., 2003), is one of several stratovolcanoes in the Cascade Volcanic Belt (CVB) (Tabor et al., 2003; Figure 1.1). Located 50 km east of Bellingham, Washington, and 25 km south of the US-Canadian international border, the distinctive 3286 meter high edifice and its occasional steam plumes can be seen from southwestern British Columbia to the Puget lowlands.

The CVB results from oblique subduction of the oceanic Juan de Fuca plate under the North American plate along the Cascadia Subduction Zone (Tabor et al., 2003; Figure 1.1). The MBVF was built on a basement of Mesozoic and Paleozoic rocks accreted as terranes during the Cretaceous, then displaced and metamorphosed during the Paleogene (Tabor et al, 2003). The MBVF has been intermittently active for 1.3 Ma (Hildreth et al., 2003) and includes the 1.15 Ma Kulshan Caldera, the remnants of the 0.5-0.3 Ma Black Buttes Volcano and the currently active Mount Baker. Older volcanic edifices were largely eroded by the repeated ice-sheet incursions from British Columbia during the Pleistocene (Hildreth et al., 2003).

Most of the modern Mount Baker edifice was built after 40,000 yr B.P. and much of the upper cone is younger than ca. 20,000 yr B.P (Hildreth et al., 2003). Based on tephra deposits, Tucker et al. (2007) identified four major eruptive episodes: The Carmelo Crater eruptive period (ca. 15,000-12,200 yr B.P.), during which the summit crater, now filled with ice, produced lava flows, block-and-ash pyroclastic flows and lahars, the Shriebers Meadow eruptive period (ca. 8850-8500 yr B.P), characterized by the eruption of a cinder cone near the southern base of the mountain and a later lahar from the nearby slope of Mount Baker, the Mazama Park eruptive period (ca. 5930-5740 yr B.P.), with its flank collapses leading to the Middle Fork and Ridley Creek lahars, and the Sherman Crater eruptive period (A.D. 1843 to present).

1.2 - SHERMAN CRATER

1.2.1 - *PRE-1975*

Sherman Crater, about 400 meters lower than and 800 meters south of the summit of Mount Baker (Figure 1.2), has been the site of intense hydrothermal activity and the source of debris flows through collapse of the eastern rim since at least the mid-Holocene (Hyde and Crandell, 1978; Scott et al., 2003). The 600 meter wide crater was enlarged by a hydrothermal explosion in 1843 (Hildreth et al., 2003; Tucker et al., 2007). Following the 1843 event, Sherman Crater remained the site of hydrothermal activity (Kiver, 1978 and references therein). Several minor eruptions were reported, but these reports were based on sea-level observations of “smoke” emanating from the crater, which could have been the result of normal fumarolic activity (Kiver, 1978). Deposits reveal at least two debris flows generated by the collapse of the eastern rim of Sherman Crater (Tucker et al., 2007), an area that remains fragile today. By 1891, Sherman Crater was filled with ice (Kiver, 1978). Vertical aerial photographs of Sherman Crater were taken from the early 1940s. Early photographs reveal fumarole vents and ice cave entrances along the west and northwest rim. The

largest fumarole, the “Old Main Fumarole”, created a pit ~35 meters deep near the East Breach (Kiver, 1978) and ice cave passages were estimated at 1200 meters in total length (Kiver, 1978). The period between 1940 and 1974 saw a gradual shift in fumarole locations and the appearance of new fumaroles (Frank et al., 1977; Figure 1.3). Observations of additional snow free area between subsequent surveys suggest a gradually increasing heat flux from the 1940s until the thermal event of 1975 (Frank et al., 1977). Thermal activity in the crater between 1940 and 1974 remained located mainly along the west and northwest rim and near the East Breach. A new fumarole pit appeared in the southwest portion of the crater between 1960 and 1963 (Kiver, 1978). This so-called “southwest pit” was originally measured to be 46 meters deep and 32 meters wide (Kiver, 1978). This fumarole pit is still present, although it has migrated eastward since its first appearance. It is referred to as the “Dragon Hole” in this study and was used as an end point for several Ground-Penetrating Radar survey lines.

1.2.2 – THE 1975 UNREST EVENT

In March 1975, Sherman Crater became the site of a considerable increase in thermal activity. Unusually high dark vapor plumes were first reported on March 10th, generating concerns of an imminent eruption. Three new clusters of fumaroles appeared and the area occupied by preexisting fumarole fields expanded significantly (Frank et al., 1977). Ice that was previously smooth became heavily crevassed and a lake of boiling water formed near the East Breach (Easterbrook, 1975; Figures 1.4 and 1.5). By September, roughly half of the crater ice had melted (from 2.2-2.7 million m³ before 1975 to 1.2-1.7 in 1975; Frank et al., 1977). Calculations by Frank et al. (1977) indicate that these changes represented an order of magnitude increase in the rate of heat flow in the crater (from 7-11 MW/m² pre-1975 to 150-200 MW/m² in 1975, averaged over the entire crater). The increase in the rate of heat flow was accompanied by a doubling in the concentration of CO₂ and a 1000-fold increase in the concentration of H₂S emitted (Kiver, 1978). Whereas the maximum fumarole temperature recorded in 1974 was ~90° C (the boiling point of water at the crater’s altitude), 1975 saw the appearance of super-heated fumaroles (~130° C) (Kiver, 1978), particularly in the central area of the crater (Frank et al., 1977), an area now apparently inactive at the surface. Petrographic analysis of ejecta collected on glaciers surrounding the crater revealed the absence of constituents characteristic of fresh magma. The ejected tephra was simply hydrothermally altered debris torn from the walls of the fumaroles (Frank et al., 1977). A review of geophysical and geochemical studies of Sherman Crater over the past 30 years, however, indicates that the thermal unrest of 1975 was in fact the manifestation of the release of volatiles due to the opening of a conduit to a deep magmatic source (Crider et al., 2011).

In response to Sherman Crater's thermal increase, the U.S. Geological Survey (USGS) closed the Boulder Creek drainage area and the shorelines of Baker Lake to the public, drew down the water level in Baker Lake to accommodate potential debris flows and launched an interdisciplinary survey of the crater that included seismic, tilt, gravity, gas, hydrologic, petrographic, thermal infrared and photographic studies. No significant deformation of the edifice was detected (Frank et al., 1977), only one small ($\sim 1 M_L$) earthquake was recorded (Frank et al., 1977) and although a slight decrease in gravity was measured at Sherman Crater (~ 0.33 mgal; Malone, 1979), the interpretation of this decrease was ambiguous due to the lack of geodetic constraints on the crater (Hodge and Crider, 2010). Researchers concluded that the probability of an imminent eruption or debris flow had decreased to background level by 1976 (Frank et al., 1977). The water level in the Baker Lake reservoir was raised back to normal and previously closed areas were reopened to the public, but extensive instrument monitoring of Mount Baker continued until 1980, when volcanic attentions were diverted to erupting Mount St. Helens.

1.2.3 - SHERMAN CRATER TODAY

Although Mount Baker is currently quiescent, Sherman Crater remains active, with constant CO_2 and H_2S degassing from active thermal areas (Werner et al., 2009) and an occasional visible gas plume. The crater glacier surface appears relatively smooth in most years, with minimal crevassing and virtually unchanging thermal features from year to year. In the winter-time, Sherman Crater is almost completely covered in snow; bare areas due to heated ground or fumarole pits occur in the East Breach Pit and in several locations in both the West Rim Fumarole Field (WRFF) and the Northwest Fumarole Field (NWFF; Figure 1.6). Summertime snow-free areas resulting from thermal activity are the WRFF, the NWFF including the West Rim Pit, the East Breach Pit the Dragon Hole (Figure 1.6). The glacier's surface topography and direction of ice extension indicated by crevasse patterns suggest that the ice that accumulates in the crater should flow generally towards the East Breach on the southwest side of the ridge below Pooch Peak and towards the Northwestern Fumarole Field on the northeast side of that ridge (Figure 1.7). Ice does not exit the crater through the East Breach. Meltwater from Sherman Crater during the 1975 thermal event, however, drained out of the crater and beneath the Boulder Glacier based on tracking with tracer dye (Frank, 1975). Although Sherman Crater, at an altitude of 2900 meters, lies entirely above Mount Baker's equilibrium line altitude (~ 2050 m on Easton Glacier as measured by Pelto and Hartzell (2004); 2155 m on Deming Glacier as estimated by Kovanen and Slaymaker (2005)) the volume of ice contained in the crater appears to be in steady state: the extent of ice observable in

Sherman Crater appears to have changed little relative to the crater rim in aerial photographs taken in mid-summer between 2003 and 2008 (2009 and 2010 were exceptional years).

Despite its apparent quiescent demeanor, Mount Baker was classified by the USGS as a “very high threat volcano” because of its recent unrest and proximity to reservoirs and population centers (Ewert et al., 2005). Ewert et al. (2005) suggest that priority for the expansion of volcano monitoring networks should go to volcanoes in this category. In recent years, the mountain has seen a revival of investigations, including seismic, gravity, gas and geodetic studies (Caplan-Auerbach et al., 2007; Crider et al., 2008; Werner et al., 2009 and Hodge and Crider, 2010). Hodge and Crider’s (2010) geodetic survey of Mount Baker revealed significant surface shortening around the edifice in the past quarter century, particularly on the northern flank of the volcano (<2 mm/yr). Modeling of these data suggests the shortening is due to degassing of a deep magma body (Hodge and Crider, 2010). This interpretation is consistent with the results of gravity (Crider et al., 2008) and gas geochemistry (Werner et al., 2009) studies. Initial thermal unrest due to opening of a new conduit to a deep magma body followed by redistribution of mass and continued degassing within the active hydrothermal system beneath Mount Baker could explain the shortening observed (Hodge and Crider, 2010), the 1800 ± 300 μgal gravitational decrease measured (Crider et al., 2008) and the long, steady trend away from a magmatic signature towards a hydrothermally generated one (Werner et al., 2009). Although Mount Baker has not exhibited high levels of seismicity since monitoring first was initiated, the period from June to September 2009 saw a cluster of shallow low frequency earthquakes centered on the southern flanks of the volcano (Caplan-Auerbach et al., 2009). Whether these seismic events are related to the flow of the Deming Glacier or to movement of fluid at depth still remains to be determined (Caplan-Auerbach et al., 2009). This study complements recent geochemical and geophysical investigations with calculations of heat flux in Sherman Crater and a description of the character and features of the crater glacier.

1.3 - PREVIOUS STUDIES OF ICE-VOLCANO INTERACTION IN CRATERS AND CALDERAS

Ice-volcano interactions in large, active calderas have been studied in Iceland, Alaska and Kamchatka (e.g., Clark et al., 1989; Salamatina et al., 2000; Welch et al., 2007, Guðmundsson et al., 2007). Although I considered several models relating glacier characteristics to heat flux developed for larger calderas, most of these theoretical models seemed inappropriate for the particular setting of Sherman Crater. One-dimensional flow models such as the one developed by Nye (1952) and adapted by Clark et al. (1989) assume the effects of side-walls to be negligible. This is an invalid

assumption in the case of Sherman Crater glacier, which is confined by the crater rim on all sides (Figure 1.6). Other models, such as the thermomechanically coupled model developed by Salamatin et al. (2000) require input parameters that are beyond the scope of this study (e.g., ice temperature, pressure at depth, shear stresses, etc.). These missing parameters would have to be either estimated or derived from the literature, negating the advantages of using this more comprehensive model. The Welch et al. (2007) model developed for the intra-caldera icefield of Mount Veniaminof, Alaska, however, seems well suited to Sherman Crater because of its assumption of a closed glacial system and its use of a simplified list of input parameters. Despite the considerable scale difference (Mount Veniaminof's caldera is 800 km² (Welch et al., 2007); Sherman Crater only 0.1 km²), the caldera on Mount Veniaminof presents a situation more similar to Sherman Crater in its heat flux distribution than other inactive or lake-filled calderas: it is mostly covered in ice, except for one active cinder cone surrounded by active fumaroles (Welch et al., 2007). To assess the applicability of Welch et al.'s (2007) calorimetric model for Sherman Crater, I also calculate the modern heat flux in Sherman Crater following the method used by Frank et al. (1977).

1.3.1 – WELCH ET AL.'S (2007) CALORIMETRY MODEL

The Welch et al. (2007) survey of the intra-caldera icefield of Mount Veniaminof, Alaska, was conducted using a 8 MHz deep-penetrating radio-echo sounding (RES) and synchronous global positioning system (GPS) measurements (a pair of altimeter-equipped, WAAS (Wide Area Augmentation System)-enabled, consumer-grade GPS). They collected data along several transects in a roughly radial pattern across the icefield. Post-processing of the radar data included the application of a bandpass filter (between 5 and 15 MHz) to remove ambient and system noise, a normal move-out correction to accommodate the constant 60m antenna separation and data migration. Welch et al. (2007) used a standard value of 0.169 m/ns for the velocity of EM waves traveling in ice. They calibrated the rate of accumulation assuming that internal reflectors revealed by the radar survey were isochronal deposits from known local eruptions. Bedrock reflectors and prominent internal layers in GPR profiles were digitized to generate maps of bedrock topography, ice thickness and extent of ash deposits. Welch et al. (2007) then applied basic glacier calorimetry to determine the heat flux. They assumed that the entire ice-thickness (determined from the radar survey) is at the pressure melting point, that all geothermal heat goes into melting ice (negligible loss through vents or otherwise) and that the steady-state equilibrium maintained in the caldera is achieved through exact melting of the glacier's mass-balance. The melt-rate is therefore simply the

annual mass-balance divided by the seconds in a year and the heat flux is this melt rate times the latent heat of fusion for ice.

The calorimetry model presented by Welch et al. (2007) relies on basic physics and on only one field-gathered input parameter: the glacier's annual mass-balance. Differences between the caldera of Mount Veniaminof and Sherman Crater, however, result in difficulties when adapting the method to Sherman Crater. Welch et al. (2007) determined the annual-mass balance by measuring the thickness of ice layers in GPR profiles. No further adjustment was necessary: ice layers represent the full accumulation and ablation seasons and at depth, they are already compacted. Unfortunately, no ash or other distinctive annual layers are present in the Sherman Crater glacier to calibrate the rate of accumulation. Instead, I evaluated the annual mass-balance the traditional way, by subtracting measured surface melting at the end of the summer from measured thickness of new snow measured at the end of the snow season. Because accumulation and ablation data were gathered at the surface of the glacier (lower density) and do not represent the full accumulation and ablation seasons for 2009, the derived annual mass-balance contains a greater level of uncertainty than Welch et al.'s (2007) values.

Although both Sherman Crater and the Veniaminof caldera contain a glacier and fumaroles venting to the air, the glacier inside the caldera of Mount Veniaminof extends from rim to rim and fumaroles create pits only around the active cinder cone (Welch et al., 2007). In Sherman Crater, fumaroles not only create pits in the glacier but also form large bare-ground areas: the SWFF and the NWFF. The assumption that all fumarole heat goes into the melting of the ice is therefore clearly inaccurate, but to an unknown degree.

1.3.2 – FRANK ET AL.'S (1977) THERMAL SURFACE AREA METHOD

Frank et al. (1977) estimated the heat flux in Sherman Crater based on the surface area of different types of thermal fields. They categorized active areas based on nighttime infrared surveys and the change in altitude of snow-and-ice margins as melting occurred on the steeper slopes (Frank and Post, 1976). This change in altitude was determined from aerial photographs and field mapping (Frank and Post, 1976). Type A, the primary area of intense heat flux, is free of snow and ice even in winter. Type B represents areas of moderate heat flux that only become snow free in summer. The remaining area, type C, remains snow- or ice-covered all year but is subjected to thinning and crevassing due to melting at the base and local extension towards higher activity thermal areas (Frank et al., 1977).

Heat flux for thermal areas of type A was calculated using both a standard value of 419 W/m², the heat flux necessary to melt snow as it falls, up to a rate of 0.11 m W.E. per day (White, 1969), a reasonable assumption of snow fall rate for Mount Baker (Frank et al., 1977), and using the highest locally measured heat flux of 2400 W/m², measured in the Central Pit in spring 1975 (Frank et al., 1977).

For type B areas, Frank et al. (1977) calculated the rate of heat flow using the following formula:

$H = \frac{\rho D A L}{t}$ (Equation 1), where H is the rate of heat flow in MW, ρ the density of ice (600 kg/m³ for snow, 700 kg/m³ for ice and snow mix), D the thickness of the melted ice in meters, A, the area covered by this melted ice, L, the latent heat of fusion for ice (336×10^3 J/Kg) and t, the time to melt ice of thickness D in seconds. To get the average heat flux (h), this value is divided by the area covered by the type of thermal ground considered. Using this method, Frank et al., (1977) calculated an average heat-flux for Sherman Crater of 8-11 W/m² for pre-1975 and 150-200 W/m² during the 1975 thermal unrest.

Heat flux for thermal areas of type C was estimated from near-horizontal photos taken from the west rim by comparing ice level along steep crater rims below Lahar Lookout and Sherman Peak (Frank et al., 1977). For 1975 thinning was also estimated from the amount of extension revealed by the width of newly formed crevasses on the glacier (Frank et al., 1977).

I apply the Frank et al. (1977) method to present day Sherman Crater as a means to verify heat flux estimates calculated using the Welch et al. (2007) calorimetric model.

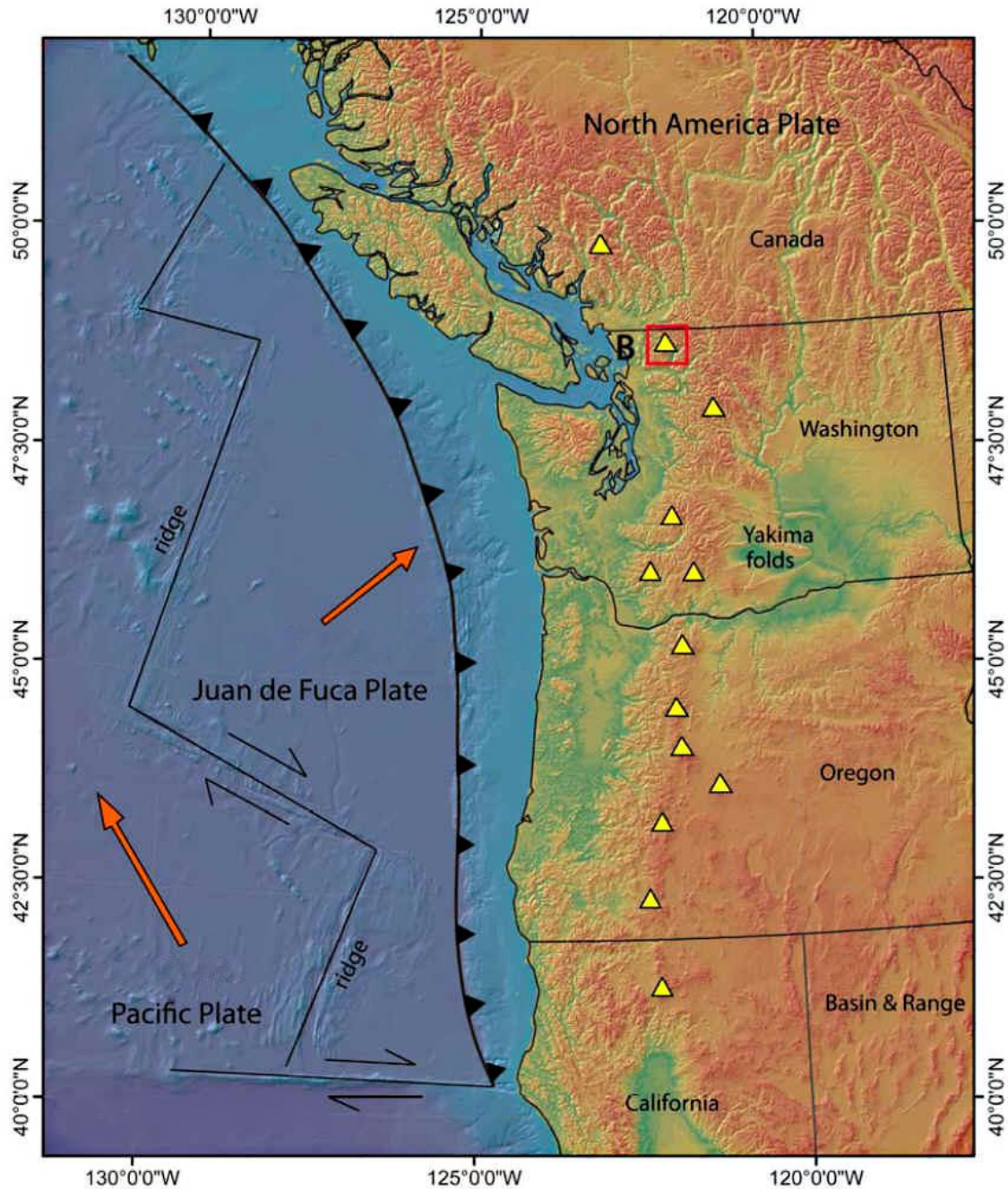


FIGURE 1. 1 - LOCATION OF MOUNT BAKER WITHIN THE CASCADE VOLCANIC BELT

Location of Mount Baker (red box) within the Cascade Volcanic Belt (yellow triangles). The CVB results from oblique convergence of the oceanic Juan de Fuca plate under the North American plate along the Cascadia Subduction Zone (marked with teeth). Mount Baker is located 50 km east of Bellingham (B), Washington and 25 km south of the US-Canadian international border. Modified from Hodge, 2008.

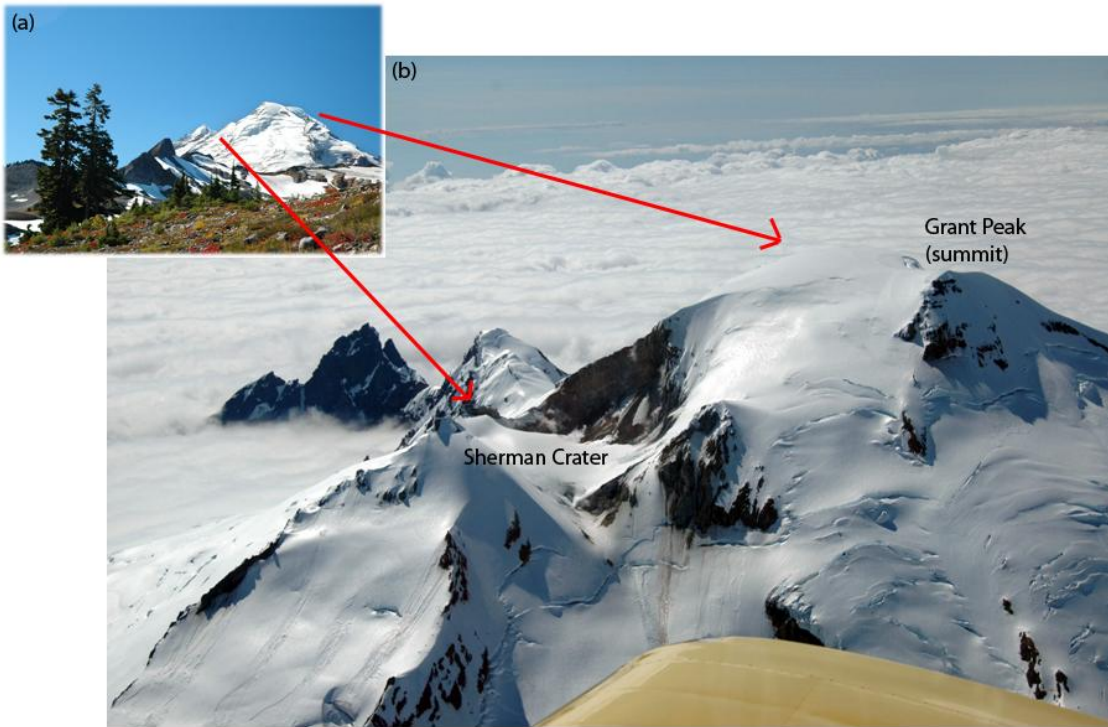


FIGURE 1. 2 – PHOTOGRAPH OF MOUNT BAKER, SHERMAN CRATER AND GRANT PEAK

(a) North-east side of Mount Baker (as viewed from Ptarmigan Ridge). (b) Looking west to the summit plateau, and Sherman Crater. Photo by Melissa Park. Insert from September 2007, crater photo from July 2010.

VOLCANIC ACTIVITY AT MOUNT BAKER, WASHINGTON

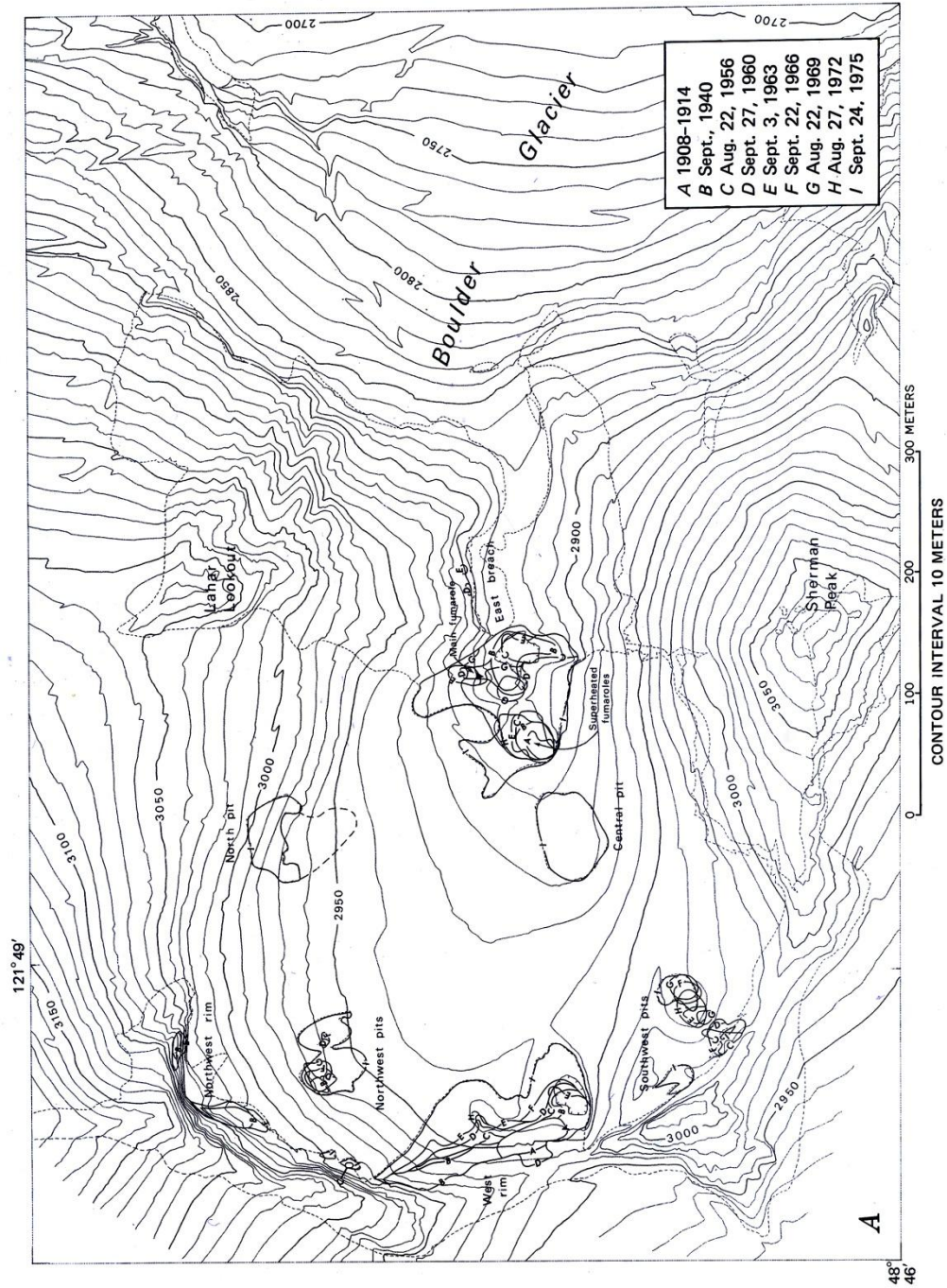


FIGURE 1.3 - MAP OF THERMAL AREAS IN SHERMAN CRATER FROM 1908 TO 1975

Thermal areas from 1908 to 1975 mapped from aerial photographs. This figure, from Frank et al., 1977, shows a gradual shift in fumarole locations.

(a)



(b)



FIGURE 1. 4 – COMPARATIVE AERIAL PHOTOGRAPHS FROM 2006 AND 1975

During the unrest event of 1975, the smooth Sherman Crater glacier became heavily crevassed. Thermal areas were enlarged and new fumaroles appeared. (a) For comparison, Sherman Crater in July 2006, looking west through the East Breach. Photo by John Scurlock. (b) Sherman Crater at the onset of the unrest event in March 1975, also looking west through the East Breach. Photo from Eichelberger et al., 1976.

(a)



(b)

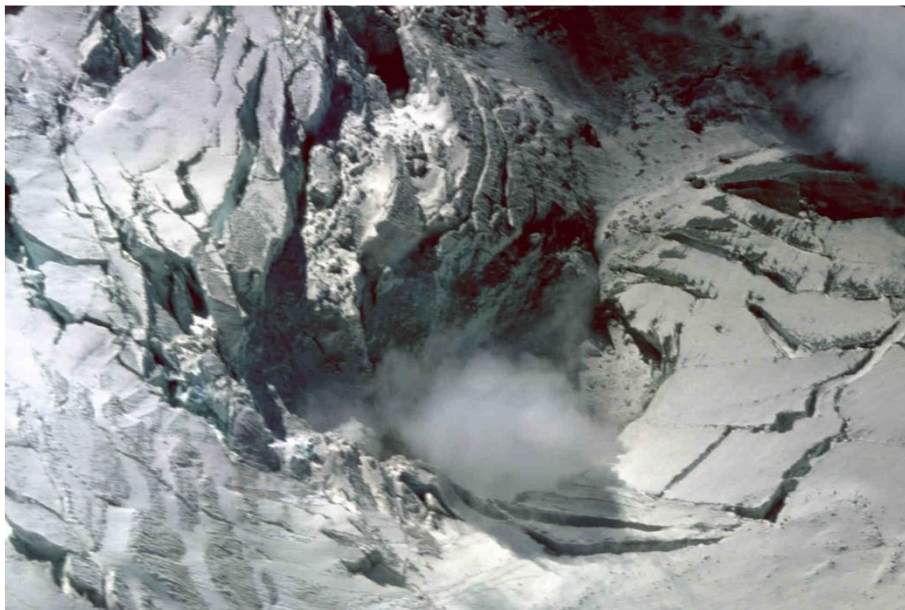


FIGURE 1. 5 - AERIAL PHOTOGRAPHS OF SHERMAN CRATER DURING THE 1975 UNREST EVENT

During the unrest event of 1975, a lake of boiling water (the Central Pit in Frank et al., 1977) formed near the East Breach. (a) April 10th, 1975. (b) June 30th, 1975. Photos by Don Easterbrook.

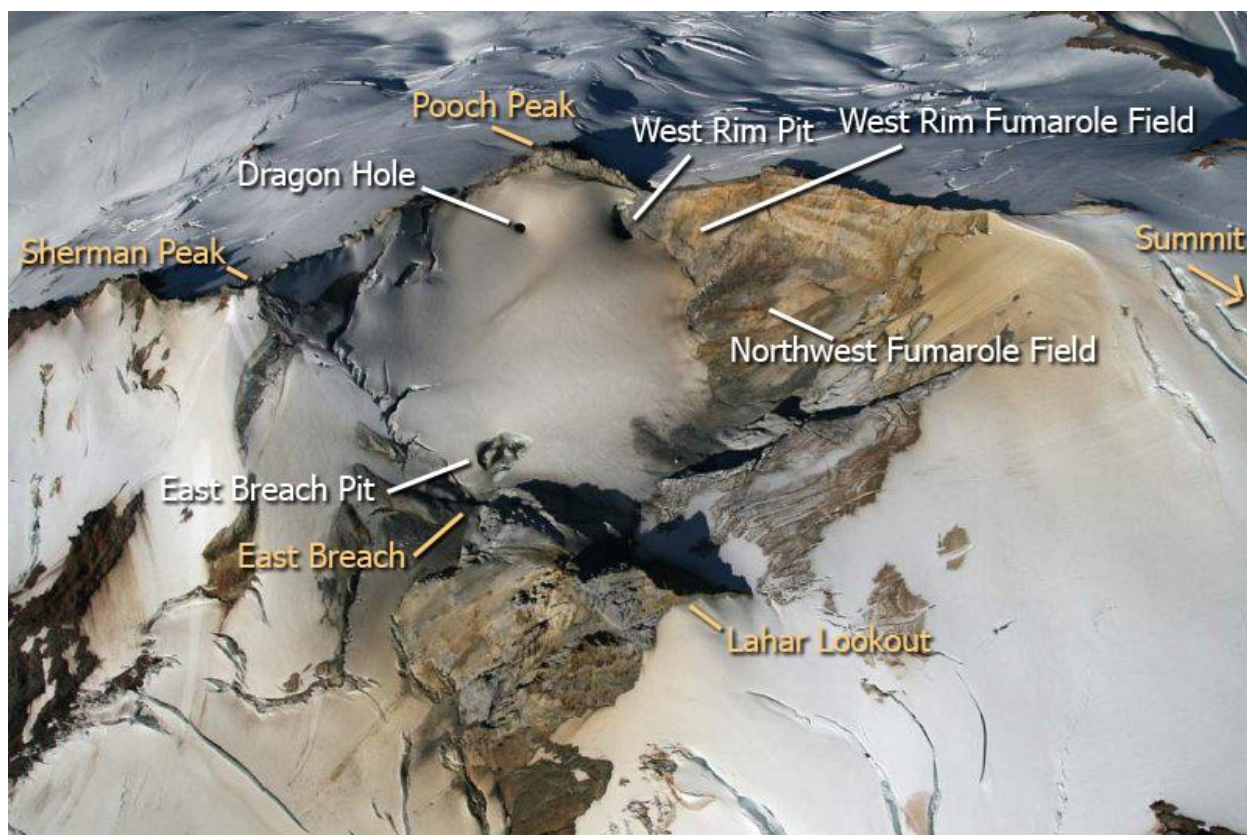


FIGURE 1. 6 – ANNOTATED AERIAL PHOTOGRAPH OF SHERMAN CRATER IN 2007

Oblique aerial view of Sherman Crater showing active thermal areas (in white) and crater rim features (in orange). Thermal areas include the Dragon Hole (or southwest pit), the West Rim Fumarole Field, including the West Rim Pit, the Northwest Fumarole Field and the East Breach Pit. Notable features of the crater rim include Sherman Peak to the southeast, the East Breach to the east, Pooch Peak to the west and Lahar Lookout to the north. The crater is about 195 meters in diameter. Photo by John Scurlock, July 2007.

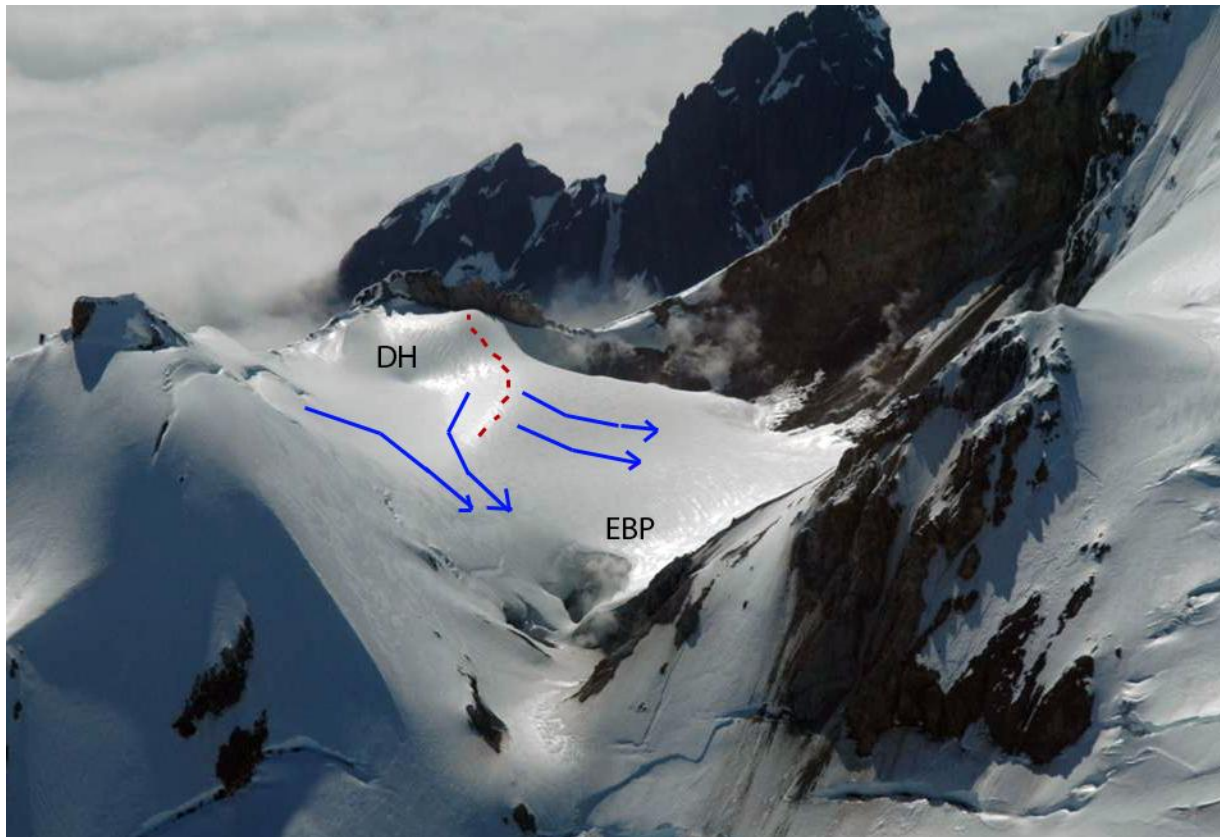


FIGURE 1. 7 – SKETCH OF EXPECTED ICE FLOW BASED ON OBSERVED GLACIER SURFACE TOPOGRAPHY

Aerial view of Sherman Crater showing expected ice flow direction based on observed glacier surface topography. I expect the ice that accumulates in the crater to flow generally towards the East Breach Pit (EBP) on the southwest side of the ridge below Pooch Peak (dashed red line) and towards the Northwestern Fumarole Field on the northeast side of that ridge. DH denotes the location of the Dragon Hole (not open in this photo). The crater is about 195 meters in diameter. Photo by Melissa Park, July 2010.

2 – DATA COLLECTION AND DATA PROCESSING

2.1 – DATA COLLECTION

Because the glacier in Sherman Crater has not been surveyed since 1975, my fieldwork aimed to determine the basic characteristics of both the modern crater and its glacier (e.g., crater diameter, total ice volume, ice thickness, annual mass balance and ice flow direction). All data for this project were gathered over the course of five expeditions in the summers of 2009 and 2010.

2.1.1 - GLACIER MASS BALANCE AND MOTION

My team and I installed and surveyed a network of ablation stakes (PVC pipes) in the crater glacier. The purpose of the ablation stakes was two-fold: by tracking changes in the positions of the stakes through the summer, we determined the ice flow pattern and velocity, and by measuring their exposed heights, we determined the volume loss from the glacier from surface melting and snowpack compaction (e.g., Hubbard and Glasser, 2005).

In late May 2009, we accessed the crater on snowmobiles and skis, equipped with a Leica total station, a steam drill and 50 meters of PVC pipe pre-cut in 1.5-meter long stake sections. These sections were assembled into longer stakes in the crater: three of the stakes were assembled to a length of 6 m, all others to a length of 3 m. We used a steam drill to install the three 6-meter ice stakes by planting them vertically in the glacier to a depth greater than the previous year's snow, identified by an increase in resistance to a metal probe. All other stakes were planted vertically by hand as follows: two lines of 5 stakes each followed the glacier's apparent flow lines, from slightly above and on either side of the Dragon Hole and running towards the East Breach (Figure 2.1). A few additional stakes completed two transects in straight lines running approximately north to south (Figure 2.1). During the May fieldwork, we also measured snow accumulation for the season using a metal probe at the location of each of the 6-meter stakes (Figure 2.1). The positions of all the stakes were then recorded using a Leica total station centered on a benchmark located on the western rim of the crater, once on the day of their initial installation, then twice more throughout the summer (May 31st, July 17th and August 8th; Figure 2.1). Two additional fixed benchmarks (BMR and SR, Figure 2.1) were surveyed to assess the accuracy of each set of measurements. These benchmarks were notches in apparently solid rock. BMR was located on the western rim, near the location of a geodetic benchmark that disappeared in early 2009. SR was located on a large rock slightly on the outside of the western rim. A new geodetic benchmark was setup in July 2009 near

the location of the SR benchmark. The precise coordinates of the geodetic benchmarks were used to estimate the location of the BMR and SR benchmarks.

We measured the length of the ice stakes exposed by surface melting and snowpack compaction twice during the summer (July 17th and August 5th). The shorter ice stakes had to be inserted further into the ice after each measurement to prevent them from melting out entirely before the next set of measurements. The three 6-meter ablation stakes were not repositioned after their initial installation.

2.1.2 - GROUND-PENETRATING RADAR (GPR)

In mid-July 2009 and 2010, my team and I imaged the glacier's subsurface using a GPR in both reflection profiling and common mid-point collection modes (CMP). The data gathered by the GPR are the two-way travel times of electromagnetic waves (EM waves) to material boundaries in the subsurface. A transmitter sends a pulse of energy into the subsurface, the ice in the case of the crater glacier. When the EM wave encounters an interface between materials with different dielectric properties, a portion of it is reflected back to the surface. A receiver at the surface records the arrival times of each reflected wave. These reflected pulses appear as stronger signals on GPR profiles (Baker et al., 2007). From the depth and character of these strong signals in reflection profiles, we can infer the ice thickness and the type of boundary at the base of the ice (e.g., ice/water, ice/hydrothermally altered rocks and ice/bedrock). From the slope of these strong signals in CMP profiles, we can calculate the velocity of EM waves through the ice.

The GPR system used consists of a Geophysical Survey Systems Inc. (GSSI) SIR-3000 controller unit and a GSSI unshielded multi-low-frequency (MLF) 3200 -antenna set to a center frequency of 80 MHz. This choice of frequency was based on preliminary tests on the Easton Glacier, on the south side of Mount Baker. For a velocity of 0.167 m/ns, an 80 MHz antenna provides a depth of penetration of at least 50 meters (Baker et al., 2007) and a vertical resolution of about 0.5 m for an ice layer and 0.02-0.03 m for a wet dust/debris layer ($1/4$ of the wave length λ , as determined from radar velocity and antenna frequency; Eder et al., 2008). This limit represents the thinnest layer that can be resolved.

In choosing the settings for the SIR-3000 controller unit, I followed the manufacturer's recommendations for use with the MLF-3200 antenna except for the number of samples per scan, the range and the gain points (GSSI, 2004). To ensure that the bottom of the crater was captured on the collected profiles, I set the range to 1500 ns. Assuming a typical velocity for EM waves in ice,

this corresponds to a two-way travel distance of ~250 meters or an ice-depth of ~125 meters. The GSSI SIR-3000 manual recommends placing the feature of interest in the vertical middle of the recorded profile (GSSI, 2004). Based on my depth estimate of 50 meters (estimated depth of the Dragon Hole), 1500 ns seemed the optimum setting for the range to capture the basal interface. Profiles were collected with 2048 and 4096 samples per scan in 2009 and 2010, respectively. With a recording range of 1500 ns for an 80MHz center frequency, sampling 2048 samples per scan yields 16 samples per EM wave. Although by the Nyquist theorem the minimum number of sample per wave to faithfully reproduce a signal is 2, a minimum of 6 samples/wave is preferred to ensure the details of each waveform are captured (Pettit E., 2010, personal communication). In 2009, I set the gain manually at five equidistant travel times based on ice readings collected in-situ to offset the effects of signal attenuation through glacial ice. The gain corrections applied were -20, 9, 2, 2 and +20 dB. In 2010, to reduce some of the signal “clipping” observed in the 2009 data, I set the gain manually to 3 points: -10 db at the surface, 0 dB half way through, +10 dB at the bottom of the scan.

My team collected data using the GPR in both reflection profiling mode and common mid-point (CMP) mode. For the reflection profiling survey, we placed the transmitting and receiving antennas on the snow at a fixed distance apart (1.5 meters, the length of the boom) and moved both simultaneously in incremental 1.2 meter steps (one antenna length) along each survey line (Baker et al., 2007; Figure 2.2). Because dipole systems transmit and receive their energy parallel to the antenna arms (Hubbard and Glasser, 2005), we moved the antennae in a parallel broadside configuration (antennae parallel to survey line – Figure 2.2) along approximate glacier flow lines to minimize signal reflections from the higher north and south sections of the crater rim. In 2009, we collected three west-east transects along the glacier’s flow lines to the south, center and north of the Dragon Hole towards the East Breach (Figure 2.3) and one south-north transects across the glacier. In 2010, we collected one east-west transect along a prominent ridge to the north of the Dragon Hole, two south-north transects, one across the Dragon Hole, one half-way between the Dragon Hole and the East Breach Pit and one diagonal transect above our inferred location for the bottom of the crater from 2009 data (Figure 2.3).

We also collected data in common mid-point (CMP) collection mode in 2009 to determine the exact distribution of radar signal velocity with depth given the particular snow and ice conditions for that day. These data were meant to increase the accuracy of depth estimates during the processing of transect profiles gathered in reflection profiling mode. To perform the CMP collection of data, we placed the transmitting and receiving antennas on the snow as close to each other as the equipment

allowed and moved them away from each other in incremental 0.36 m steps (twice the side length of the transmitter and receiver, 0.18 m each) until they were 7 meters apart (the length of the fiber optic cable connecting them). Because Eder et al. (2008) successfully determined velocity of propagation within different snow and ice layers down to 35 meters using a 100 MHz antenna and 0.10 m incremental steps for a maximum distance of 7 m, we deemed this cable length sufficient for our purpose.

2.1.3 - GLOBAL POSITIONING SYSTEM (GPS) AND ALTITUDE MEASUREMENTS

We collected 310 GPS waypoints in Sherman Crater with two Garmin GPSmap 60csx handheld GPS units in July 2010. Northing and easting locations were collected in WSG84 mode (World Geodetic System, version 1984, revised in 2004). Elevations were collected using the built-in altimeter. Of these 310 GPS waypoints, 155 waypoints were collected during the GPR survey and mark every fifth GPR scan location along linear transects (Figure 2.4). The remainder of the data points was collected at various locations on the glacier, including the periphery of the ice as it appeared in mid-July 2010 (Figure 2.4). In 2009, the elevation of every tenth GPR scan was recorded using a handheld altimeter.

2.2 - DATA PROCESSING

I processed all data at Western Washington University with software packages available in the Geology Department. In particular, I analyzed ablation stake data using Microsoft Excel and ESRI ArcGIS 10.0. I created ice thickness maps, topographic maps and surface representations of the base and surface of the glacier with Golden Software Surfer 8.0. I processed all GPR data with GSSI Radan 6.0 and Microsoft Excel.

2.2.1 – GLACIER MASS BALANCE AND MOTION

Coordinates of ablation stakes recorded with the Leica total station were translated to UTM locations based on their distance from a set of benchmarks on the crater rim for which GPS coordinates are available (Hodge, 2009, personal communication). These coordinates, representing the location of ice stakes in May and August 2009, were imported into ArcGIS and superimposed on a 2009 orthographic aerial photograph of the crater (NAIP, digital orthographic imagery, 2009; Figure 2.1).

Easting, northing and elevation data for stake locations were analyzed in Microsoft Excel. A comparison of coordinates for what should have been fixed benchmarks (BMR and SR) between May and August revealed a difference in elevation of 0.81 m for both benchmarks. The elevation

component of the August coordinates was therefore reduced by 0.81 m. Changes in easting and northing were not consistent: BMR “moved” 0.02 m to the north and 0.46 m to the west while SR “moved” 0.05 m to the north, but only 0.04 to the west. I could not resolve this discrepancy, which is likely the result of actual movement of the benchmarks, and therefore applied neither east-west nor north-south correction to the data.

2.2.2 – GPS POINTS PROCESSING

The elevations of GPS waypoints were recorded with the Garmin 60csx’s built-in altimeter. Because the barometric pressure gradually changed throughout the day, these elevations had to be normalized. For those points along GPR transects, I calculated the difference between measured elevations at locations where GPR transects intersect and deduced the rate of change in elevation per minute between recordings. I applied this time-dependent change to waypoints along the intersecting transect that displayed the lowest elevations. Because the date and time were set incorrectly on the second GPS unit, I was unable to use the same strategy to normalize waypoints collected at random locations on the glacier. I opted instead for a uniform correction to all points collected with this second unit by matching the elevation of those closest to an intersection of GPR transects to the corrected data from the first GPS unit.

2.2.3 – GPR CMP DATA ANALYSIS

Common mid-Point (CMP) radar surveys are used to derive an estimate of the EM wave velocity versus depth by increasing the spacing between transceiver and receiver antennas over a fixed center location. Reflectors in CMP profiles are down-trending half-hyperbolas representing the increasing travel times to prominent interfaces directly below the center location as the transceiver and receiver are separated stepwise (Figure 2.5 - a). When plotted on a $(t^2 - x^2)$ graph (Figure 2.5 - b), these two-way travel times yield a straight line for each prominent reflector (Burger et al., 2006). The EM wave velocity through the subsurface can be calculated using the Dix equation:

$$V_{rmsi} = \sqrt{\frac{\sum_i^n V_i^2 \Delta t_i}{\sum_i^n t_i}} \text{ (Burger et al., 2006), where } V_{rmsi} \text{ is the root-mean-square velocity of EM waves}$$

from the surface to layer i. Parameters for the Dix equation are: V_i , the velocity determined by the inverse square root of the slope of the straight line representing the reflector at the base of layer i (Figure 2.5 - b) and t_i , the vertical to near-vertical one-way travel time from the surface to the reflector at the base of layer i (determined on Figure 2.5 - a, center). Burger et al. (2006) recommend the use of the Dix equation for a multi-layer subsurface. This set of equations is therefore appropriate for the ice in the crater glacier.

I used Radan 6.0's Depth Pick tool in EZ-track mode to locate the onset of 4 reflectors for which a distinct offset was visible (continuous solid white upper-layer of an hyperbola) in CMP profiles and saved these arrival times for each scan to a .lay file. From this .lay file, I imported the offset distances and associated two-way travel times to a Microsoft Excel spreadsheet for further processing, including the plotting of $(t^2 - x^2)$ graphs (Figure 2.5 - b) and the derivation of velocities using the Dix equation.

2.2.4 – GPR REFLECTION PROFILING DATA ANALYSIS

2.2.4.1 – Post processing

Post-processing of each set of reflection profiling data consisted of a +2 dB uniform gain and surface elevation correction. I applied a +2 dB uniform gain during post-processing to increase the contrast of prominent reflectors in profiles for ease of interpretation. Although noise, such as ringing multiples, is visible in the data, I found post-processing filtering, in addition to the filtering applied during collection, to be unnecessary; these ringing multiples are obvious in their symmetry and cannot be mistaken for real reflectors. I also opted to not migrate the data. Migration is commonly used in GPR signal processing to remove artificial parabolic reflectors even though the process also removes some of the “real” signal (Binder et al., 2009). Because only a few parabolic reflectors appear in GPR profiles collected in Sherman Crater, migration would have degraded rather than enhanced the quality of my data and therefore would have been detrimental to analysis. I applied to each scan a surface elevation correction to match the observed surface topography (Hubbard and Glasser, 2005) and stretched profiles horizontally by a factor of 5 to equalize the horizontal distance to depth ratio (Figure 2.6).

2.2.4.2 – GPR scans geolocation for 2009

Because GPS locations for GPR transects are only available for 2010, I estimated the approximate easting and northing for the 2009 data by extrapolating between those locations where GPR scans can be matched to ablation stakes from field notes. I verified my result by calculating the distance between 10 scans, which must be ~12 m (10 scans * 1.2 m between scans). I found this method adequate for qualitative assessment of the subsurface but where discrepancies occur between the 2009 and 2010 data, which are matched to precise GPS waypoints coordinates, I favored the 2010 data.

2.2.4.3 – GPR reflector analysis

The GPR profiles recorded in the crater reveal different types of reflectors below the ice surface. The nature of these reflectors is identified by analyzing their amplitude, continuity and phase sign.

The amplitude of a reflector relates to the contrast in dielectric constant across an interface between two materials. This interface causes a scaled version of the radar pulse to be reflected back to the surface according to the reflection coefficient K:

$$\frac{\sqrt{\epsilon_2} - \sqrt{\epsilon_1}}{\sqrt{\epsilon_2} + \sqrt{\epsilon_1}}$$

(where ϵ_1 and ϵ_2 are the dielectric constants of the material above and below the interface, respectively; Baker et al., 2007). The higher the reflection coefficient, the more contrast in the GPR profile. Typical dielectric constants for materials we expect to find in Sherman Crater are: ice=3-4, wet sand/rubble (assumed to be similar to hydrothermally altered regolith) =10-30, basaltic bedrock=6, water=81 and air=1 (Baker et al., 2007). A high reflection coefficient, such as that of an ice/water interface ($K=0.64-0.68$) corresponds to a high contrast reflector (e.g., white-black-white) in the GPR profiles. Lower reflection coefficients, such as that of an ice/bedrock interface ($K=0.10-0.17$), appear as shades of grey (e.g., light grey-dark grey-light grey) and result in low contrast reflectors in GPR profiles. Because the exponential gain applied during data collection compensates for signal attenuation at depth, we assume that the apparent contrast of reflectors in GPR profiles accurately represents the reflection coefficient of material boundaries at all depths, with the exception of the top ~50 ns, which is obscured by the time-constant direct coupling pulse (high-contrast surface reflection; GSSI, 2004).

The amplitude of the reflection coefficient is generally insufficient to uniquely determine a specific type of interface; continuity and polarity must also be considered. Continuity hints at the homogeneity of the contact: an ice/water or ice/bedrock interface likely produces a relatively continuous reflector, whereas because hydrothermally altered regolith can be altered to different degrees, the interface between ice and hydrothermally altered regolith is heterogeneous and therefore produces a discontinuous reflector. Reflectors representing ice/air interfaces should display a reversal of phase (black-white-black instead of white-black-white). The negative reflection coefficients associated with ice/air interfaces ($K=-.033$ to -0.27) result from the relative decrease in dielectric constant across the material boundary.

2.2.4.4 – GPR depth picks

In profiles collected in 2009, basal reflectors stand out prominently from the background and are easily identified, except in a few locations. The area near the center of the crater has several possible basal reflectors. By comparing the relative position of similar reflectors in different profiles, I separated reflectors representing the base of the glacier from reflectors representing side

echoes from the crater rim or from ringing in the antennae. In profiles collected in 2010, basal reflectors are partially obscured by intermittent interferences in the data. The base of the ice in 2010 profiles was inferred by extrapolating between scans unaffected by interferences.

The base of the ice along each GPR transect was determined in Radan 6.0 using the Depth Pick tool. For each scan that corresponds to a GPS waypoint (every 5th scan along transects collected in 2010) or an estimated geolocation (every 10th scan along transects collected in 2009), I clicked on the reflector I interpreted as the basal reflector (Figure 2.7). This set of points was saved as a .lay file and imported into Microsoft Excel. Of interest to me in the .lay file is the two-way travel time to the basal reflector. I subtracted from the total two-way travel time to the base the 0-position offset at the top of each profile (usually between 110 and 150 ns) during collection and converted time to distance using the average velocity for the ice in the crater glacier derived from CMP data, 0.151 m/ns (Section 3.4).

2.2.5 – GLACIER CHARACTERISTICS – MAPS AND CALCULATIONS

2.2.5.1 – Ice thickness and ice flow maps

I used Surfer 8.0 to produce ice-thickness and ice flow maps and to estimate the total ice volume in the crater. The ice-thickness map was created by estimating the glacier's thickness in all locations by extrapolating between the set of depths calculated along GPR profile lines and the glacier's periphery where the thickness is 0 (Figure 2. 8). Surfer's vector tool was used to create a map of expected ice flow direction and relative velocity in the crater based on the glacier's surface topography.

2.2.5.2 – Ice density used for water-equivalency conversions

Because ice volume and ice depths calculations are typically primarily used to estimate meltwater volume, these values are most useful when presented as water-equivalent (W.E.). The W.E. volume is the volume ice would occupy if it were melted to water (W.E. volume=measured volume*density of ice/density of water). When calculating W.E. ice depth (or thickness), the W.E. value actually represents a volume per unit area so its unit is the meter. In this study, volumes were calculated both from the measured ice depths and the calculated W.E. ice depths.

Various values for the density of a typical snowpack in the Cascades can be found in the literature: According to Kay (2006), typical late-Winter Cascade snow is homogeneous, isothermal and has a density of ~450 kg/m³, with a densification rate of ~ 50 kg/m³ per month during the snow season. Pelto (2010) measured a density of ~600 kg/m³ on the Easton glacier, at an elevation of 2450

meters, in August. Frank et al. (1977) used a density of $\sim 700 \text{ kg/m}^3$ to estimate the W.E. volume and depths in Sherman Crater. Because Sherman Crater (elevation $\sim 2900 \text{ m}$) is at least 450 m higher than the location of Pelto's (2010) ice density measurements and because higher elevation corresponds to higher accumulation and higher densification rates (Kay, 2006), I expect the average density for the ice in Sherman Crater to be higher than that measured by Pelto, but to an unknown extent. In order to facilitate comparisons between Frank et al.'s (1977) and my own glacier data, I have therefore used a density of $\sim 700 \text{ kg/m}^3$ for all depth measurements and volume calculations. I trust that this value is reasonably accurate for the ice in Sherman Crater.

2.2.5.3 – Ice volume

Ice volume was calculated by applying Surfer 8.0's differential analysis tool to the ice-thickness map. I verified this value by calculating the volume of a paraboloid with the maximum W.E. ice depth found in my radar depth picks and an approximate radius calculated from the total surface area (Appendix A). The paraboloid method was used by Frank et al. (1977) to estimate the volume of ice in Sherman Crater before the unrest event of 1975.

2.3 – HEAT FLUX CALCULATIONS METHODS

To calculate the modern heat flux in the crater, I applied Welch et al.'s (2007) calorimetric model developed for the caldera of Mount Veniaminof, in Alaska and Frank et al.'s (1977) thermal ground model to data measured and calculated for Sherman Crater.

2.3.1 – GLACIER CRATER CALORIMETRY (THE WELCH MODEL)

The Welch et al. (2007) model input parameters are: surface ablation, annual accumulation and latent heat of fusion.

Because Sherman Crater is located entirely above the regional glacier equilibrium line altitude, the annual mass balance (annual accumulation – (surface ablation-thickness reduction due to compaction)) yields a positive number. This number is the volume of ice that must be melted yearly per square meter at the base of the glacier to account for its observed steady-state in photographs from 2003 to 2008. The heat flux is thus simply the melt rate times the latent heat of fusion for ice divided by the glacier area (Welch et al., 2007).

$$\underline{H = L * \text{Melt rate}/A}$$

H = Heat Flux in W/m²

L = Latent heat of fusion for ice, 333550 J/kg (Welch et al., 2007)

A = Area of thermally affected grounds

Melt rate = Dm/t in kg/s

t = seconds in a year (31,557,600 s in a Julian year, IAU system of units)

$$\underline{Dm = D * \rho_{ice}}$$

Dm = Mass of melted basal ice in a year (in kg)

D = Volume of basal melted ice in a year (in m³)

D = Actual (not W.E) annual mass balance*Glacier area

ρ_{ice} = Average density of glacier \sim 700 kg/m³ (Frank et al., 1977)

2.3.2 – THERMAL AREAS MODEL (THE FRANK MODEL)

The Frank et al. (1977) model input parameters are the area of thermal grounds of three types: A: snow free year-round, B: snow-free in summer, C: covered year-round, and for each area type a measurement or estimate of the geothermal flux density for that area type.

With the help of Dave Tucker of the Mount Baker Volcano Research Center and John Scurlock, aerial photographer, I estimated the location and size of areas of type A based on the analysis of a series of aerial photographs from different angles and ranging in date from November 2009 to January 2011 (Figure 2.9; Scurlock, 2011). I measured areas of type B in ArcGIS by selecting snow free thermal grounds on a mid-summer orthographic photograph of the crater from 2009 (NAIP, digital orthographic imagery, 2009) and subtracting those sections identified as type A (Figure 2.9). I also measured areas of type C in ArcGIS by selecting snow covered areas in the same mid-summer orthographic photograph.

For areas of type A, since no updated measurement for point source heat flux is available, I applied the standard value of $H=419 \text{ W/m}^2$. White (1969) calculated $H= 419 \text{ W/m}^2$ as the heat flux necessary for melting falling snow at a rate of 0.1 m/day (W.E). This value, which represents a minimum heat flux, was deemed appropriate for Mount Baker by Frank et al. (1977).

For areas of type B, I assumed that the amount of snow and ice melted is equivalent to that accumulated during the prior snow season (6.8 ± 1.0 m), as this is the amount that would have accumulated over bare ground during the winter (Section 3.1.1). Heating continues after bare ground is exposed, however, so the calculated heat flux for areas of type B is also a minimum.

For areas of type C, I could not use the volume of newly created crevasses to calculate thinning of the glacier based on its extension: crevassing in Sherman Crater is currently confined to the ice adjacent to the southern rim and to the steep slopes below Sherman Peak, and is only apparent in late summer. Instead I used a volume loss per square meter of 4.0 ± 1.5 m (the annual mass balance; section 4.2).

For areas B and C, H was calculated using Equation 1 (Section 1.3.2). The total heat flux for the crater is the weighted (by area) average of heat fluxes calculated for each area type.

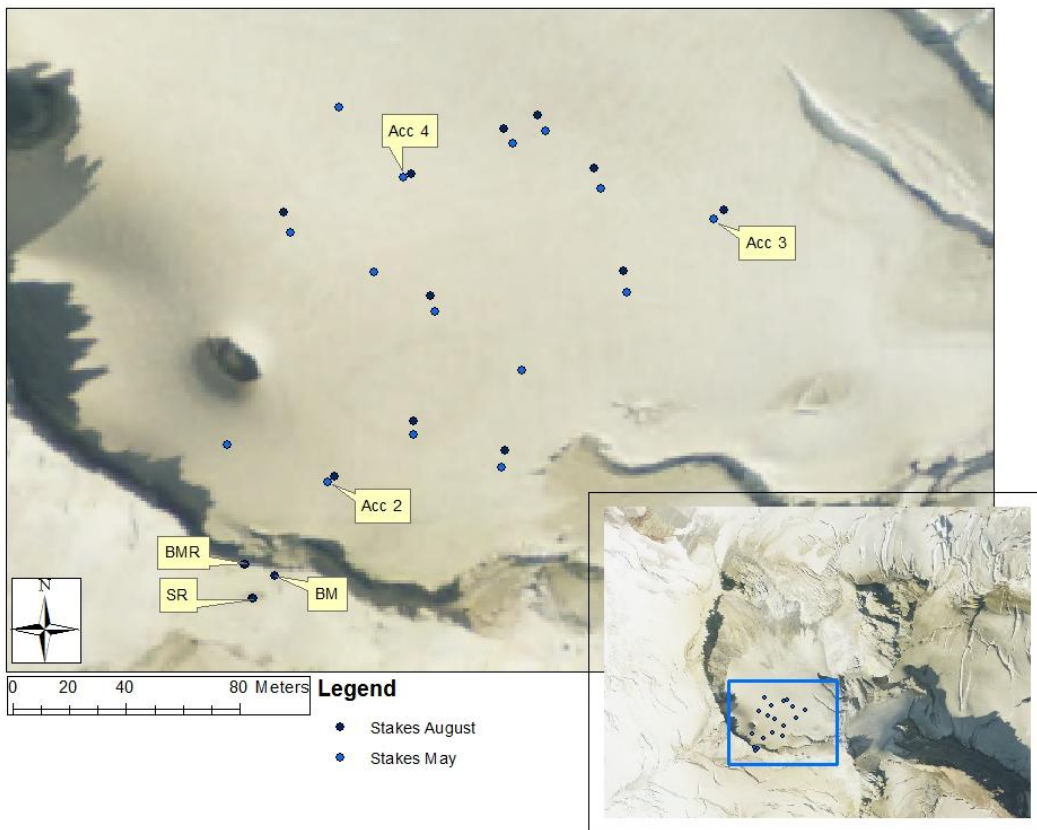


FIGURE 2. 1- MAP OF LOCATIONS OF ABLATION STAKES IN MAY AND AUGUST 2009

Locations of ablation stakes in Sherman Crater in May and August 2009. Acc 2, Acc 3 and Acc 4 denote stake locations where snow accumulation for the winter of 2008-2009 was measured. BM denotes the location of the benchmark above which the Leica total station was positioned for both sets of measurements. BMR and SR are control benchmarks on the crater rim used to assess the accuracy of measurements of the moving stakes. The insert gives an overview of these locations relative to Sherman Crater.

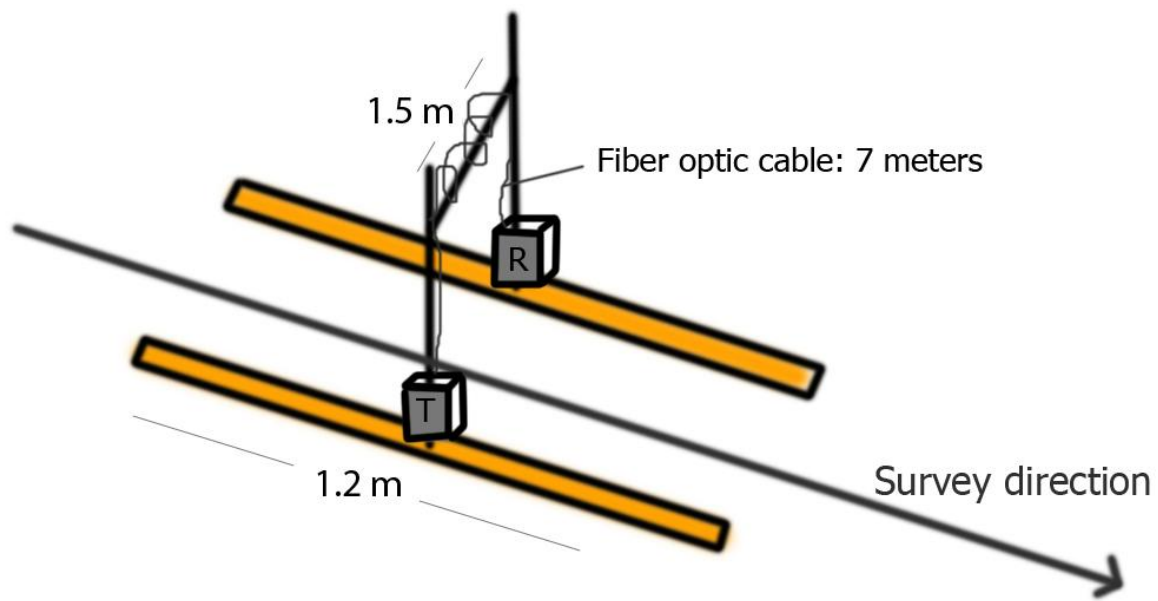


FIGURE 2. 2- SKETCH OF GROUND PENETRATING RADAR (GPR) SETUP

The GSSI MLF 3200 antenna (orange tubes) is in parallel broadside orientation (parallel to survey direction). Antenna separation is 1.5 meters (the length of the boom). Incremental steps are 1.2 meters (the length of the antenna). The side length of the transmitter (T) and receiver (R) is 0.18 meters. This GPR system also comprises a SIR-3000 control unit not shown on this sketch.

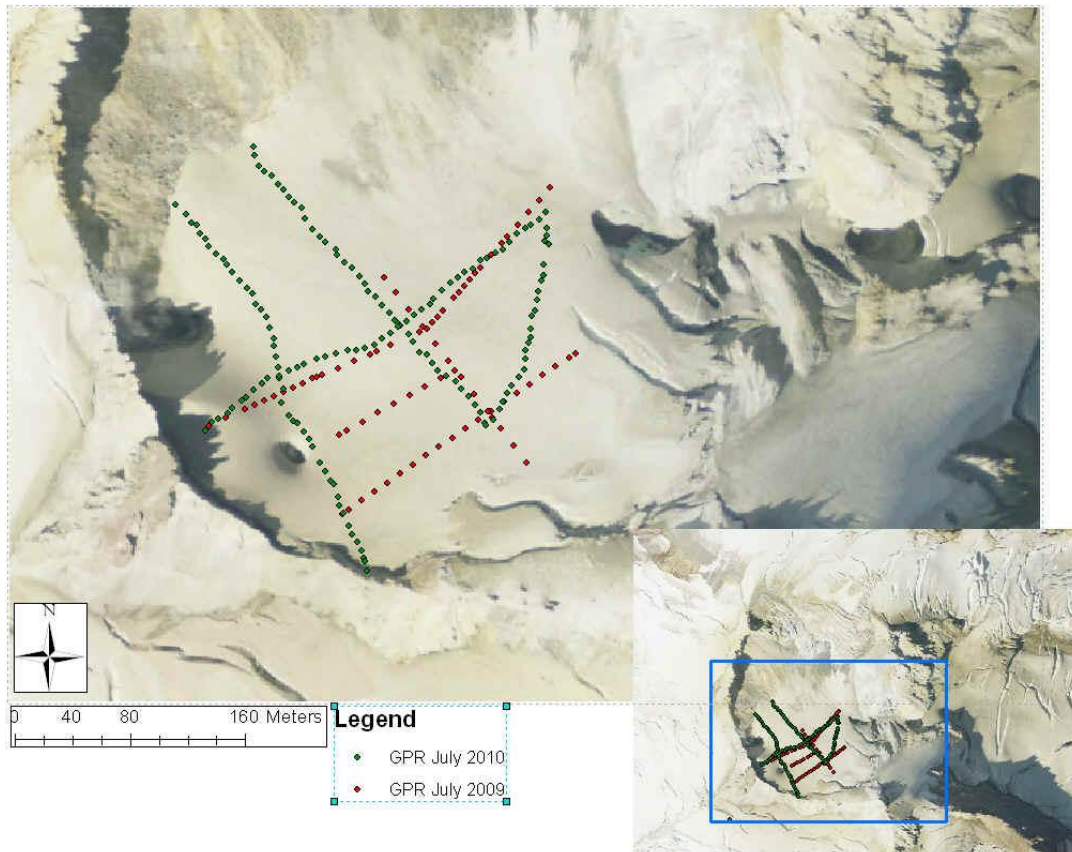


FIGURE 2. 3 - MAP OF GPR SURVEY LINES IN 2009 AND 2010

Ground Penetrating Radar (GPR) survey lines in Sherman Crater. In green are the GPS waypoints collected at every fifth GPR scan, collected in July 2010. In red are the approximate locations of every tenth GPR scan, estimated from 2009 field notes by extrapolating between scans at known stake locations. The insert gives an overview of these locations relative to Sherman Crater.

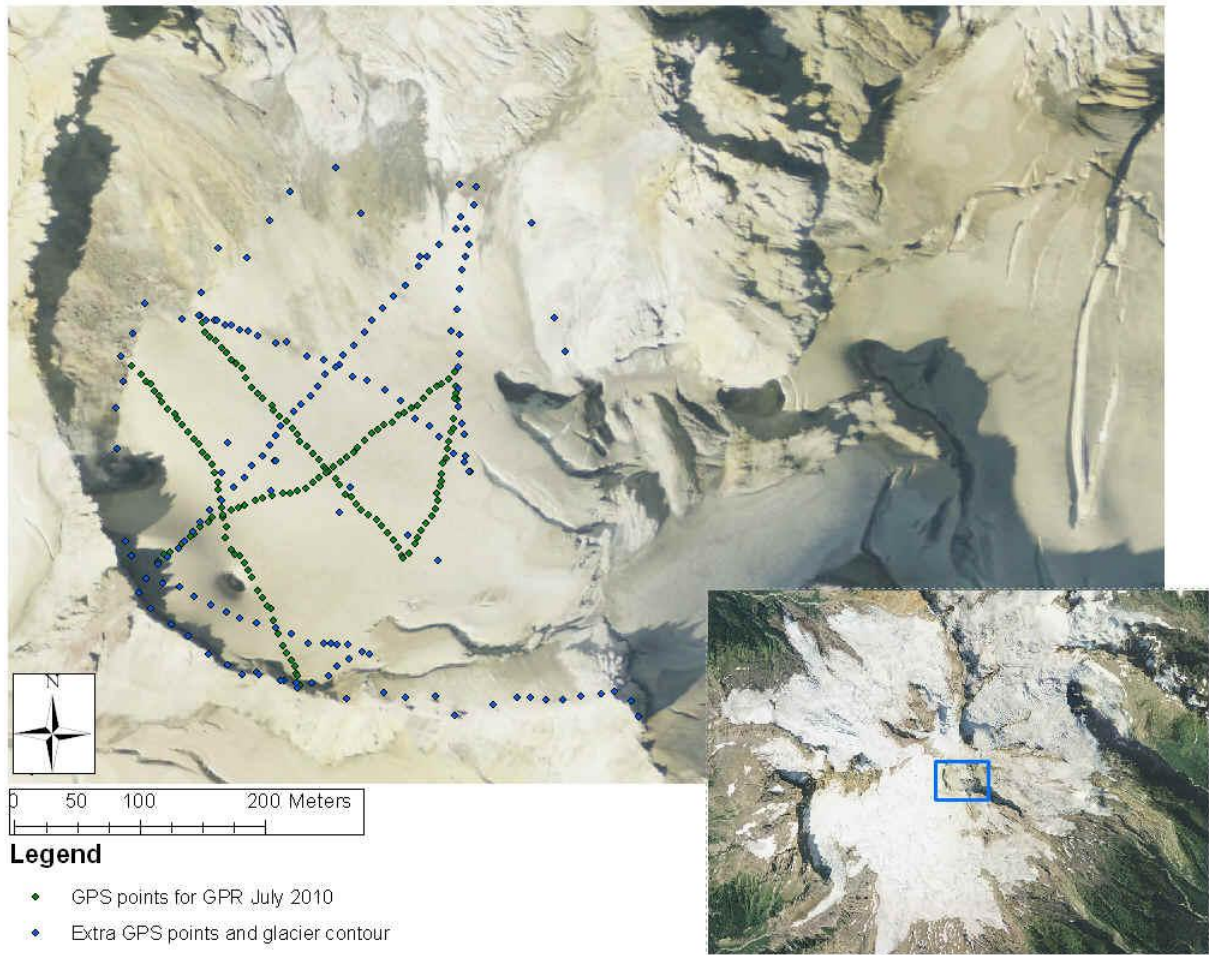


FIGURE 2. 4 – MAP OF GLOBAL POSITIONING SYSTEM (GPS) WAYPOINTS COLLECTED IN 2010

Global Positioning System (GPS) waypoints collected in Sherman Crater. In green are the GPS waypoints collected at every fifth GPR scan, collected in July 2010. In blue are GPS waypoints collected at the periphery of the glacier (where safe) and other mostly random locations on the glacier surface. The insert gives an overview of these locations relative to Mount Baker.

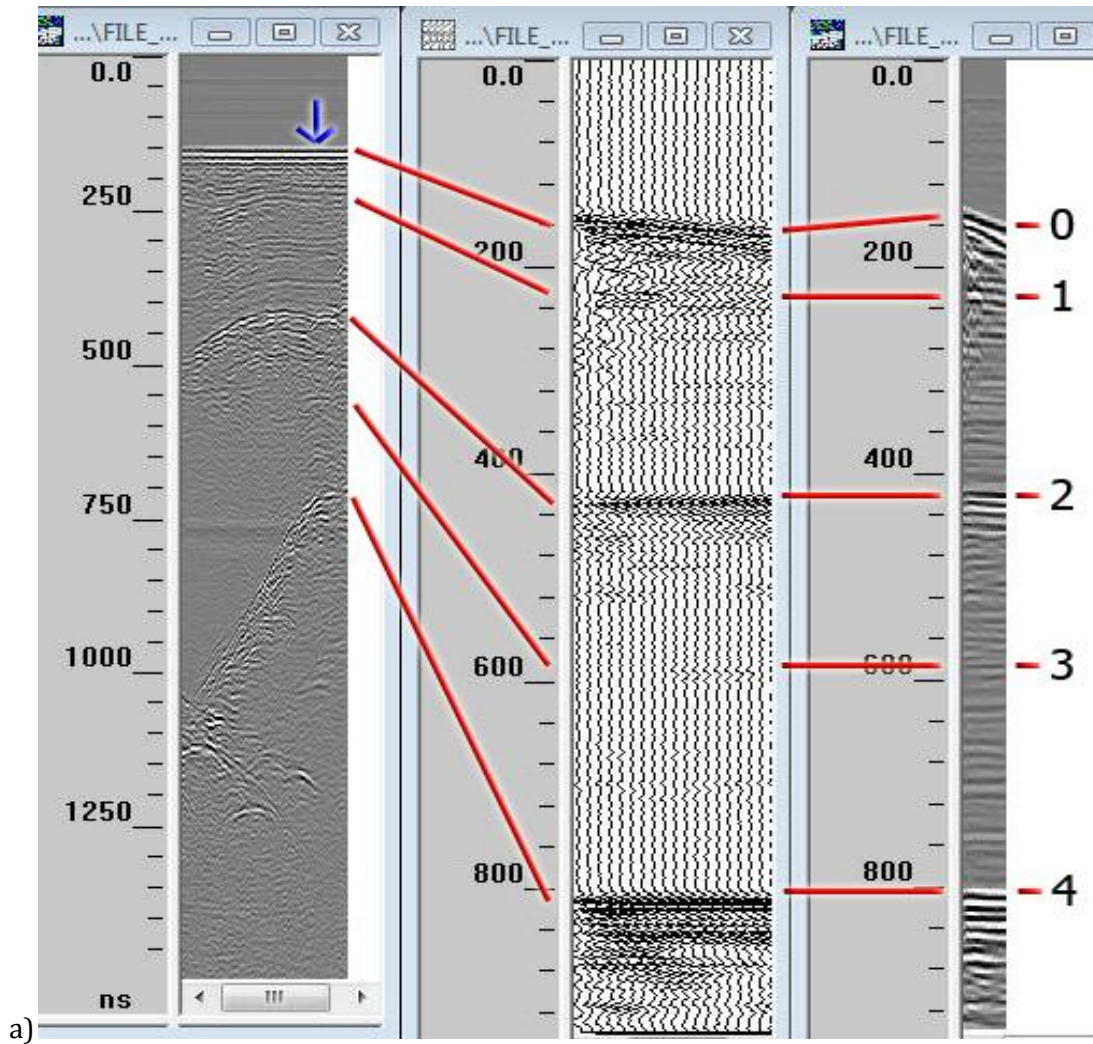
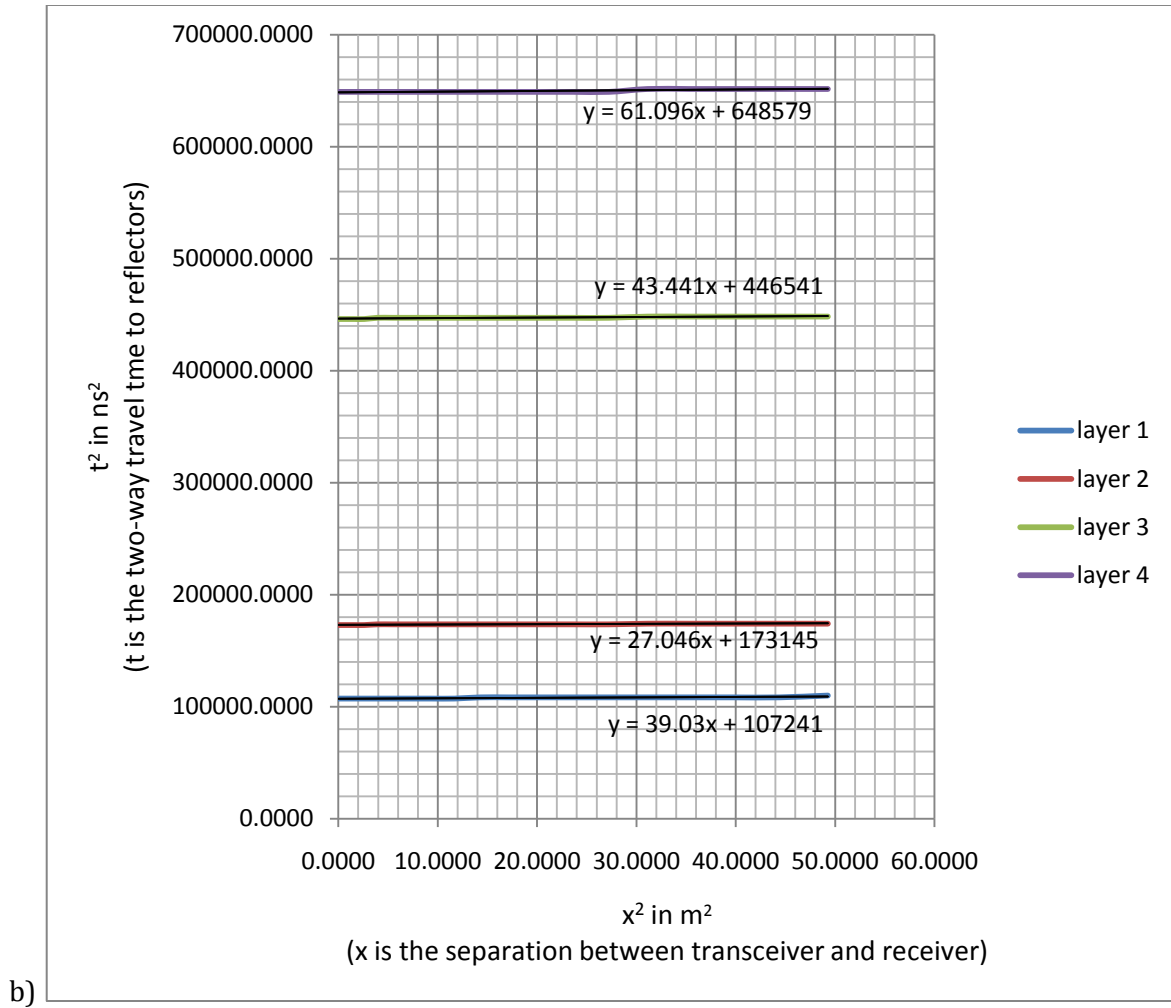


FIGURE 2. 5- GPR CMP DATA RECORD

- a) GPR record for data collected in CMP mode in Sherman Crater in Wiggles mode (center) and LineScan mode (right). Red lines point to reflectors with (x,t) coordinates used in the (x2 – t2) graph: (0) is the air-wave, representing the surface, (1) is a faint reflector close to the surface, (2) is a strong englacial reflector, (3) is a faint reflector below the strong englacial reflector, and (4) is the basal reflector. The blue arrow in the left-hand panel marks the approximate location of the CMP survey in GPR reflection line 003, collected in 2009 from approximately the center of the glacier to the eastern edge of the Dragon Hole (short red center line on figure 2.3).



- b) ($x^2 - t^2$) graph for the prominent reflectors in the GPR reflection line 003: Layer 1 and 3 are faint englacial reflectors, line 2 is a strong englacial reflector, line 4 is a basal reflector. The slopes of the lines in the graph represent $(1/v_i)$ for each layer i and are used to estimate the velocity of EM waves through ice using the Dix equation. The intercept of each line with the t^2 axis is t_0 in the individual layer equation (Burger et al., 2006).

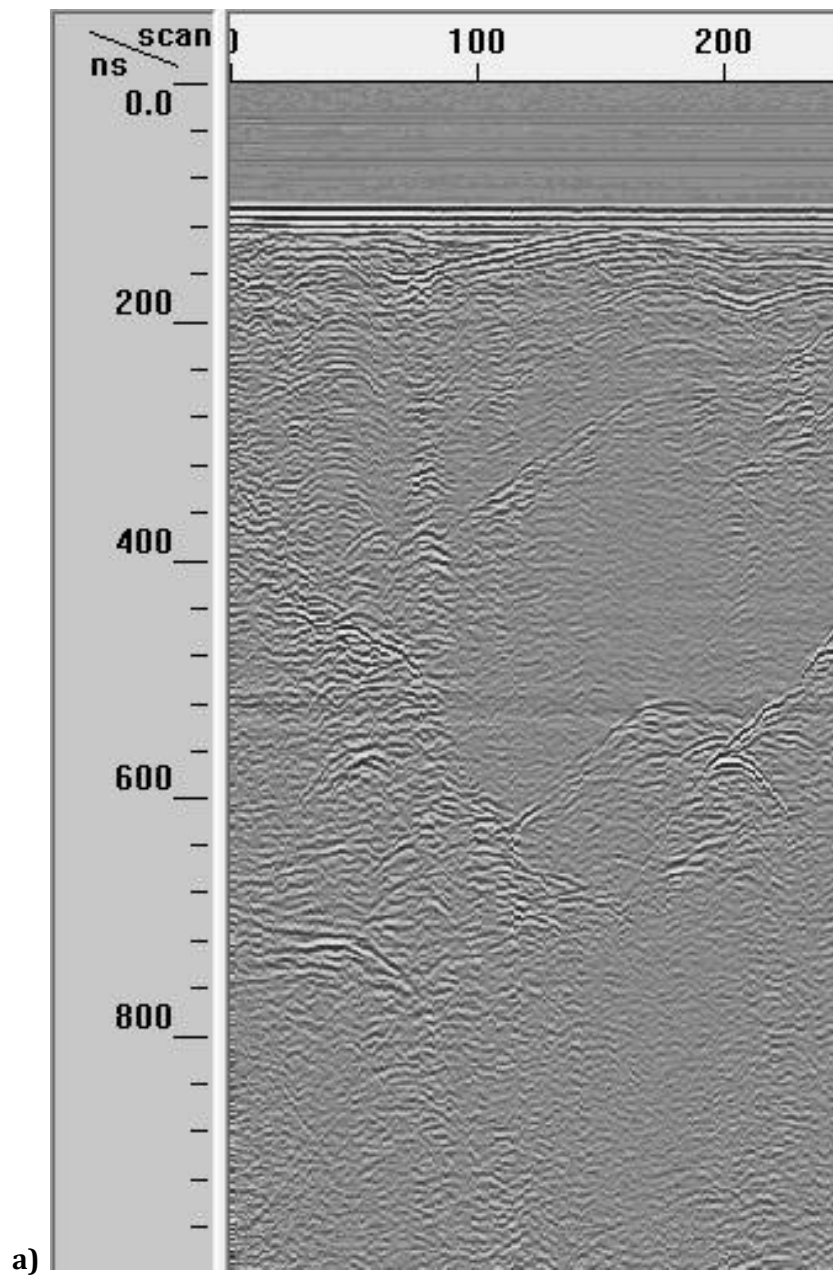
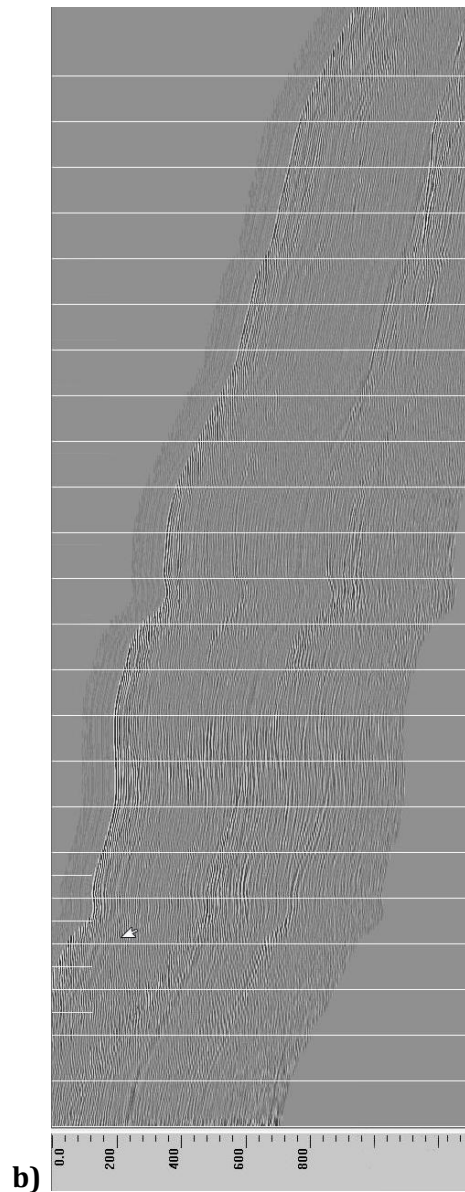


FIGURE 2. 6 – EXAMPLE OF GPR PROFILE BEFORE AND AFTER PROCESSING

a) GPR profile processing example. A) Unprocessed GPR profile (line 006 from Pooch Peak to East Breach collected in July 2009; Figure 2.3).



b) GPR profile processing example. An elevation is assigned to each scan for which it is available (every 10th scan in the case of this particular profile). Using GSSI Radan 6.0, surface correction is applied to the profile. A stretch factor of X5 is then applied to the corrected profile to equalize horizontal distance and depth. In some cases, top or bottom clipping of important data can occur. Clipped, corrected profiles are stitched together in Photoshop CS4. This image is a composite of six clipped, stretched, corrected profiles.

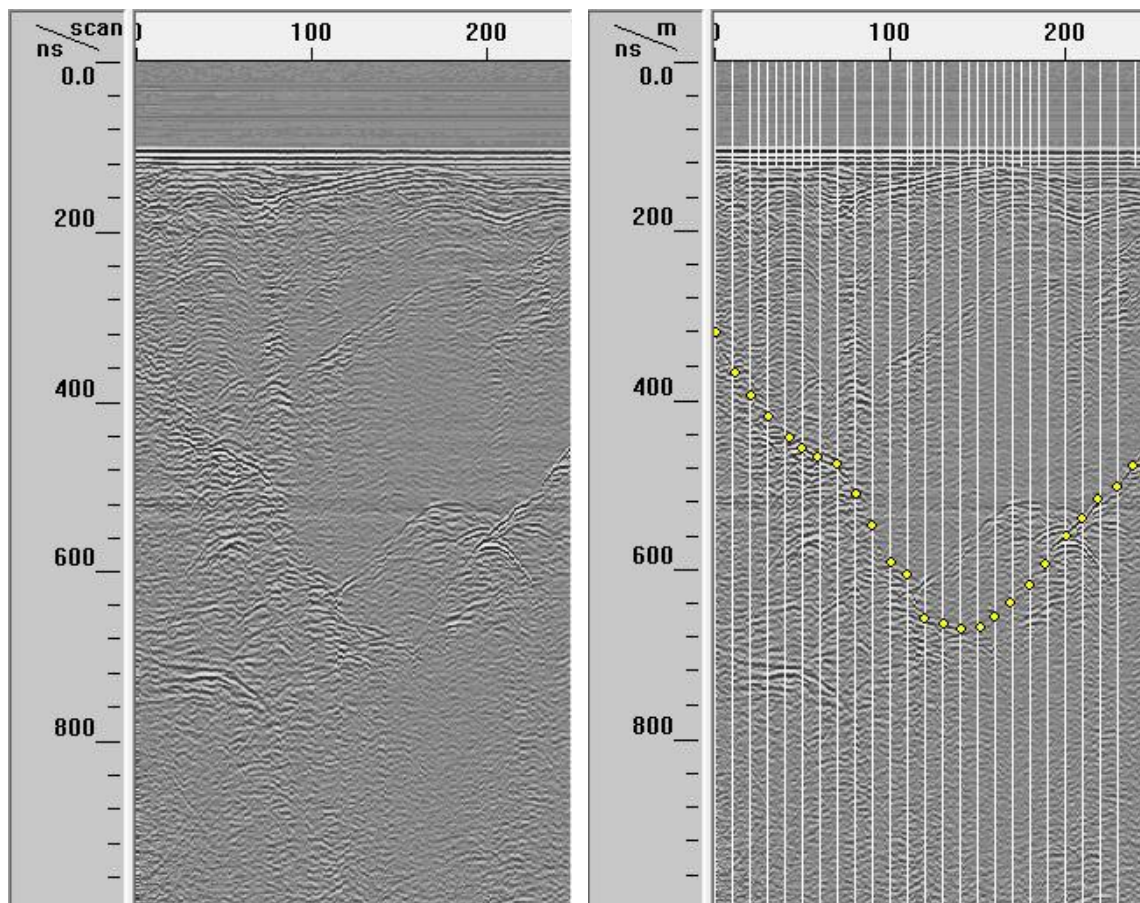


FIGURE 2.7 – EXAMPLE OF DEPTH PICK PROCESSING

For each scan for which an easting and northing is known (white lines in “after” profile), the reflector interpreted to be the base of the glacier is selected. These data are then exported to a .lay file and into Microsoft Excel for further processing.

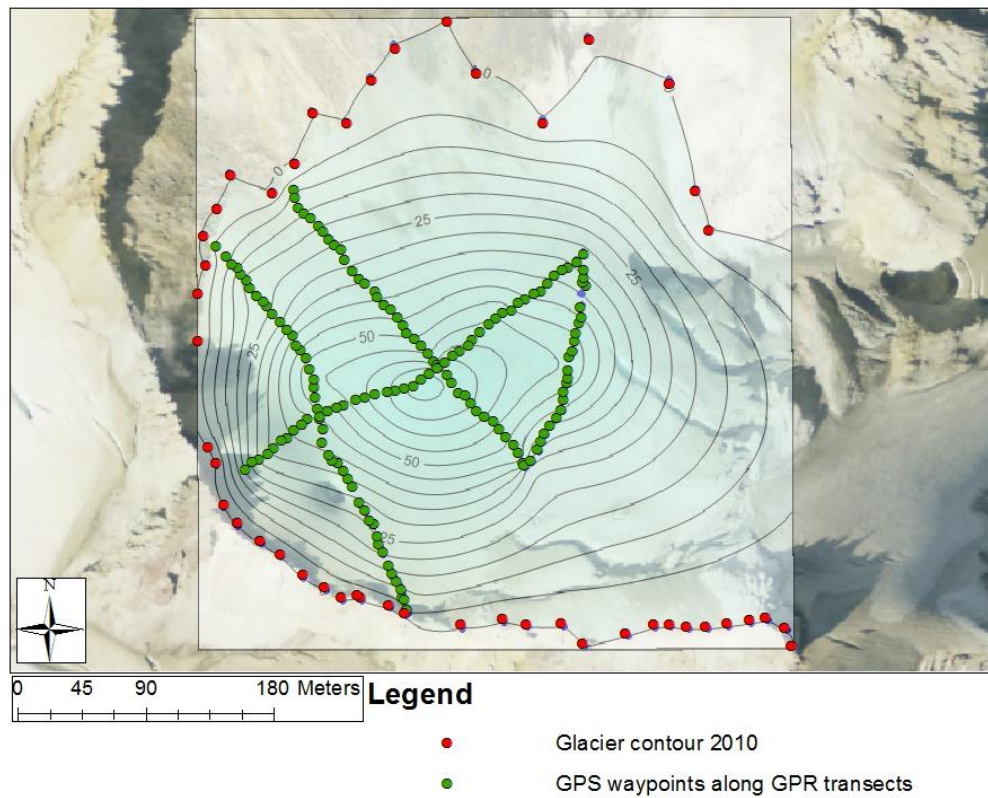


FIGURE 2. 8 – ICE THICKNESS MAP

Ice thickness map for 2010 created in Surfer 8.0 by extrapolating between known ice thicknesses (measured, not water-equivalent) in locations where GPR scans were collected (in green) and the glacier's periphery with ice depth = 0 m (in red).

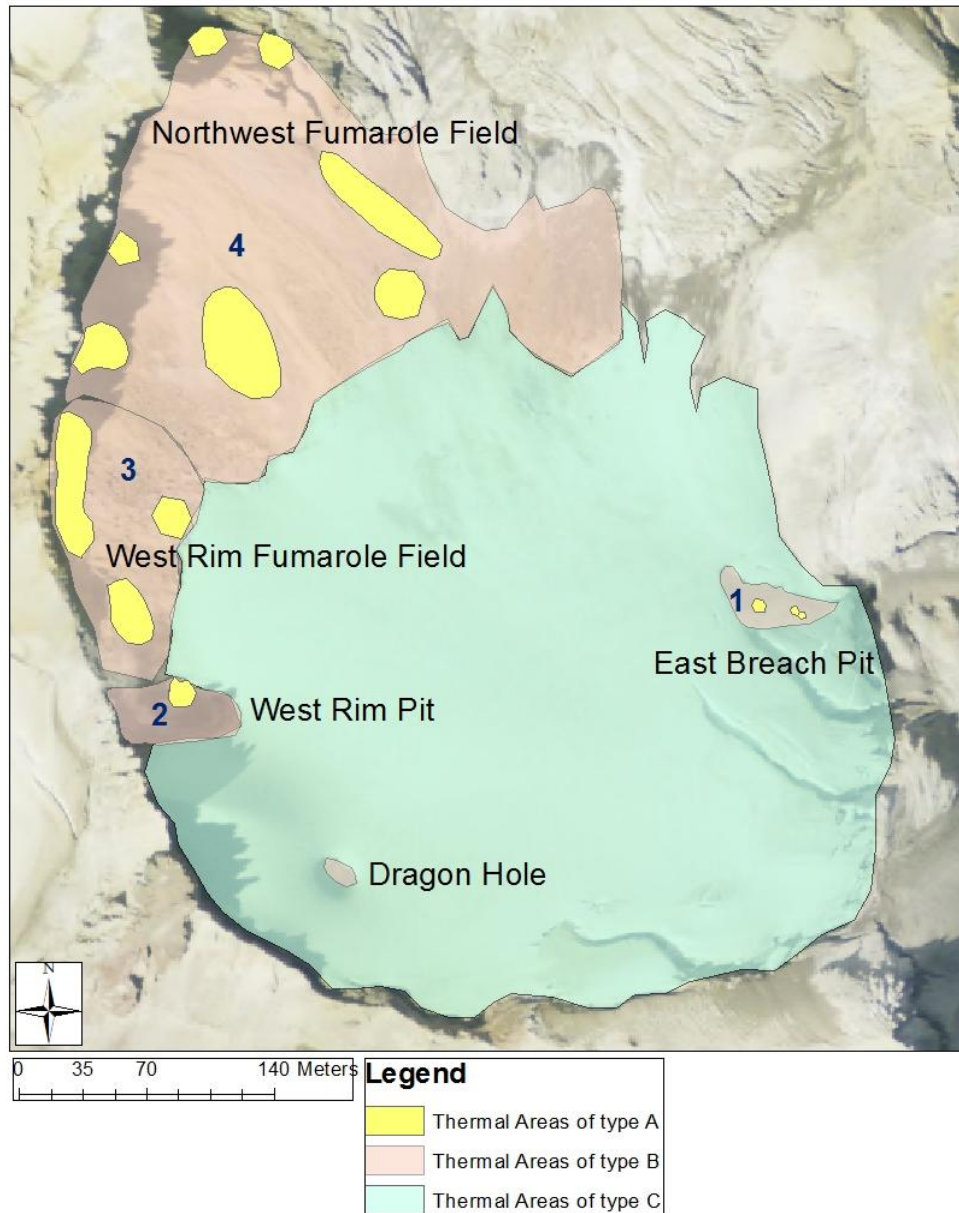


FIGURE 2. 9 – MAP OF THERMAL GROUNDS IN SHERMAN CRATER IN 2009

Thermal zones in the crater are identified as one of three types: Type A, snow free year-round, type B: snow free in the summer and type C: snow-covered year-round. We estimate the approximate size and location of these thermal grounds based on aerial photographs and the above background orthographic imagery from July 2009 in ArcGIS. Background photo by NAIP, digital orthographic imagery, 2009

3 – FIELD DATA

3.1 – ABLATION STAKES

Three 6-meter and twelve 3-meter stakes were inserted into the glacier and geolocated in late May 2009. By mid-July one of the 3-meter stakes was completely melted out, but still lying on the glacier. One stake was forgotten. The remaining thirteen were measured for ablation. By August 5th, one of the 6-meter stakes was broken above the surface but still firmly imbedded in the glacier, two of the 3-meter stakes had disappeared and likely fell into the Dragon Hole and one was completely melted out but still lying on the surface. The broken stake was not measured for surface ablation, but was used in subsequent geolocation. By August 9th, one more of the 3-meter stakes had disappeared and three had melted out and fallen on the ice, limiting the final geolocation survey to only six stakes. The locations of the fallen stakes were also recorded. I used their imprecise coordinates in estimating ice flow directions, but did not include them in the calculation of ice flow velocity. (Table 3.1 and Figure 3.1)

3.1.1 – ACCUMULATION

Snow accumulated during the 2008-2009 snow season was measured in early May 2009 in three locations in the crater (Figure 3.1). They totaled 5.5, > 8.0, and 7.0 meters (Table 3.1) for a minimum average of 6.8 ± 1.0 . This average is a minimum because the depth to last year's layer was greater than the length of the probe (8 m) at stake ACC3, above the East Breach Pit. Because the density of the ice and snow at the surface of the glacier is unknown, I did not convert these values to water-equivalent depths.

A reasonable density estimate for snow and near-surface ice is 550-600 kg/m³ (Section 5.2.4). Based on this assumption, the W.E. accumulation for 2009 is ~3.8-4.0 m.

3.1.2 – ABLATION

During the first 45 days of the ablation season (May 31st to July 17th), the stakes still standing were exposed by an average of 1.6 ± 0.1 meters. During the subsequent 19 days (July 17th to August 5th) those stakes remaining in the ice were further exposed by an average of 1.6 ± 0.5 meters, for a total average surface melt over the summer fieldwork season (May to August; the full ablation season for 2009 lasted from May to mid-November) of 2.8 ± 1.1 meters (Table 3.1). The volume loss observed at the surface is likely due to melting, sublimation and compaction. Assuming a density for snow and near-surface ice is 550-600 kg/m³ (Section 5.2.4), the W.E. ablation for 2010 is ~1.5-1.7 m.

Total station measurements of stake locations (northing, easting and elevation) between May 31st and August 9th reveal an average decrease in elevation of 6.1 ± 0.6 meters for those stakes still standing. Included in this decrease are the loss of elevation due to downhill movement of the stakes and the loss of elevation due to basal melting and compaction. A residual loss in elevation ranging from 0.5 to 4.9 meters remains after measured ablation and estimated downhill movement are subtracted from the change in stakes' elevations (Table 3.1). Because the cause of this residual loss cannot be confirmed and because the precision in the z component of the total station data is less than that of the ablation stakes data (Table 3.1), annual mass-balance values were derived from stake data.

3.1.3 – GLACIER FLOW

Geolocation of stakes that survived the ablation season reveal an unexpected direction of ice flow. Surface topography estimated from GPS measurements collected in 2010 and from field observations suggests that ice should flow generally towards the East Breach on the southwest side of the ridge below Pooch Peak and towards the Northwestern Fumarole Field on the northeast side of that ridge (Figure 1.7). Stakes in the glacier, however, generally moved northward towards the Northwest Fumarole field, except for the three 6-meter stakes, which moved northeast towards the East Breach. These three stakes also migrated much shorter distances than their 3-meter counterparts (Figure 3.2). While the three 6-meter stakes moved ~3 meters down glacier, at an average velocity of ~6 cm/day, the 3-meter stakes moved ~10 meters, at an average velocity of 11 cm/day (Table 3.1; Figure 3.2).

3.2 – GPS DATA - SURFACE TOPOGRAPHY OF GLACIER

When plotted in Surfer 8.0, the 310 GPS waypoints collected in mid-July 2010 yield a surface topography map for the crater glacier that approximates my observations in the field. In particular, the ridge of snow that extends from below Pooch Peak to below the Dragon Hole, the small depression in the location of the Dragon Hole, the gentle slope from the ridge to the Northwest Fumarole Field and the steep slope up to Sherman Peak are present (Figure 3.3). Details in the glacier surface, however, are not captured (Figure 3.3).

3.3 – PROFILING GPR DATA – SIGNAL CHARACTER

Over the course of two fieldwork seasons, eight GPR transects were collected ranging in lengths from ~100 meters to ~300 meters. Most 2009 transects were collected along northeast-southwest lines approximately 40 meters apart (Figure 2.3). The 2010 data complements the 2009 data with

additional northwest-southeast transects and one north-south “diagonal” (Figure 2.3). These GPR data are available as Radan’s native .dzt files and as jpeg images in the CD appendix of this thesis.

3.3.1 – BASAL AND ENGLACIAL REFLECTORS

The most prevalent type of basal reflector is discontinuous, with a magnitude ranging from weak (low contrast against the background) to strong (high contrast) and a positive phase polarity (white-black-white). In profiles corrected for elevation, these resemble sets of short reflectors (less than a meter in length) stacked along diagonal lines (Figure 3.4 - A). These discontinuous reflectors are interrupted by continuous, strong, positive phase polarity reflectors (Figure 3.5 - E) several meters to several tens of meters in depths. In only one profile, collected in 2009, a weak continuous reflector of positive polarity can be discerned (Figure 3.4 - D)

I identified two types of primary englacial reflectors in the collected profiles. Continuous reflectors of medium contrast and positive polarity (Figure 3.4 - F) can be found in all profiles. These span distances from tens of meters to the entire length of a profile. In a few profiles, reflectors of this type only tens of meters in length appear stacked vertically for hundreds of nanoseconds (tens of meters in depth; Figure 3.4 - C). Englacial continuous reflectors of medium strength and reverse polarity can be found (Figure 3.4 - D) in most profiles. These reflectors typically appear slightly above the inferred base of the ice.

The distribution of different types of reflectors in the glacier reveals several groupings: the portions of profiles collected near the crater rims are characterized by strong, discontinuous reflectors (Figure 3.4 - A; Figure 3.5). The center of the glacier (Figure 3.5 - area CC) and the area above the East Breach Pit (Figure 3.5- area EB) are characterized by strong continuous basal reflectors (Figure 3.5 - E). Reflectors with reverse polarities (Figure 3.4 - D) are typically found on profiles collected in the proximity of fumarole pits such as the East Breach Pit and the West Rim Pit. Because the only discernable weak reflector (Figure 3.4 - D) was collected in 2009 as part of a set of data for which no precise coordinate is available, its location in the crater cannot be confidently identified. No weak reflectors could be found in the 2010 GPR profiles.

3.3.2 – INTERFERENCE SIGNALS

Two types of signals in the profiles appear to be interference, i.e., not related to actual subsurface features, and I therefore do not include them in my interpretations. One is vertically wider than normal reflectors, weak, and mimics the surface (Figure 3.6 - G). Another is a downward shift relative to the surface of the signal of approximately a thousand of nanoseconds over the length of

one to several scans (Figure 3.6 - H). This second type of signal is only observed in GPR profiles collected in 2010.

3.4 – CMP GPR DATA – EM WAVE VELOCITY

Two sets of CMP data ~ 20 scans in length (7 meters) were collected in mid-July 2009: one below Pooch Peak, one towards the center of the glacier, downglacier from the Dragon Hole. Although data collection was limited to a maximum offset of 7 meters by the length of the cable connecting the transceiver and receiver antennas, this small data is sufficient to estimate an average velocity for the crater glacier.

The CMP data collected below Pooch Peak yield a velocity for EM waves through ice faster than the speed of light, which is clearly inaccurate. These data were therefore discarded. The velocity of EM waves through the ice of the Sherman Crater glacier was therefore solely determined from CMP data collected downglacier from the Dragon Hole.

This set of data features numerous reflectors below the air-wave on the CMP profile: A few closely spaced reflectors within the first 100 ns, two prominent high-contrast reflectors at ~300 ns (englacial) and ~ 550 ns (basal), and several faint reflectors in between (Figure 2.5). Because Radan 6.0 does not allow magnification of profiles while in interactive mode (with the Depth Pick tool active), several “EZ-track” picks were applied for each noticeably distinct reflector. Each of the two prominent high-contrast reflectors (englacial and basal) resulted in straight lines with exactly the same slope on the ($x^2 - t^2$) graph despite slight differences in the manual picking of first onsets. For other reflectors in the profile, however, slight differences in the manual picking of first onsets resulted in widely different slopes (from -6 to +80). Two faint reflectors, one below the surface and one towards the base, produced reasonably consistent slopes on ($x^2 - t^2$) graph and were therefore included in the velocity calculations. Based on my calculations, the glacier can be divided in approximately four vertical sections pertaining to EM wave velocities. The ice just below the surface has a velocity of 0.160 m/ns. The section that extends to the high-contrast englacial reflector has a velocity of 0.240 m/ns. The two lower sections, from the englacial reflector to the base have velocities of 0.138 m/ns and 0.113 m/ns.

Because the location or existence of the high-contrast englacial reflector cannot be ascertained in all profiles, I opted to use the root-mean-square velocity from the surface to the base rather than use a four-layer velocity map for the crater glacier. The average velocity for EM waves through the Sherman Crater ice used for all time-to-depth conversions in this study therefore is 0.151 m/ns.

| Stake | Acc | Ablation in cm | | | Vertical corrected* | | | horiz. | downglac |
|-------|-----|----------------|---------|--------|-------------------------|-------------|------------|-----------|-----------|
| | May | May | Jul | summer | Theodolite measurements | | | velocity | velocity |
| | | -> July | -> Aug | | drop | horiz. move | total move | in cm/day | in cm/day |
| Acc2 | 545 | 218 | 485 | 703 | -586 | 334 | 674 | 4.77 | 5.06 |
| Acc3 | 800 | 201 | 238 | 439 | -671 | 461 | 814 | 6.59 | 7.38 |
| Acc4 | 700 | 213 | broken | >213 | -648 | 318 | 722 | 4.54 | 7.70 |
| 5 | | missing | missing | | | | | | |
| 6 | | 209 | 201 | 410 | -745 | 768 | 1070 | 10.97 | 11.97 |
| 7 | | 165 | 181 | 346 | -634 | 592 | 868 | 8.46 | 9.40 |
| 8 | | 170 | 140 | 310 | -567 | 645 | 859 | 9.21 | 9.92 |
| 9 | | 172 | missing | >172 | | | | | |
| 10 | | 150 | 236 | 386 | -603 | 796 | 998 | 11.37 | 11.79 |
| 11 | | 167 | down | >167 | | | | | |
| 12 | | 126 | 281 | 407 | -519 | 471 | 701 | 6.73 | 6.92 |
| 13 | | forgotten | 276 | >276 | -553 | 608 | 822 | | |
| 14 | | 187 | 271 | 458 | -604 | 564 | 826 | 8.06 | 8.32 |
| 15 | | 154 | 278 | 432 | | | | | |
| 16 | | 227 | missing | >227 | | | | | |
| BMR | | | | | 0 | 47 | 47 | | |
| SR | | | | | 0 | 7 | 7 | | |

*based on 0.81 m benchmark drop correction

| | | | | | | | | | |
|-----------------------------------|-----|-----|-----|-----|--|--|--|------|------|
| All | | | | | | | | | |
| Mean | 682 | 259 | 259 | 432 | | | | 7.07 | 7.86 |
| Stdev | 105 | 29 | 88 | 105 | | | | 3.21 | 3.49 |
| Stakes in which I have confidence | | | | | | | | | |
| Mean | | | | | | | | 6.99 | 7.93 |
| Stdev | | | | | | | | 3.57 | 3.94 |

TABLE 3. 1 – SUMMARY OF ABLATION STAKES AND TOTAL STATION DATA

Summary of ablation stakes and total station data collected, including accumulation measured in May, surface ablation measured in both July and August, stakes movements and calculated velocities. In grey are imprecise data. Accumulation and ablation values listed are actual measured data, not W.E. All data are in cm, except for velocity data in cm/day.

For details on formulas and corrections, see file “Table3_1_Stakesdata.xls” on the CD appendix.

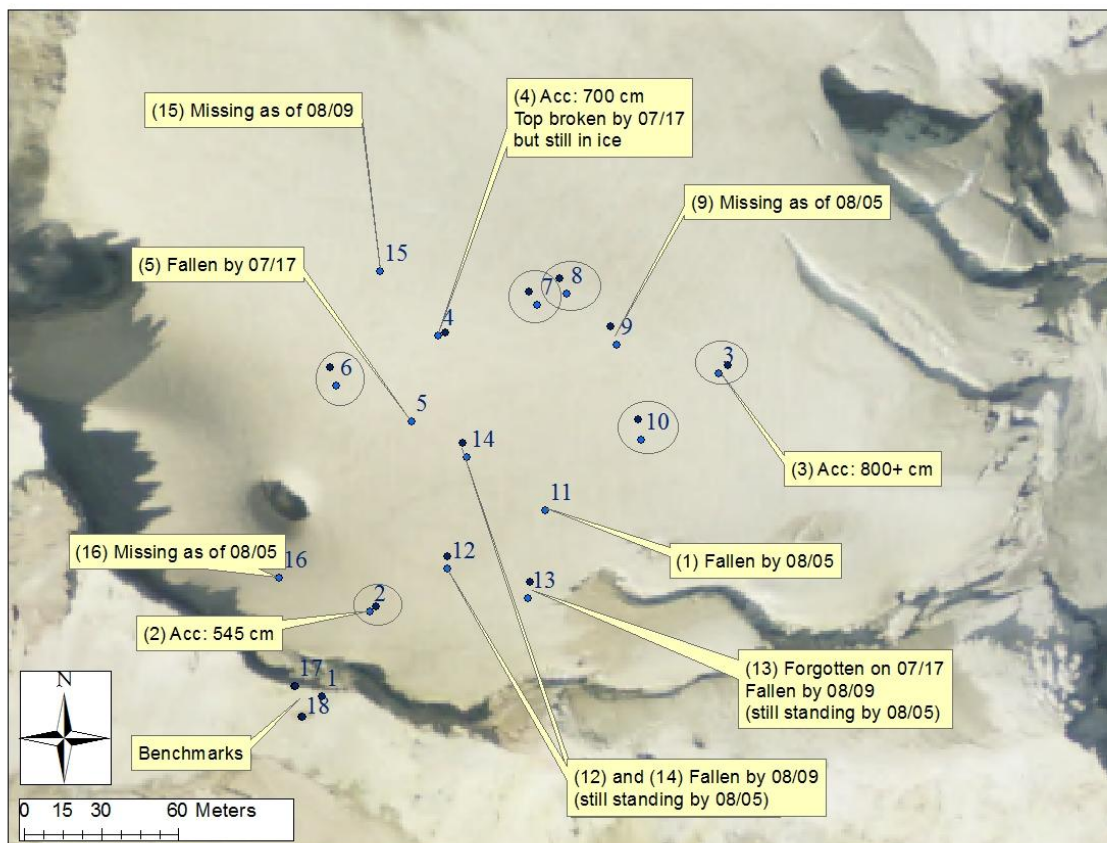


FIGURE 3. 1- ABLATION STAKE INVENTORY

Stakes 2, 3 and 4 are locations at which accumulation was measured. Those stakes that fell or disappeared at any date were not geolocated. Circled stakes are those for which a full set of data (surface ablation and geolocation) is available. Although a full set of data was collected for stakes 12 and 14, their geolocation is approximate and was not used in velocity calculations.

A)

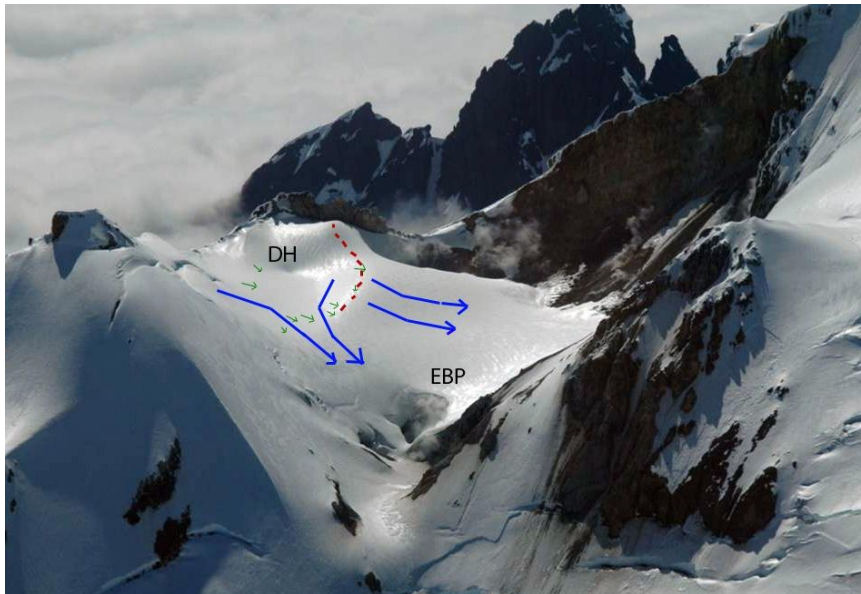
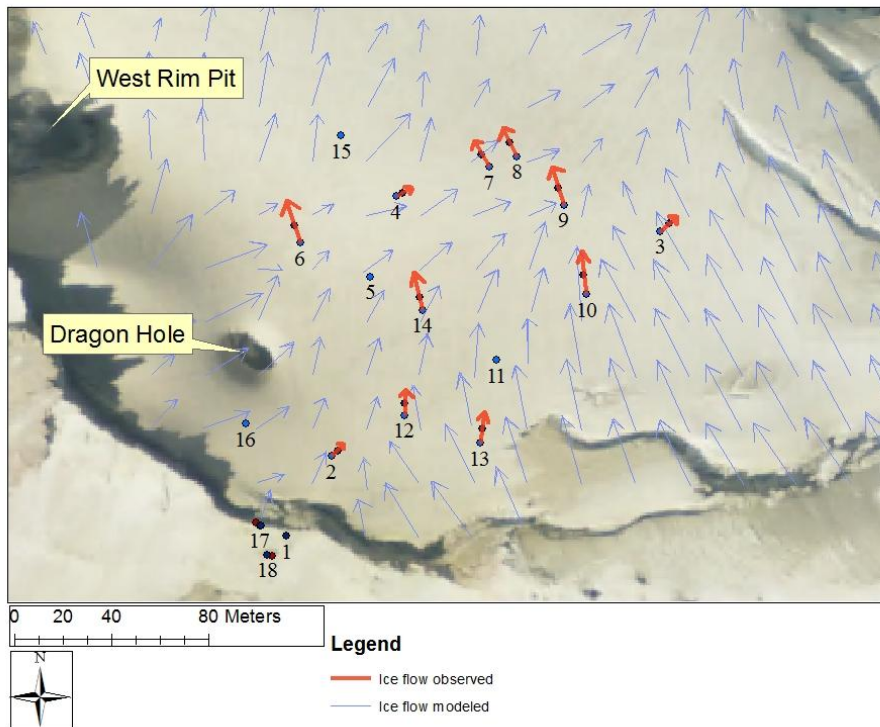


FIGURE 3. 2 – ABLATION STAKES MOVEMENT AND MODELED ICE MOTION

A) Ablation stakes movement between May and August 2009 (in red) compared to the modeled ice flow based on surface topography (light blue). B) Qualitative oblique view (to the west through the East Breach) of stakes movements (in green) compared to the modeled ice flow (bright blue).

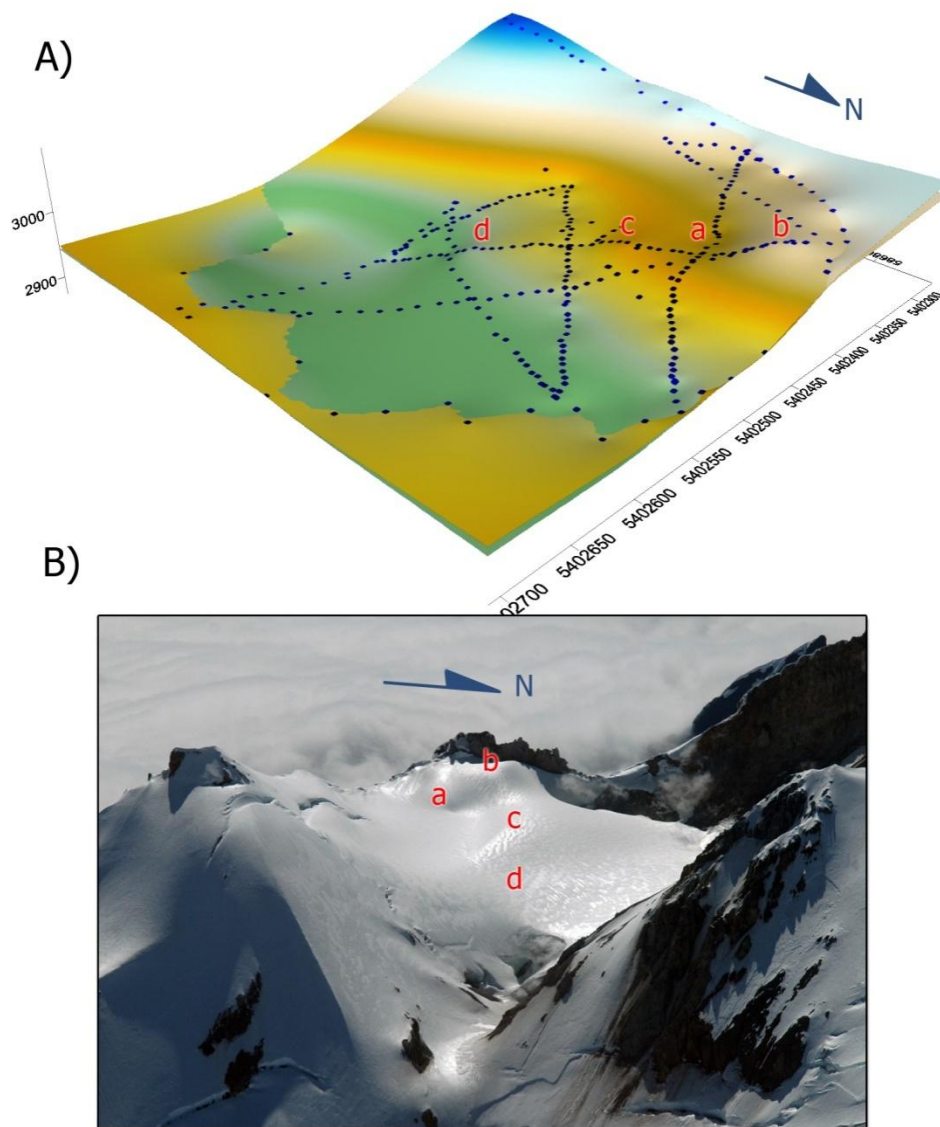


FIGURE 3.3 – SURFACE TOPOGRAPHY GENERATED FROM GPS WAYPOINTS

A) Surface topography generated from the plotting of 310 GPS waypoints (in blue), including waypoints gathered at the periphery of the glacier. Colors from green to blue represent various elevations. B) Surface features observable in the field: a) the Dragon Hole, b) the top of the ridge below Pooch Peak and c) a wide elevated ridge. The match is not perfect, however; note d) an elevated area on the plotted surface is actually a shallow trough.

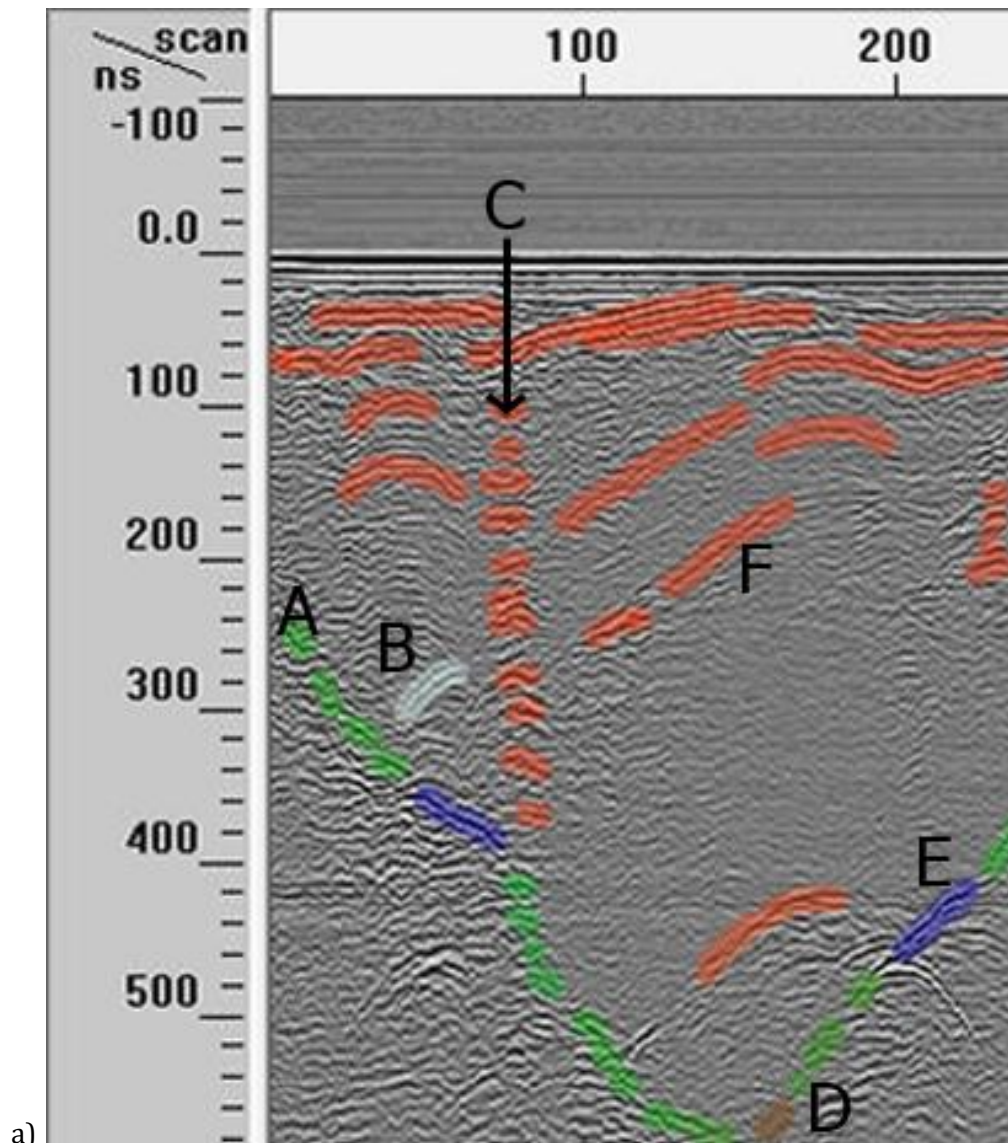
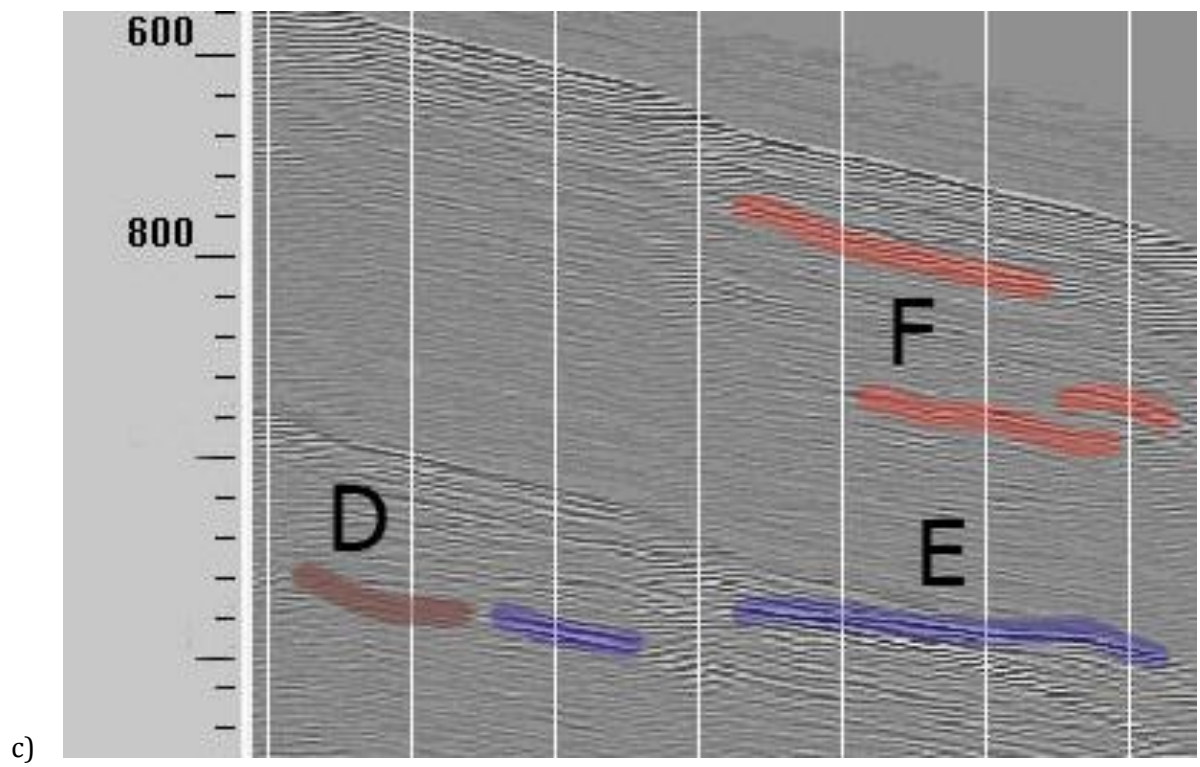
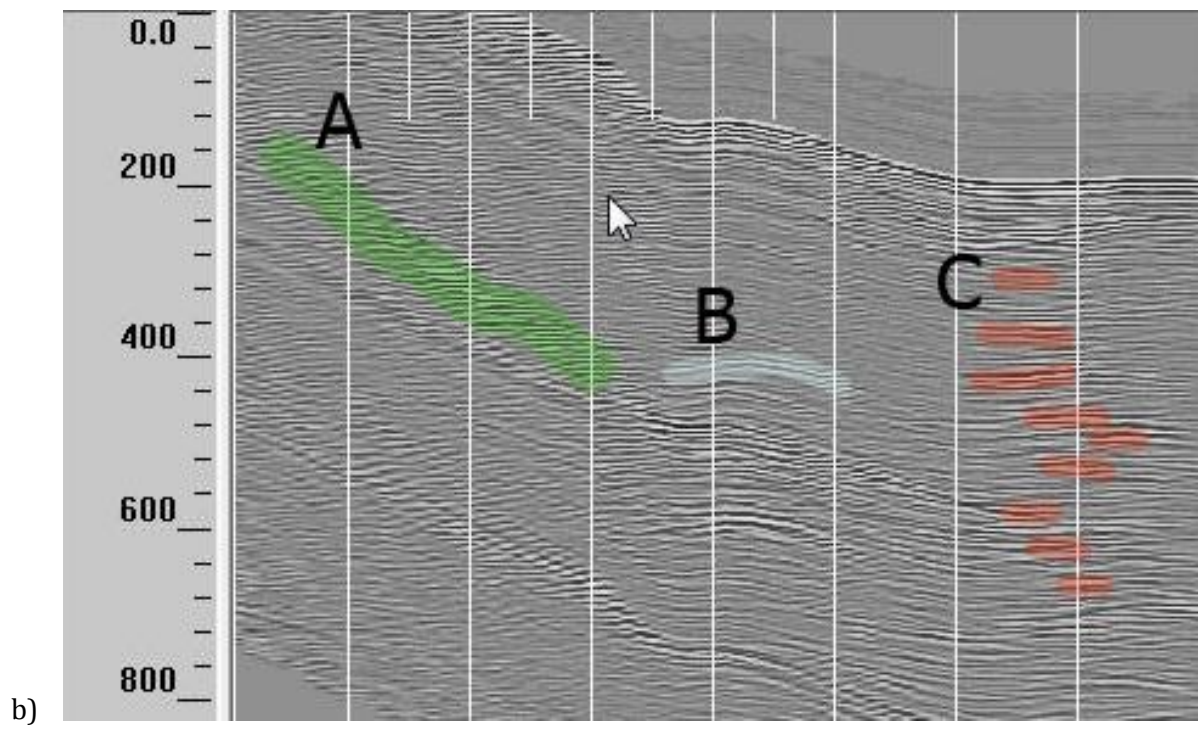


FIGURE 3. 4 - REFLECTOR TYPES IN ORIGINAL DATA

a) Reflectors as they appear in original data.

A) In green: discontinuous signal with a range of amplitude from weak to strong and a positive phase (white-black-white) is interpreted as ice/hydrothermally altered material. B) In white: phase reversal (black-white-black) above the base of the glacier is interpreted as ice/air interface (tunnels and cavities in the ice). C) In red: stacked englacial reflectors of medium contrast are interpreted as clearly revealed debris layers. D) In brown: weak yet continuous reflector with a positive polarity likely represents ice/bedrock interface. E) In blue: strong, continuous positive polarity signals are interpreted as ice/water interfaces. F) In red: englacial reflectors of medium strength and positive polarity are likely layers of debris related to summer debris accumulation.



b) and c) Reflectors as they appear in stretched profiles corrected for surface elevations.

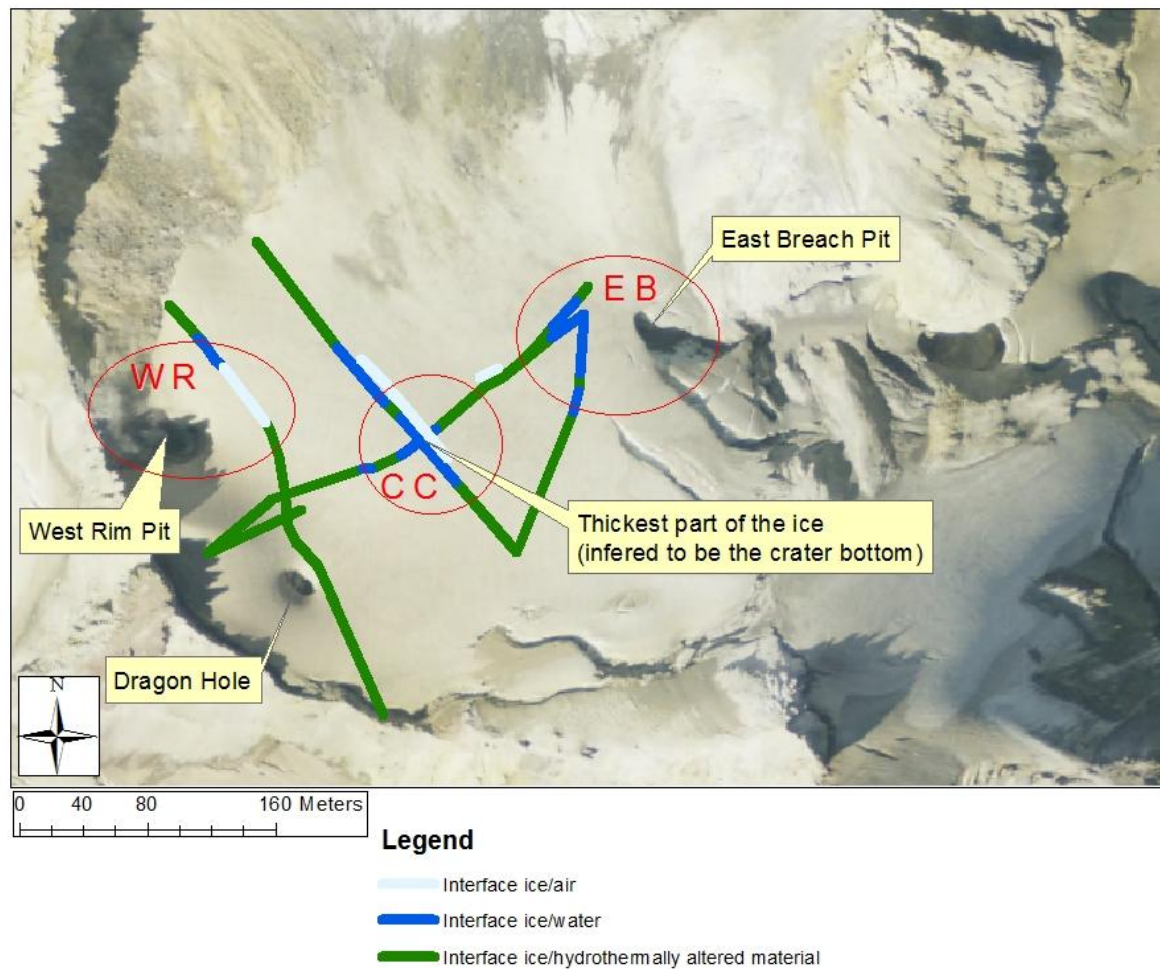


FIGURE 3. 5 - DISTRIBUTION OF REFLECTOR TYPES ALONG 2010 GPR TRANSECTS

Areas of interest are:

WR) Near the West Rim Pit, reflector of medium contrast with a negative polarity: englacial ice/air interface, likely corresponds to subglacial cave.

EB) Near the East Breach, intersection of two transects and part of a 2009 line. All three have similar strong continuous reflectors inferred to be ice/water interfaces.

CC) Center of the crater, intersection of two transects. All lines have strong continuous reflectors and reflectors of medium contrast and reverse polarity inferred to be ice/water and ice/air interfaces respectively.

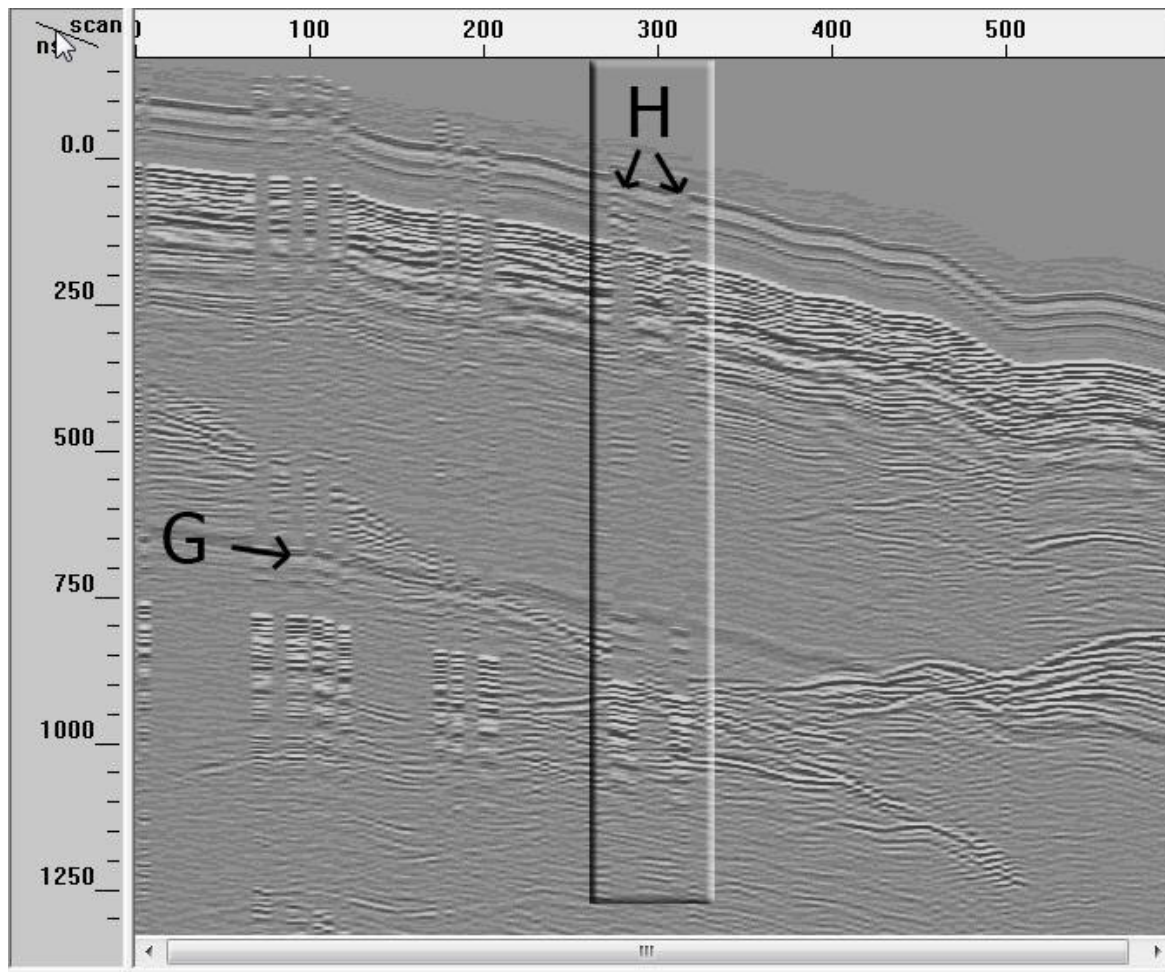


FIGURE 3. 6 - EXAMPLES OF INTERFERENCE SIGNALS

G: Vertically wide signal parallel to surface interpreted as false reflector caused by ringing in the antenna

H: Vertical shift over the length of several scans interpreted as electrical short circuit in the antenna

4 – CRATER AND CRATER GLACIER CHARACTERISTICS

4.1 – MAXIMUM DEPTH, GLACIER AREA AND ICE VOLUME

4.1.1 – MAXIMUM DEPTH

The maximum ice depth measured along GPR transects collected in 2010, assuming an EM wave velocity of 0.151 m/ns, is 71 ± 5 m (Table 4.1). This maximum is located approximately in the geographic center of the crater, ~75 meters southwest of the location of the Central Pit in 1975 (Figure 4.1; Frank et al., 1977). Ice depth data measured in the 2009 GPR profiles yield a maximum depth of 58 ± 5 m (Table 4.1). This maximum depth is located ~45 m southeast of the maximum depth in 2010 (Figure 4.1). The large depth difference between the two years likely reflects extremes in the weather pattern: The summer of 2009 was the second hottest in the past decade; the summer of 2010 the coldest (NOAA, 2009). Because errors in the geolocations of 2009 GPR scans are substantial, I favor the location indicated by the 2010 data (Figure 4.1).

Field observations suggest that the exceptionally hot summer of 2009 resulted in the melting of most of the new accumulation for that year (despite the exceptionally high 2009-2010 accumulation season; Snotel, 2011)). I therefore assume the snowpack to be likely compacted to an average of 700 kg/m^3 by mid-July, when GPR profiles were collected. Under this assumption, the water-equivalent (W.E.) maximum measured depth for 2009 is 40 ± 4 m. The summer of 2010, however, was unusually cold, following a slightly above average, but not exceptional accumulation season. Field observations suggest that much of the new accumulated snow did not melt by July 2010, when GPR profiles were collected. The added depth between the two years therefore likely results from an increase in surface uncompacted snow. Assuming a density of 600 kg/m^3 for this surface snow and 700 kg/m^3 for the rest of the glacier, the maximum depth of 2010 is 66 ± 4 m W.E. (Figure 4.1; Table 4.1)

4.1.2 – GLACIER SURFACE AREA

Based on a 2009 orthographic image of Mount Baker (NAIP, digital orthographic imagery, 2009), the surface area for the glacier that year is $\sim 119,000 \text{ m}^2$. GPS waypoints collected around the periphery of the glacier in 2010 yield a surface area of $\sim 125,000 \text{ m}^2$ (Table 4.1). This difference reflects extremes in the weather pattern for 2009 and 2010: the edge of the glacier melted further in 2009 than in 2010 particularly along the SWFF and NWFF thereby reducing the glacier's surface area.

4.1.3 – ICE VOLUME

Volume calculations in Surfer 8.0, based on ice depths measured in GPR profiles, yield a volume of snow and ice for the glacier of ~ 2.0 million m^3 for 2009 and ~ 3.1 million m^3 for 2010 (Table 4.1). Assuming a density of 700 kg/m^3 (following Frank et al., 1977; Section 4.1.1) for the extensively melted glacier of 2009, the W.E. volume for 2009 is ~ 1.3 million m^3 . Assuming a density for snow of 600 kg/m^3 (following Frank et al., 1977; section 4.1.1), the added volume in 2010 is 1.1 million m^3 , for a total volume of 2.7 million m^3 W.E. (Table 4.1)

Mathematical approximation of the glacier as a paraboloid (following Frank et al., 1977) yields a volume of 2.4 ± 0.4 million m^3 W.E. for 2009 (with a depth of ~ 40 m W.E. and a diameter of 195 m; appendix A and Table 4.1) and 4.1 ± 0.4 million m^3 W.E. for 2010 (with a depth of ~ 66 m W.E. and a diameter of 199 m; Table 4.1).

4.2 – ANNUAL MASS BALANCE

The minimum average of the three accumulation point measurements (5.45, > 8.00 , and 7.00 meters) is 6.8 ± 1.0 m (Section 3.1.1; Table 3.1). The total average volume loss due to surface melt and compaction over the summer fieldwork season is 2.8 ± 1.1 m (Section 3.1.2; Table 3.1). The annual mass balance for 2009 based on these data is 4.0 ± 1.5 m. This is the thickness per unit area of snow and ice added to the glacier over the course of the year.

Assuming that the surface volume loss due to sublimation, melting and compaction is relatively homogeneous across the glacier, and assuming that most melted ice percolates through the ice and is lost from the glacier (Frank, 1975), the resulting annual mass balance for the whole glacier is $\sim 480,000 \text{ m}^3$ of snow and ice in one year. This is the amount of snow and ice (D) that must be melted at the base in order for the glacier to remain in dynamic equilibrium ($D = \text{Annual mass balance}$ (4.0 ± 1.5 m) times the glacier area (118900 m^2); table 4.3).

4.3 – BASAL AND ENGLACIAL REFLECTORS

4.3.1 – BASAL REFLECTORS

The discontinuous reflectors (Figure 3.4 - A) predominant along the GPR transects (Figure 3.6) likely record the interface between ice and hydrothermally altered regolith. Field observations along the exposed crater rim and looking down to the base of the Dragon Hole indicate such material exists underneath the ice. Because hydrothermally altered regolith can be altered to different degrees, this material's dielectric constant can vary from ~ 10 to ~ 30 (Baker et al., 2007).

The reflection coefficient for the ice/hydrothermally altered regolith interface therefore varies from 0.23 to 0.52. The discontinuous appearance of the reflector representing this interface likely results from the juxtaposition of section of the reflector with reflection coefficients anywhere within this range.

The strongest continuous reflectors likely correspond to ice/water interfaces (Figure 3.5 – E). The transition from ice to water yields a reflection coefficient of 0.64-0.68, the highest amongst the possible transitions between materials in the crater. Because these strong continuous reflectors are located on portions of GPR transects near the West Rim Pit and through the center of the crater (Figure 3.6), I infer the presence of basal meltwater in these locations.

The lowest reflection coefficient amongst the possible interfaces between materials in the crater pertains to the ice/bedrock interface ($K=0.10-0.17$). Because the GPR also records reflectors below the base of the ice likely related to differences in the crater material, I infer the base of the ice in the section where a weak reflector can be discerned by assuming approximate continuity in the topography from surrounding strong reflectors. Only one example of this type of reflector (Figure 3.5 – D) can be found in a profile collected from approximately north of the East Breach Pit to Pooch Peak. None are apparent in profiles collected in 2010, possibly because interferences in the signal mask their presence.

Although it is not impossible that some of the ice base rests on bedrock, because of the pervasiveness of hydrothermal alteration in the crater and the presence of only one short reflector of such type in nine profiles, I conclude that this small reflector likely represents a section of the base hydrothermally altered in such a way as to produce little reflection of the EM wave velocity at its interface with ice.

Based on these inferences, the glacier base most likely rests on hydrothermally altered regolith, except in those locations where heat flux has created a thin layer of basal meltwater layers.

4.3.2 – ENGLACIAL REFLECTORS

The GSSI MLF-3200 antenna set to a center frequency of 80 MHz has a vertical resolution of ~ 0.5 m for an ice layer and $\sim 0.02-0.03$ m for a wet dust/debris layer ($1/4$ of the wave length λ). Debris layers thicker than 0.03 m should appear as continuous reflectors of medium strength. Such reflectors can be found in all profile (Figure 3.5 - F) and are likely related to annual englacial debris layers: such layers are visible in the walls of the Dragon Hole. In most profiles, the englacial reflectors are, however, too few to represent annual layers in the ice. They more likely represent

debris layers related to years with exceptional summer debris accumulation. Englacial debris layers in normal years are probably too thin to produce distinct reflectors. In a few profiles, numerous englacial reflectors inferred to represent debris layers appear for the length of one or two scans (a few meters; Figure 3.4 – C). In these sections, whether from a difference in wave attenuation as it travels through the ice or from a difference in how the data is recorded in the GPR, more of the englacial debris layers present in the ice are revealed. Such sections are common in published papers featuring GPR profiles, but I could not find any hypothesis related to their presence or existence.

Because no explanation could be found for those short sections of profiles where numerous englacial reflectors are apparent, my reflector analysis concentrated on those englacial reflectors several tens to hundred of meters in length apparent in all profiles (e.g., Figure 3.5 – F). Because some of these englacial reflectors appear as strong in magnitude as basal reflectors, they could be interpreted as side basal reflector (signal bouncing from the nearby crater rim, instead of the actual base of the ice). However, if these were side basal reflectors, their depth would appear greater in profiles further from the rim. This is not the case; the distribution of these strong englacial reflectors in relation to the surface is consistent in all profiles in which they appear: reflectors approximately in the middle of the ice also appear approximately in the middle of the ice in profiles where the ice is thinner. The depth at which they are found, however, is highly dependent on their location in the crater (Figure 4.2). Because GPR data collected in 2009 are not paired to exact locations, englacial reflectors observed in the 2009 data and in the 2010 data cannot be accurately matched for comparison. In addition, because the Dragon Hole did not open in 2010, I could not correlate visible dust bands in the hole to particular reflectors in the radar profiles. I was therefore unsuccessful in extracting information related to either the snow's compaction rate or glacial mass balance from englacial reflectors.

Continuous reflectors of medium magnitude and reverse polarity appear slightly above the inferred location for the base of the ice (Figure 3.4 – B). These reflectors likely represent ice/air interfaces related to ice caves and tunnels. The reversal of polarity (black-white-black; Reflection coefficient of -0.33 to -0.27) is the key to their identification.

4.3.3 – INTERFERENCE SIGNALS

Because the GSSI MLF 3200 antenna is unshielded, multiples appear in all profiles. Multiples are created by “ringing” in the antenna (Conyers, 2004) and appear as wide reflectors that mimic the air/ice interface signal (Figure 3.7 – G). When several multiples can be seen, the travel times at

which they are found are multiples, hence the name. In the profiles collected in 2009 and 2010, which range in depth from 0 to 1500 ns, the first multiple appears ~650 ns after the EM wave is sent (Figure 3.7 – G). The second multiple is faint and below the base of the ice and therefore of no concern to us.

Vertical shifts in the signal over the length on one to a few scans (Figure 3.5 - H) afflict the 2010 radar profiles: these are the result of a short-circuit in the antenna and do not reflect characteristics of the subsurface (GSSI technical support, 2010, personal communication).

4.4 – HEAT FLUX

4.4.1 – GEOTHERMAL GROUND INVENTORY

Aerial photographs of the crater taken in the early fall to late winter for the years 2009 to 2011 (Scurlock, written communication, 2011; Figure 4.2) and field observations over the summers from 2007 to 2010 (Tucker, written communications, 2011), reveal several areas of type A (snow free year-round; Figure 4.3): 1) the East Breach Pit has three small fumarole pits open in winter, one of which is likely the “Main Fumarole” mapped in Frank et al. (1977), 2) the West Rim Pit is open in winter but much smaller than in summer, 3) the West Rim Fumarole Field (WRFF) has three fumarole pits, and 4) the Northwest Fumarole Field (NWFF) has seven visible clusters of fumaroles (a through g in Figure 4.3). The largest fumarole clusters occur near Frank et al.’s (1977) Northwest Pit (f, Fig. 4.3) and in the areas to the east of Frank et al.’s (1977) North Pit (e and d, Fig. 4.3). Several small clusters occur at the base of the cliff that looms over the crater to the northwest. The total area for year-round snow-free ground in the NWFF is ~7800 m² (Table 4.2)

The remainder of the East Breach Pit, West Rim Pit, WRFF and NWFF, only snow-free during the summer months, is classified as thermal ground of type B, and covers ~45000 m² of the crater. The Dragon Hole is also of type B, even though it can appear as a mere depression in the snow during some exceptional years, such as 2010, with an area of ~165 m² (Figure 4.4, Table 4.2).

Any area still covered in snow in July, when the orthographic photo was taken, is classified as thermal ground of type C (Figure 4.4). The total surface area for the glacier is estimated at ~119000 m² for 2009 (Table 4.2; Section 4.1.2). The glacier has only a few crevasses, concentrated near the East Breach and below Sherman Peak. These crevasses do not appear to account for much total extension and were not included in the glacier mass loss calculations.

4.4.2 – HEAT FLUX CALCULATIONS

4.4.2.1 – Welch et al. (2007) calorimetric method

The Welch et al. (2007) method for calculating heat flux assumes that all heat flux goes into the melting of the glacier. Because approximately 30% of Sherman Crater in the summer is snow-free, I consider two options: 1) the loss of glacier volume observed in summer results only from the heat flux under the glacier (including the Dragon Hole, West Rim Pit and East Breach Pit), but the resulting heat flux can be extrapolated to the entire crater (i.e. if the glacier was thicker, it would not completely melt out in the SWFF and NWFF, but experience a volume loss similar to that observed in the rest of the glacier) and 2) the loss of glacier volume observed in summer is also the result of heat flux in the SWFF and NWFF through melting at the edge, thinning of the glacier and advection in steam plumes.

Under the first assumption, the method of Welch et al. (2007) yields a heat flux of $27.7 \pm 5.6 \text{ W/m}^2$ (Table 4.3). This value is calculated from an estimated 4.0 m of melted basal ice in a year over the area of the glacier ($\sim 119000 \text{ m}^2$). The melt rate therefore is 331 million kg/yr (11.2 kg/s) and the rate of heat flow is 3.5 MW. If this flux emanates from the entire crater, the heat flux is 27.7 W/m^2 (Table 4.3). To estimate the range of uncertainty, I calculate the heat flux for a depth of melted ice ranging from 2.6 m to 5.4 m ($4.0 \pm 1.4 \text{ m}$ – See section 4.2).

Under the second assumption, the method of Welch et al. (2007) yields a heat flux of $29.5 \pm 5.3 \text{ W/m}^2$ (Table 4.3). This value is calculated from an estimated 4.0 m of melted basal ice in a year over the area of the entire crater ($\sim 126000 \text{ m}^2$), which yields a melt rate of 352 million kg/yr (11.2 kg/s) and a rate of heat flow of 3.7 MW for the entire crater and a heat flux of 29.5 W/m^2 (Table 4.3). To estimate the range of uncertainty, I again calculate the heat flux for a depth of melted ice ranging from 2.6 m to 5.4 m ($4.0 \pm 1.4 \text{ m}$ – See section 4.2).

4.4.2.1 – Frank et al. (1977) thermal areas method

Using the method of Frank et al. (1977) method, heat flux is calculated for each type of area (A, B and C) in the crater for an average flux of $18.5 \pm 5.7 \text{ W/m}^2$ over the whole crater. The minimum total output for areas of type A, where active fumaroles melt snow as it falls, leaving patches of bare ground even in the heart of winter is 3.3 MW (Table 4.2). Areas of type B produce a minimum of 2.3 MW, exposing an additional $\sim 45000 \text{ m}^2$ of bare ground in the crater in the summer (Table 4.2). The glacier, which is the only area of type C in the crater, is melted at its base by a total of 3.5 MW (Section 4.2; Table 4.2).

The heat flux for areas of type A and B could however be greater. The heat flux of 419 W/m^2 used for areas A is that estimated by White (1969) for fast snow melt and deemed appropriate by Frank et al. (1977) based on a typical rate of snowfall of 0.1 m (W.E) on Mount Baker. The heat flux calculated for areas of type B is the amount of heat required to melt the accumulation season's fresh snow. In both cases, heating certainly continues after bare ground is exposed. Heat flux could therefore be considerably larger, but to an unknown extent.

Based on these calculations, the crater as a whole releases 3.16 MW , which corresponds to a heat flux of 18.5 W/m^2 (Table 4.2). I estimate the range of uncertainty by calculating the heat flux using the extremes in the range of depth of ice melted yearly: $6.8 \pm 1.0 \text{ m}$ in areas of type B and $4.0 \pm 1.4 \text{ m}$ in areas of type C (Table 4.2). Because the heat flux assigned to areas of type A is calculated from the standard value of 419 W/m^2 and does not depend on a measured depth of melted ice, I do not have a range of values from which to calculate the uncertainty in the total heat flux for areas of type A.

4.5 – ICE FLOW

Although ice flow deduced from the measured movement of ablation stakes in the glacier differs from the modeled ice flow based on surface topography (Figure 3.2), it is consistent with the location of major heat sources in the crater and the flow direction indicated by crevasses.

Based on the geothermal ground inventory, the WRFF and NWFF combined represent the biggest source of heat in the crater, with a minimum total of 5.3 MW (3.2 MW for areas of type A, snow free year-round, and 2.1 MW for the remainder of the combined fields; Table 4.2), compared to only 3.8 MW for the rest of the crater (including the glacier, East Breach, West Rim Pit and Dragon Hole). Because glacial ice mass is lost to this higher heat flux, the mass gradient for the glacier is towards the north-northwest (towards the WRFF and NWFF; Figure 4.5), even for that portion of the glacier to the south side of the ridge below Pooch Peak, which surface flow modeling predicts should flow northeast towards the East Breach (Figure 3.2). Only stake number 4 moves in opposition to flow vectors predicted by the glacier mass-gradient hypothesis. This stake, however, was found broken yet still in the ice during the July fieldwork and displayed the smallest amount of horizontal movement, with only 7 meters compared to 8-10 meters for all the other stakes (Table 3.1). Whether and how its broken state affected its geolocation is uncertain, but it is sufficiently suspicious to justify discarding it from the data set.

Based on the surface topography, model ice should flow away from the ridge below Pooch Peak on both sides and radially inwards near the Dragon Hole (Figure 4.5). These surface features, however, appear to have little effect on the overall measured ice flow field. Although the heat generated at the base of the Dragon Hole is enough to create a local hole to the base most years, with only a surface area of 165 m² and localized rate of heat flow of 0.01 MW (Table 4.2), the extent of the melting is not significant enough to affect ice flow direction in that part of the crater. It is likely that the stake closest in proximity to (and up-glacier of) the Dragon Hole (stake 16) moved towards the hole, but that stake had melted out and disappeared by August, before the survey of stakes' locations (Figure 3.1). As for the snow ridge, GPR profiles collected across its crest reveal no subglacial ridge beneath the ice. Its existence is therefore most likely the result of higher accumulation. Because the snow ridge sits directly to the east of Pooch Peak, the highest point along the western rim, flanked by two topographic saddles, and because storms on Mount Baker usually come from the west (Gardner et al., 1995 – Figure 2), it stands to reason that the snow ridge is the result of a high snow-deposition zone in the wind shadow behind Pooch Peak. If the majority of this topographic ridge is snow (rather than ice), the effect of this high-accumulation ridge on ice flow is likely inconsequential compared to the overall mass-gradient of the glacier. In addition, the size of the ridge might be insufficient to affect the overall flow gradient.

No data could safely be gathered on the steep slope below Sherman Peak, so vectors in the flow model for that area are extrapolated from data gathered at least a hundred meter away and are therefore unreliable (Figure 4.5).

| | 2009 real | 2009 water- equ | 2010 real | 2010 water-equ | Pre-75 ⁽⁷⁾ water- equ | 1975 ⁽⁷⁾ water- equ | |
|---|--------------|-----------------------|--------------|-------------------|--|--------------------------------------|------------------------------|
| Maximum depth ⁽¹⁾ | 58±5 | 40±4 | 71±5 | 66±4 | 28-35 | | in m |
| Surface area ⁽²⁾ and ⁽³⁾ | 118900±7000 | | 125000±7000 | | 156000 | 137000 | in m ² |
| Calculated radius ⁽⁴⁾ | ~195 | | ~199 | | | | in m |
| Volume measured ⁽⁵⁾ | ~2.0 | ~1.3 | ~3.1 | ~2.7 | | | in million m ³ |
| Volume calculated ⁽⁶⁾ | 3.4±0.4 | 2.4±0.4 | 4.4±0.4 | 4.1±0.4 | 2.2-2.7 | 1.2-1.7 | in million m ³ |
| <p>Water-equivalent calc assume an average snow and ice density of 700 kg/m³ for compacted snow (2009) and 600 kg/m³ for snow added volume between 2009 and 2010</p> <p>(1) Based on depth picks in GPR profiles</p> <p>(2) Area calculated in ArcGIS based on July 2009 ortho image</p> <p>(3) Area calculated in ArcGIS based on GPS data collected in July 2010</p> <p>(4) $r = \sqrt{\text{Surface}/\pi}$</p> <p>(5) Volume calculated in Surfer 8.0 based on depth contour maps created from depths picks and GPS waypoints of glacier contour</p> <p>(6) Volume calculated mathematically using a paraboloid of rotation (see Appendix A)</p> <p>(7) Based on Frank et al., 1977</p> | | | | | | | |

TABLE 4. 1 – SUMMARY OF GLACIER CHARACTERISTICS

Summary of glacier characteristics (depth, radius, surface and volume), including pre-1975 and 1975 data from Frank et al. (1977).

| | A | D | H | Notes |
|---|------------------------|------------------------|-------------------|---|
| Areas of type A | | ice and snow thickness | Rate of heat flow | |
| Locations | Area (m ²) | (m) | in MW | A from GIS area tool |
| 1) 3 clusters in the East Breach Pit | 79 | | 0.03 | H=419 W/m ² * A |
| 2) West Rim pit | 184 | | 0.08 | |
| 3) West Rim Fumarole Field | 2291 | | 0.96 | |
| NWFF - a | 641 | | 0.27 | |
| NWFF - b | 353 | | 0.15 | |
| NWFF - c | 1297 | | 0.54 | |
| 4) Northwest Rim Fumarole Field | 5253 | | 2.20 | |
| NWFF - f | 1925 | | 0.81 | |
| NWFF - d | 611 | | 0.26 | |
| NWFF - e | 1374 | | 0.58 | |
| NWFF - g | 279 | | 0.12 | |
| NWFF - h | 252 | | 0.11 | |
| NWFF - i | 597 | | 0.25 | |
| NWFF - k | 215 | | 0.09 | |
| | 7807 | | 3.27 | |
| Areas of type B | | | | |
| Locations | | | | A from GIS area tool |
| East Breach Pit | 1060 | 6.82 | 0.05 | h - snow accumulated that |
| Dragon Hole | 165 | 6.82 | 0.01 | year must melt to expose |
| West Rim Pit | 1852 | 6.82 | 0.09 | bare ground |
| West Rim Fumarole Field | 6046 | 6.82 | 0.31 | |
| Northwest fumarole Field | 35666 | 6.82 | 1.80 | |
| | 44789 | | 2.26 | |
| Areas of type C - with measured melt | | | | |
| Remainder of crater glacier | 117721 | 3.98 | 3.49 | A from GIS area tool h - amount of basal melt calculated |

Rate of heat flow - weighted average for the crater (in MW)

3.16

Heat flux of the crater (in W/m²)

18.54

±5.68

TABLE 4. 2 – HEAT FLUX CALCULATIONS USING THE METHOD OF FRANK ET AL. (1977)

This table also includes an inventory of thermal zones shown in Figure 4.3. For details on formulas and error uncertainty calculations, see file “Table4_2_heatfluxfrank.xls” on the CD appendix.

A)

| <u>H = L * Melt rate</u> | | <u>Where does it come from?</u> |
|---|-------------|---------------------------------|
| H = Heat Flux in W/m ² | 27.7 | =Ht*1000000/A |
| Ht = Rate of heat flow (in MW) | 3.5 | =Melt Rate/1000000 |
| L = Latent heat of fusion for ice, 333550 J/kg (Welch et al., 2007) | | |
| Melt rate = Dm/t in kg/s | 10.5 | = Dm/t |
| t = seconds in a year (31,557,600 s in a Julian year) | | |
| <u>Dm = D*ρ ice</u> | 331000000.0 | = D*ρ ice |
| Dm = Mass of melted basal ice in a year (in kg) | | |
| D = Vol of basal melted ice = annual mass balance (in m ³) | 473405.1 | =h*A |
| ρ ice = Density of basal ice ~ 700 kg/m ³ (Frank et al., 1977) | | |
| ρ water = Density of water at 0° C ~ 916.7 kg/m ³ | | |
| h -> volume of snow and ice melted(m ³ melted per m ²) | 4.0 | Measured in crater see 4.3 |
| Ag -> Glacier area (in m ²) | 118946.0 | Measured in GIS |
| A -> Crater area (in m ²) | 126490.0 | Measured in GIS |

B)

| <u>H = L * Melt rate</u> | | <u>Where does it come from?</u> |
|---|-------------|---------------------------------|
| H = Heat flux in W/m ² | 29.5 | =Ht*1000000/A |
| Ht = Rate of heat flow (in MW) | 3.5 | =Melt Rate/1000000 |
| L = Latent heat of fusion for ice, 333550 J/kg (Welch et al., 2007) | | |
| Melt rate = Dm/t in kg/s | 10.5 | = Dm/t |
| t = seconds in a year (31,557,600 s in a Julian year) | | |
| <u>Dm = D*ρ ice</u> | 331000000.0 | = D*ρ ice |
| Dm = Mass of melted basal ice in a year (in kg) | | |
| D = Vol of basal melted ice = annual mass balance (in m ³) | 473405.1 | =h*A |
| ρ ice = Density of basal ice ~ 700 kg/m ³ (Frank et al., 1977) | | |
| ρ water = Density of water at 0° C ~ 916.7 kg/m ³ | | |
| h -> volume of snow and ice melted(m ³ melted per m ²) | 3.98 | Measured in crater see 4.3 |
| Ag -> Glacier area (in m ²) | 126490.0 | Measured in GIS |
| A -> Crater area (in m ²) | 126490.0 | Measured in GIS |

TABLE 4. 3 – HEAT FLUX CALCULATIONS USING THE METHOD OF WELCH ET AL. (2007)

A) assuming that the melting is only the result of heat flux under the glacier.

B) assuming that the entire crater contributes to the melting of the glacier, even those areas that are venting to the air.

For details on formulas and uncertainty calculations, see file “Table4_3_heatfluxWelch.xls” on the CD appendix.

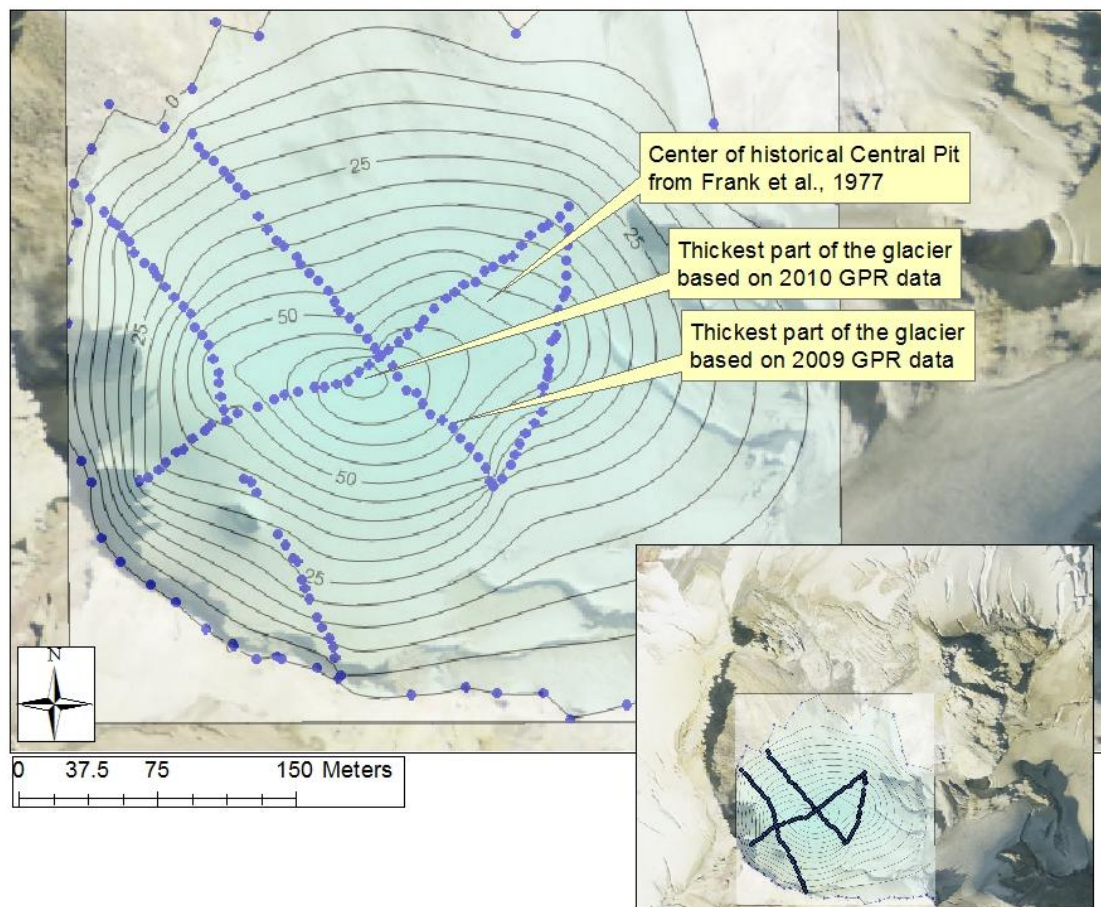


FIGURE 4. 1 – ICE THICKNESS CONTOUR MAP

Ice thickness contour map, assuming a velocity for EM waves through ice of 0.151 m/ns, for GPR scans collected in 2010 for which a GPS waypoint was recorded (measured depths, not water-equivalent). This map also indicates the location of the inferred thickest ice in 2009 and the center of the historical Central Pit as mapped in Frank et al., 1977. Thickness contour interval is 5 m.

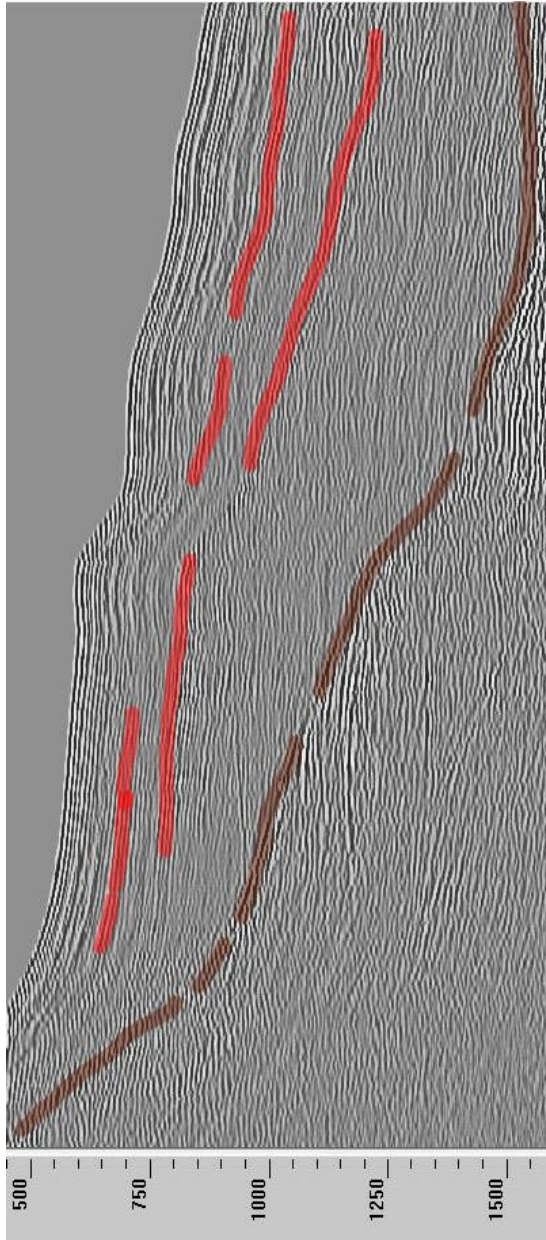


FIGURE 4. 2 – EXAMPLE OF ENGLACIAL REFLECTORS IN GPR PROFILES

Example of englacial reflectors (in red). Ice/base contact is indicated in brown. At the thickest part of the ice in this profile collected in 2009, the strongest englacial reflector appears ~30 meters from the surface and ~30 meters from the base. A slightly weaker reflector appears ~15 meters from the surface and ~45 meters from the base. Vertical scale in ns.

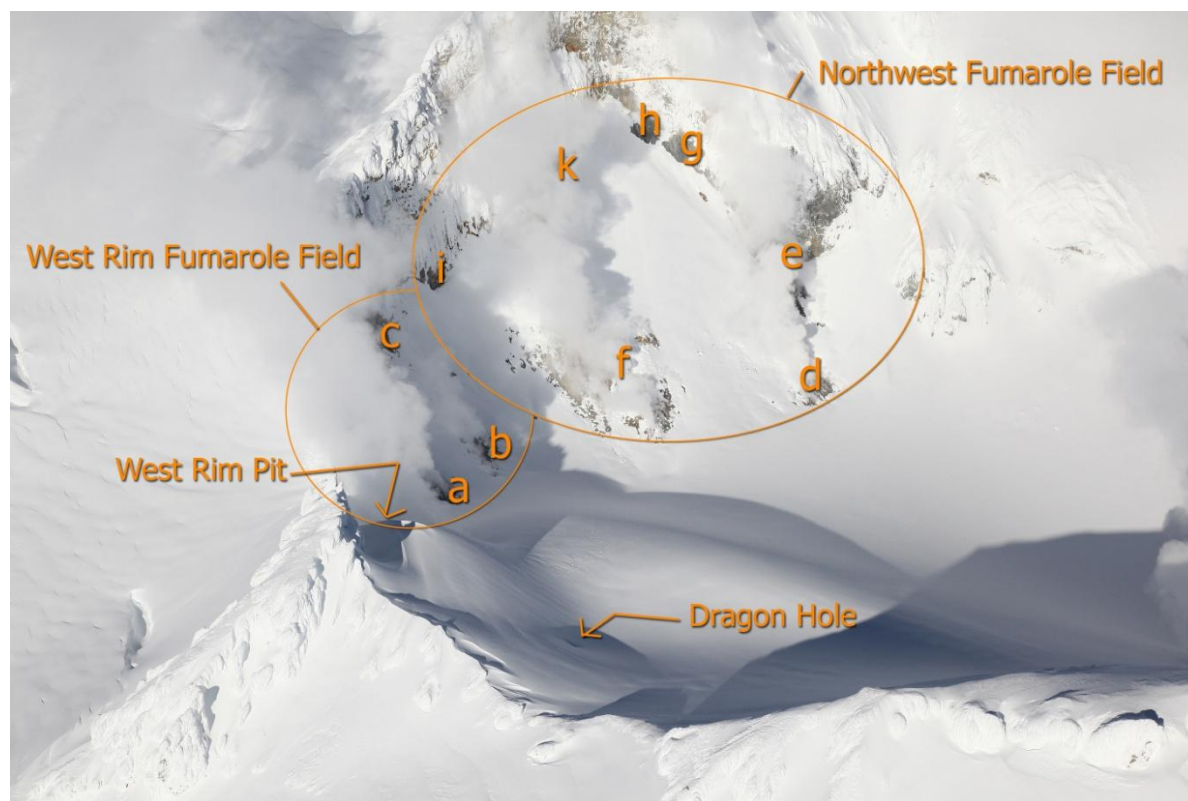


FIGURE 4. 3 - OBLIQUE AERIAL PHOTOGRAPH OF THERMAL ZONES OF TYPE A

Example of winter aerial photograph from which the location of thermal ground of different types is inferred. This photo from January 2011 reveals the areas of type A in the West Rim Fumarole Field (WRFF) and the Northwest Fumarole Field (NWFF). These zones are correlated between photos from different angles, varying in time from November 2009 to January 2011 (Tucker and Scurlock, 2011, personal communication; Photo by John Scurlock, 2011).

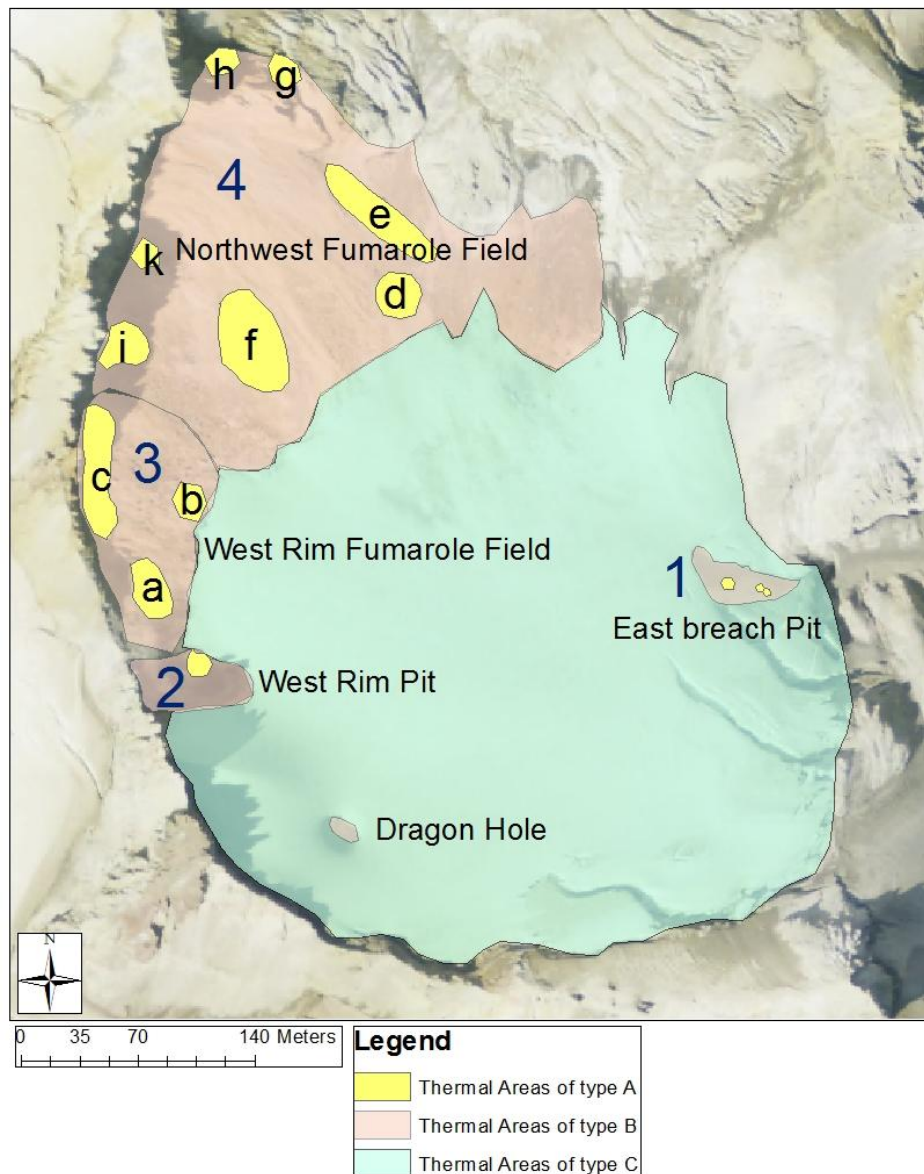


FIGURE 4. 4 - THERMAL ZONES INVENTORY: TYPES A, B AND C

Thermal zones in the crater are identified as one of three types: Type A, snow free year-round, type B: snow free in the summer and type C: snow- or ice-covered year-round. The approximate size and location of these thermal zones are based on aerial photographs and the above orthographic imagery from July 2009 in ArcGIS.

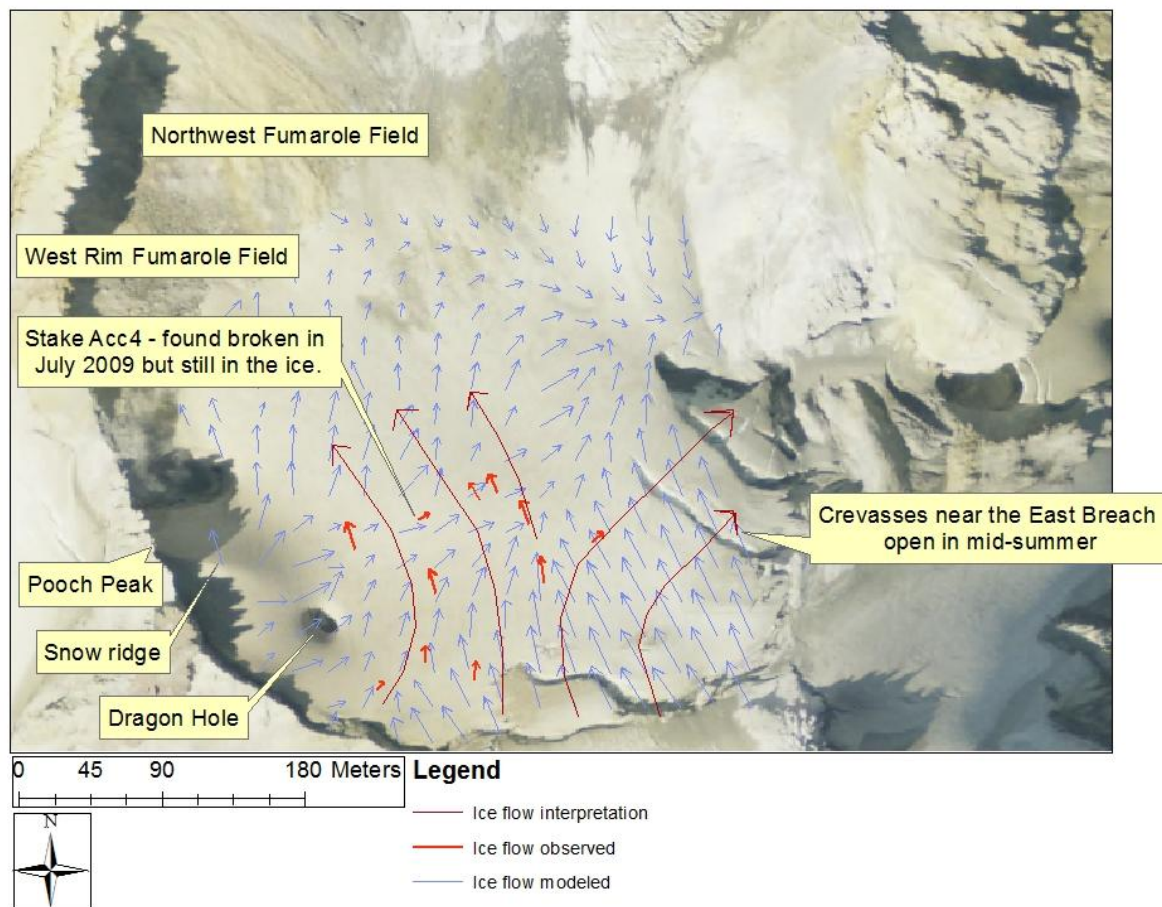


FIGURE 4. 5 – ICE FLOW VECTOR MAP

Ice flow vector fields: interpreted, observed and modeled observations. This map highlights the WRFF and NWFF, inferred to be the main zone of ablation and the cause of an apparent north-northwest trending glacier mass gradient, Pooch Peak, which creates a ridge of enhanced wind-drifted accumulation, and crevasses above the East Breach, which confirm direction of extension of the glacier in that area of the crater.

5 - DISCUSSION

5.1 – ICE MOTION

5.1.1 – TOTAL STATION MEASUREMENT UNCERTAINTIES

Despite careful placement and setup of the Leica total station, the coordinates of two purportedly fixed benchmarks (BMR and SR in Figure 2.1) surveyed in May and August 2009 differ both in elevation (downward shift of ~ 80 cm for both benchmarks) and azimuth (47 cm 0.96 degrees west for benchmark BMR, 7 cm 0.05 degrees west for benchmark SR). Because the BM, BMR and SR benchmarks were notches in apparently solid rocks on a mostly hydrothermally altered crater rim, the shifts in coordinates recorded could be attributed to movement of the rocks holding the benchmarks, errors in the total station setup or both.

The vertical drop of ~80 cm observed for both BMR and SR benchmarks between May and August is more likely the result of an error in the setup of the total station's height from the ground during the August survey than a coincidentally similar drop of both rocks. The stakes data were corrected accordingly. It is highly unlikely, however, that an incorrect placement or setup of the total station produced the apparent azimuth shifts. One or both of the benchmarks likely moved. Although no instability of the rock holding the BMR benchmark was discernable in 2009, by July 2010 it appeared fractured and by August 2010 it had completely disintegrated. I therefore attributed the BMR benchmark's apparent azimuth shift to benchmark movement and did not apply any related correction to the stakes data. The rock on which the SR benchmark was located appeared stationary throughout, but this benchmark's apparent azimuth shift is only 7 cm 0.05 degrees west; this change would be indiscernible to the eye. An error in the total station's calibration of the north azimuth during the August survey could produce the observed shift for benchmark SR. An error of 0.05 degrees at the BM benchmark would result in a difference of ~20 cm for the furthest stake from the total station. Because I could not ascertain whether the SR benchmark change of coordinates was the result of benchmark movement or error in the total station setup, I did not apply any correction to the stakes data based on the apparent SR benchmark shift. The maximum possible error of ~20 cm in stake location falls within the standard deviation of ~50 cm (Table 3.1), so I trust the data are still reasonably representative of the stakes' true movement and velocity.

5.1.2 – ICE VELOCITY COMPARED TO OTHER GLACIERS

Although studies of ice flow velocity abound in the literature, few focus on small (less than a few square kilometers) glaciers in active craters. The glacier most similar to Sherman Crater in terms of size and geographic setting is Crater Glacier ($\sim 0.6 \text{ km}^2$, 70 m in depth where not constricted by the growing rock spire; Walder et al., 2007) in the active crater of Mount St. Helens. Walder et al. (2007) report an average velocity of $\sim 20 \text{ cm/day}$ for the part of Crater Glacier downglacier from the domain that is being squeezed by the rock spire. These velocities represent an order of magnitude larger than those measured in Sherman Crater ($\sim 3 \text{ cm/day}$). Despite the similarities in terms of slope and thickness, however, the Crater Glacier is heavily debris-laden, closer in texture to a rock glacier than an alpine glacier (Walder et al., 2007). The higher mass of this ice-debris mixture is likely the cause of the recorded high velocities.

Muir (1973) measured an ice flow velocity of $\sim 3 \text{ cm/day}$ for the Maclure (McLure) Glacier, a $\sim 0.2 \text{ km}^2$ cirque glacier with a $\sim 20^\circ$ slope in the Sierras. Jacobel (1992) reports an ice velocity of $\sim 4 \text{ cm/day}$ for the South Cascade Glacier, a $\sim 2 \text{ km}^2$ glacier in a non-volcanic area of the Washington Cascades, and Benson (1971) reports $\sim 3 \text{ cm/day}$ for ice in the 15 km^2 active caldera of Mt. Wrangell in Alaska. These values are comparable to calculated ice flow velocities in Sherman Crater, despite differences in climatic and geologic setting, size and thickness between these glaciers and the glacier in Sherman Crater.

Benson (1971) also notes that ice flow in the caldera is clearly directed towards areas of higher heat flux, suggesting that the increased melting of ice leads to a mass-gradient towards areas of higher flux, as observed in Sherman Crater.

5.2 – ICE DEPTH AND GLACIER VOLUME

5.2.1 – GPR TIME-TO-DEPTH CONVERSIONS

Depth calculations and the derived volume of snow and ice for the glacier inside Sherman Crater are based on an EM wave velocity through ice of 0.151 m/ns . This value was calculated from CMP data collected in Sherman Crater as the root-mean-square velocity to the basal reflector (Section 3.4).

The difference in velocities in the ice column likely results from structural differences. Temperate glacier ice is a three-phase mixture of air, water and ice (Gusmeroli et al., 2008). Although the velocity of EM waves decreases through wet ice (velocity through water is 0.033 m/ns) and possibly debris layers (which can range from 0.055 m/ns for wet sand to 0.017 for wet clay),

Gusmeroli et al. (2008) found that EM-waves can travel through temperate ice that includes significant amount of air at velocities greater than the standard value for cold solid ice, 0.168 m/ns. The highest measured velocity in an air-inclusion-rich part of the temperate glacier Falljökul in Iceland was ~ 0.19 m/ns (Gusmeroli et al. 2008). Bradford et al. (2009) measured velocities through the high-water zone of the Bench Glacier, in Alaska, as low as 0.160 m/ns. Eder et al. (2008) measured a velocity through the wet temperate ice of the Hallstaetter Glacier in the Austrian Alps of 0.148 m/ns. Although no measurement of the amount of air or water in the glacier inside Sherman Crater is available, I deduce from these comparable values that the glacier's upper section, where lower density snow from recent accumulation is found, likely holds significant air inclusions, while the lower section, more closely subjected to geothermal flux, is likely water-saturated. The presence of thin meltwater layers at the base of the glacier, revealed in GPR profiles, further supports this hypothesis.

The average velocity of EM waves through ice of 0.151 m/ns calculated for the Sherman Crater glacier is lower than that used by Welch et al. (2007) on Mount Veniaminof. The velocity of 0.169 m/ns used on Mount Veniaminof is, however, a standard value calculated for cold pure ice and is not derived from actual measurements on the glacier. My data suggest the Sherman Crater glacier has a high water-content.

5.2.2 – WEATHER CONSIDERATIONS

GPR data used in my volume calculations for Sherman Crater were collected in July and August 2009 and in July 2010. The meaningfulness of these data depends in part on how typical these years were in terms of ice volume inside the crater, a factor of both their accumulation and ablation seasons.

The year 2009 was exceptional both in its accumulation and ablation seasons. Data gathered at three SNOTEL stations surrounding Mount Baker reveal 2008-2009 as the year with the second highest snow water equivalent accumulation in 15 years (Snotel, 2011; Figure 5.1), and the National Climatic Data Center lists 2009 as the second hottest summer in the past decade, with record highs in July and August for most of the Pacific Northwest (from Portland to Vancouver; NOAA, 2009). The accumulation for the winter of 2009-2010 was below average, but not exceptional (Snotel, 2011; Figure 5.1). The summer of 2010 was exceptionally cold, with temperatures below average for most of July and August (recorded at Sea-Tac; NOAA, 2010)

Field observations in Sherman Crater suggest that although 2008-2009 was a year of exceptionally high accumulation, the added volume did not offset the effects of the exceptionally hot summer that followed. On July 17th 2009, entry into the crater via the west rim required a rappel of ~7 meters down to the glacier. On July 17th 2010, the snow on the glacier was even with the crater's west rim. In mid-July 2007, a year with a more typical summer and only slightly above average snow water equivalent accumulation, entry into the crater via the west rim only required a 1-2 meter scramble down to the glacier. These observations highlight the delicate balance upon which the volume of ice in Sherman Crater depends. The volume measured in 2009 (~1.6 million m³ W.E.) is likely an underestimate of the average volume of ice in Sherman Crater, but because the accumulation season was exceptionally high, it is not an extreme low. The volume measured in 2010 (~2.4 million m³ W.E.) is likely an overestimate, but because the accumulation season was below average, it is not an extreme high.

5.2.3 – ICE DENSITY CONSIDERATIONS

Because ice volume calculations are primarily used to estimate meltwater volume and glacier mass, they are most useful when presented as water-equivalent volumes. Uncertainties in snow and ice densities in a small thin glacier such as that in Sherman Crater could significantly affect estimates of total water mass.

Kay (2006) reports that snow on the west slopes of the Cascades, which include Mount Baker, densifies quickly because of its high water content and exposure to mild atmospheric temperatures. Although densification rates vary across the western slopes of the Cascades, typical snow density by the end of the accumulation season is ~450 kg/m³ with a densification rate of ~ 50 kg/m³ per month as it accumulates (Kay, 2006). The densification rate is also a factor of accumulation: higher accumulation typical of higher elevations should therefore yield a higher densification rate (Kay, 2006). Using ~ 50 kg/m³ as a minimum densification rate and assuming that it is also applicable to the early ablation season (April to May), I calculate a likely minimum density for the snow and ice near the surface of the crater glacier by May 31st of 550 kg/m³.

If I consider extreme cases and assume that the density of ice at the base of the glacier can range from 700 kg/m³ to that of pure ice at the melting temperature, ~900 kg/m³, while the density of the surface snow can range from 550 kg/m³ to 700 kg/m³, and if I further assume that the densification is linear with depth, end member values for the range of possible average densities for the glacier are 625 kg/m³ and 800 kg/m³. The W.E. volumes calculated from these extremes yield a W.E.

volume of ~ 1.3 million m^3 to ~ 1.8 million m^3 for 2009 and ~ 2.2 million m^3 to ~ 2.8 million m^3 for 2010.

At an elevation of 2450 m in August, Peltó (2010) measured a density of 600 kg/m^3 on the Easton Glacier. Because Sherman Crater (elevation $\sim 2900 \text{ m}$) is at least 450 m higher than the location of Peltó's (2010) ice density measurements and because higher elevation corresponds to higher accumulation and higher densification rates (Kay, 2006), I expect the average ice density near the surface of the crater glacier to be higher than that measured by Peltó, but to an unknown extent. In addition, because ice in the glacier compacts with depth, even a surface density of $\sim 600 \text{ kg/m}^3$ would yield an average for the whole glacier higher than 600 kg/m^3 . Although no measurement of the ice near the base of any glacier on Mount Baker is available in the literature, it is unlikely that this density approaches that of pure ice, $\sim 900 \text{ kg/m}^3$. Observations in the Dragon Hole reveal layers of dense snow, rather than pure ice, from the surface to the base. GPR profiles also reveal a consistent type of ice throughout, with no increase in transparency related to a decrease in water content as could be expected in pure ice (Bradford et al., 2009). It therefore stands to reason that the end member values calculated above are unlikely to accurately represent the ice density of the crater glacier, and that the values of 600 kg/m^3 for surface snow and 700 kg/m^3 for an average for the whole glacier (following Frank et al., 1977) are likely reasonably close to the actual densities in the crater glacier.

5.2.4 – VOLUME COMPARISONS

Frank et al. (1977) approximated the glacier volume by calculating the volume of a paraboloid with a maximum depth of 18 to 35 m W.E. and a surface area of $\sim 164,000 \text{ m}^2$ (Table 4 in Frank et al., 1977). The resulting volume of total ice and snow is 2.2-2.7 million m^3 W.E. for the pre-1975 glacier and 1.2-1.7 million m^3 W.E. for the half-melted glacier in 1975. These values are apparently close to those calculated in 2009 and 2010: ~ 1.3 and ~ 2.1 million m^3 W.E. for 2009 and 2010 respectively, based on radar depths picks and ice periphery geolocation (section 4.1.2 and 4.1.3), and ~ 2.4 and ~ 4.1 million m^3 W.E. for 2009 and 2010 using the paraboloid approximation (Table 4.1).

Frank et al.'s (1977) calculation were based on an estimated maximum depth derived from sounding of the Central Pit when it appeared in 1975 (Frank, 2010, personal communication). Because no actual profile of the ice base was available in 1975, how closely this depth represents the maximum thickness for the glacier is uncertain. The outline of the 1972 glacier's edge as it appears on Figure 19 in Frank et al., (1977) is, however, higher by ~ 70 meters along the northwestern rim than it is in 2009-2010 (Figure 5.2). Assuming an unchanging crater subglacial

topography, this higher snowline suggests a much thicker glacier in pre-1975 than in 2009-2010. I therefore expect the volume of ice in Sherman Crater in 2009 and 2010 to be less than in pre-1975. Because Frank et al.'s (1977) calculated volumes are based on a measured depth likely not to be the maximum depth, caution should be exercised when comparing the calculated volumes for 2009 and 2010 and Frank et al.'s (1977) published volumes for pre-1975 and 1975.

A comparison between measured volumes in Surfer 8.0 and the paraboloid approximation reveals a tendency for the paraboloid approximation to yield greater volumes than those calculated in Surfer 8.0: ~80% greater in 2009 and ~60% greater in 2010 (Table 4.1). Because Surfer 8.0 derives volumes from differential analysis between a surface plane and a topographic map extrapolated from a set of depth measurements and GPS locations of the glacier periphery (Figure 2.8), while the only parameters in the paraboloid approximation are one of these depth measurements (the maximum) and a calculated radius based on measured surface area, it seems likely that volumes calculated in Surfer 8.0 are more accurate than those approximated mathematically.

5.2.5 – RECOMMENDATIONS FOR MORE ACCURATE VOLUME ESTIMATES

The use of GPR data to calculate the crater glacier volume is appropriate. Small changes in the data collection method could, however, greatly improve the accuracy of the final values. 1) GPR reflection profiling transects should be collected from rim to rim as much as safety allows to limit the need to extrapolate depths in areas where no depth picks are available. 2) CMP data should be collected in several locations on the glacier to determine the lateral distribution of EM wave velocities through ice in addition to the vertical distribution 3) In addition, vertical sounding for depth of the Dragon Hole could provide a baseline against which to compare radar depth picks. Other fumarole pits seem unsafe for sounding due to active degassing of harmful chemicals in a confined part of the glacier (e.g. the East Breach Pit) or surrounding undercut ice shelves (e.g. the West Rim Pit). 4) Snow and ice density should be measured during field work both at the surface and at depth if possible, to improve estimates of water-equivalent volumes.

5.3 – MASS BALANCE

5.3.1 – COMPARABLE ACCUMULATION AND ABLATION RATES

Assessing the reasonability of the accumulation (6.8 ± 1.0 ; Section 3.1.1), surface ablation (2.8 ± 1.1 m; Section 3.1.2) and resulting annual mass balance (4.0 ± 1.5 m; Section 4.2) measured in Sherman Crater is hampered by a lack of comparable data. The glacier in Sherman Crater, at an elevation of 2900 m, lies entirely above the ELA for Mount Baker and at a higher elevation than the accumulation zone of most other glaciers on the mountain.

The best comparable accumulation value is the high altitude (2450 m) average for the Easton Glacier for the years 1990 to 1999 reported by Pelto (2000). By probing the glacier for the prior winter's snow depth and using crevasse stratigraphy, Pelto (2000) measured an average thickness in mid-August of 5.3 ± 2.2 m (3.1 ± 1.3 W.E.) of accumulated snow and ice for the years 1990-1999. The surface density at that elevation, measured in August 1999, a year of exceptional accumulation, was 600 kg/m^3 (Pelto, 2000). Pelto (2010; 2011) also reports ablation rates of 4.4 m/yr (W.E.) for the Easton Glacier averaged over the whole glacier (Pelto, 2000), measured in mid-August 1999. I therefore estimate the likely average thickness of accumulated snow at the start of the melting season on the Easton Glacier, at an altitude of 2450 m to ~ 9 m (5.3 ± 2.2 m + 4.4 m). Because Pelto's (2000) reported value is an average over nine years while that measured in Sherman Crater is for 2009, the second highest accumulation in 15 years, because Sherman Crater is at an elevation equivalent to the top of the accumulation zone for the Easton Glacier and because snow in Sherman Crater in late May is likely less compacted than that on the Easton Glacier in August (section 5.2.3), I expect the accumulation in Sherman Crater to be more than Pelto's (2000) reported measurement for the Easton Glacier. The minimum average accumulation measured in Sherman Crater of 6.8 ± 1 m is therefore likely an underestimate of an average full season's accumulation by at least several meters.

Pelto (2000) reports ablation rates of 4.4 m/yr (W.E.) for the Easton Glacier averaged over the whole glacier, measured in mid-August 1999, and 4.2 m/yr (W.E.) for the Rainbow Glacier measured at 1900 m, also in mid-August, and averaged for the years 1984 to 1999 (Pelto, 2011). For these water-equivalent values, Pelto (2010) assumes a density of 600 kg/m^3 . Assuming the same density, the ablation rate measured in Sherman Crater is 1.4 ± 0.6 m/yr (W.E.). This relatively low value reflects the position of Sherman Crater at an elevation near the top of the accumulation zone of both the Easton and Rainbow glaciers. Even the Rainbow Glacier ablation value, at an elevation of 1900 m, is 100-200 meters below the ELA for Mount Baker (Pelto and Hartzell, 2004; Kovanen and Slaymaker, 2005). It is therefore reasonable that the surface ablation in Sherman Crater is less than those reported for lower elevation glaciers.

Ablation estimates by Frank et al. (1977) for the glacier in quiescent pre-1975 Sherman Crater, based on field observations and photographs, range from 1 to 4 m (W.E) between April and August 1972. My 2009 ablation survey yields a range from 1 to 3 m (W.E) between June and August. Frank et al.'s estimated ablation values are greater than those recorded in 2009, but they also span two more months of melting. This discrepancy highlights the importance of considering the full ablation

and full accumulation season for the best accuracy in annual mass balance and heat flux calculations.

5.3.2 – WEATHER CONSIDERATIONS

The National Climatic Data Center lists 2009, the year during which ablation data were collected, as having the second hottest summer in the past decade (NOAA, 2009). Although final measurements of the ablation stakes were taken in early August, the first snow did not fall until in mid-November (Mountain News Corp., 2009) after several weeks of record-breaking temperatures in August (NOAA, 2010). The increase in surface melting recorded (from 3.5 cm/day before mid-July to 8.9 cm/day after mid-July; Table 3.1 on CD Appendix B) correlates with the observed increase in temperature during late July-early August. Assuming that the melting rate likely remained high for the remainder of August and average for the months that followed until the first snow, the total ablation for that particular summer could have been as high as 8.2 m (Table 3.1 on CD Appendix B), almost three times the ablation value used in this study.

The snow season that preceded the 2009 accumulation measurements was also exceptional, with the second highest snow water equivalent accumulation in 15 years (Snotel, 2011; Section 5.2.2). The last snow fell in early April, two months before our measurements. Assuming the melting rate observed for June-July also applies to the April-May period, the accumulation could have been as much as 8.8 m (Table 3.1 on CD Appendix B). Field observations suggest that the ablation in 2009 was such that it nullified the effects of an exceptional accumulation season: the glacier inside Sherman Crater was melted to a greater extent than is apparent on aerial photos from 2003 to 2008.

The annual mass-balance for the crater glacier for 2009 derived from these full-season estimates is only 0.6 m. In a typical year, however, the accumulation season for Sherman Crater lasts from approximately late September to early June, and the ablation season from mid-June to mid-September (Field observations, 2006-2010). The measurements collected in the crater therefore are more representative of typical accumulation and ablation seasons than these full season calculations for an exceptional year.

5.3.3 – RECOMMENDATIONS FOR MORE ACCURATE MASS BALANCE ESTIMATES

A solution to the problems inherent in calculating annual mass balance from accumulation and surface ablation measurements is to determine annual mass balance directly from snow and ice stratigraphy. This can be accomplished by measuring the thickness of seasonal layers related to

summer debris deposits exposed in fumarole pit walls and matching these layers to englacial reflectors in GPR profiles.

Welch et al. (2007) determined the annual mass-balance based of englacial reflectors in GPR profiles, but their success hinged on the presence of thick, well dated volcanic eruption deposit layers. The only volcanic event in recent history for Sherman Crater is the 1975 unrest event. Assuming an annual mass balance of ~ 4 m, even when considering deformation and thinning of the glacier, an eventual 1975 debris layer would likely be absent or near the base of the glacier and would therefore be unusable in the estimation of the glacier's annual mass-balance.

There are a few distinct englacial reflectors in both the 2009 and 2010 GPR data, but none that can be confidently matched across all profiles for the same year, or from year to year in those profiles collected along similar transects across the glacier. These data are not sufficiently consistent to yield a reliable annual-mass balance value. A higher frequency antenna would yield more detail related to englacial reflectors closer to the glacier surface, but could potentially miss the basal reflector. Sinisalo et al. (2003) suggest using radar layering (collection of data with various antenna frequencies over the same path and superimposing of the resulting transects) instead of ablation stakes measurements for the best accuracy. The logistics involved in using different radar frequencies in the crater, however, make this method impractical. Correlating annual layers in fumarole pits to radar transects is therefore most likely the best method to improve annual mass-balance data accuracy in Sherman Crater.

5.4 – HEAT FLUX

5.4.1 – ALTERNATE CALCULATIONS AND COMPARABLE VOLCANOES

Heat flux calculations depend primarily on accurate measurements of accumulation and surface ablation (and resulting annual mass balance) and on the estimated ice density for the crater glacier. The range of calculated heat fluxes for Sherman Crater based on alternate values for the annual mass balance (Section 5.3.2) and ice density (Section 5.3.3) values is ~ 4 - 37 W/m².

5.4.1.1 – Full accumulation and full ablation season

Compared to accumulation and ablation measurements on other glaciers on Mount Baker, values reported in this study are likely too low (Section 5.3.1). Estimated values for the full 2009 accumulation and ablation seasons yield values of 8.8 m and 8.2 m, respectively (Section 5.3.2). The resulting annual mass-balance is only 0.6 m. If this were the case every year, very little heat flux from the crater would be necessary to keep the glacier in dynamic equilibrium: ~ 4 W/m² (following

Welch et al., 2007) to $\sim 7 \text{ W/m}^2$ (following Frank et al., 1977). Such values are observed in other ice-filled calderas with active fumaroles, such as that at the summit of Mount Wrangell in Alaska (7 W/m^2 ; Clarke et al., 1989) and are only slightly lower than those calculated for pre-1975 Mount Baker ($7\text{-}11 \text{ W/m}^2$; Frank et al., 1977).

Because an annual mass-balance of 0.6 m is likely an underestimate of a typical annual mass-balance for the glacier inside Sherman Crater (Section 5.3.2), the resulting heat fluxes in the $\sim 4\text{-}7 \text{ W/m}^2$ range are probably too low for Sherman Crater.

5.4.1.2 – Pure ice basal density

Although in general glaciologic practice the annual-mass balance is calculated at the surface, in order for the glacier to remain in dynamic equilibrium while not overflowing the East Breach as observed in aerial photographs from 2003 to 2008, the yearly excess surface accumulation must be melted at the base. Considering an unlikely maximum ice density of 900 kg/m^3 at the base of the glacier (Section 5.2.3), $\sim 4.0 \text{ m}$ of ice measured at the surface represents a loss of $\sim 3.6 \text{ m}$ (W.E.), instead of 2.8 m (W.E.) when using a density of 700 kg/m^3 . The resulting heat flux ranges from $\sim 23 \text{ W/m}^2$ (following Frank et al., 1977) to $\sim 37 \text{ W/m}^2$ (following Welch et al., 2007). Heat fluxes in the range of $29\text{-}36 \text{ W/m}^2$ are typical of active hydrothermal vents in volcanic lakes (Shikano et al., 2004). Although a lake of boiling water formed in Sherman Crater in 1975, heat fluxes in the crater were then $\sim 150\text{-}200 \text{ W/m}^2$ (Frank et al., 1977). The heat flux in Sherman Crater is not currently sufficient to create a lake in the crater as it did in 1975. Meltwater has been traced to exit the crater, however, (Frank, 1975), so the absence of a lake in modern Sherman Crater does not disqualify the $\sim 23 \text{ W/m}^2$ to $\sim 37 \text{ W/m}^2$ range of alternate heat flux values.

Ice at the base of the crater glacier, however, is unlikely to have the density of pure ice (Section 5.2.3), so these values, particularly the $\sim 37 \text{ W/m}^2$ calculated following the method of Welch et al., (2007; Section 5.4.4), are likely overestimates of the actual heat flux in Sherman Crater.

5.4.1.3 – Comparable heat fluxes

Heat fluxes of $\sim 18\text{-}19 \text{ W/m}^2$ have been measured in quiescent but active craters such as the caldera on Mt. Veniaminof (19 W/m^2 ; Welch et al., 2007) and the summit crater of Mount Rainier ($\sim 18 \text{ W/m}^2$; Frank, 1995). The heat flux of $\sim 19 \text{ W/m}^2$ calculated following the method of Frank et al., (2007; Section 4.4.2.1) therefore seems a reasonable estimate for Sherman Crater. Because Frank (1975) deemed $\sim 18 \text{ W/m}^2$ to be a modest repose-period discharge for volcanoes in the Cascade Range, higher heat fluxes, such as the $\sim 28 \text{ W/m}^2$ value calculated following the method of Welch et al., (2007), therefore could also be reasonable for Sherman Crater.

Although alternate calculations yield a range of heat fluxes from $\sim 4\text{--}37\text{ W/m}^2$, I consider the $\sim 4\text{--}7\text{ W/m}^2$ sub-range to be likely an underestimate and the $\sim 28\text{--}37\text{ W/m}^2$ sub-range to be an overestimate of the actual heat flux in Sherman Crater. The $18\text{--}28\text{ W/m}^2$ sub-range seems the most likely to represent the heat flux in Sherman Crater based on calculations for other quiescent but active volcanoes in Alaska and the Cascade Range.

5.4.2 – USING THE WELCH ET AL. (2007) METHOD – VALIDITY OF ASSUMPTIONS

The Welch et al. (2007) glacier calorimetry model relies on a couple of assumptions: the entire ice-thickness is at the pressure melting point, all volume loss recorded in the caldera is the result of geothermal activity and all heat flux goes into melting ice (negligible loss through vents or otherwise). Because the crater glacier at Mount Baker consists of temperate ice, the first assumption is likely valid. The latter two assumptions, however, are probably inappropriate for Sherman Crater.

Not all volume loss from the crater glacier is the result of geothermal activity. Volume loss also results from surface melting, sublimation and from snowpack compaction. The volume loss at Mt. Veniaminof discussed in Welch et al.'s (2007) is the volume of ice that must melt for the caldera to remain in dynamic equilibrium, the annual mass-balance. Welch et al. (2007) relied on depths of dated englacial layers to determine the average annual mass balance. Because englacial annual layers represent the net difference between the full accumulation and the full ablation seasons, they yield exactly the volume that must be melted for equilibrium.

Englacial layers recorded by GPR in the Sherman Crater glacier were clearly not annual and could unfortunately not be dated; the annual mass balance was derived from measured surface accumulation and surface ablation. This introduces several sources of uncertainty in the calculations: my measurements at the surface of the glacier yield only part of the accumulation and the ablation seasons (Section 5.3.2) and no compaction data. These uncertainties in turn affect the calculated heat flux considerably: e.g., values from 4 W/m^2 to 37 W/m^2 based on alternate values (Section 5.4.1).

The glacier inside the caldera on Veniaminof extends from rim to rim except for a melt hole surrounding the active cone (Welch et al., 2007). The assumption that all heat flux goes into melting ice is appropriate in this setting. It is not for Sherman Crater: at least 30% of the crater (SWFF and NWFF) is snow free in summer with fumaroles venting to the air. If, as Frank et al. (1977) surmise, the location of fumaroles is controlled by concentric fractures related to the initial formation of the

crater, then the method ignores the part of the crater from which the majority of the heat flux emanates.

Because small uncertainties in mass balance and ice density measurements can considerably affect the calculated heat flux and because some of the basic assumptions required by the method are invalid in Sherman Crater, the method of Welch et al. (2007) seems ill-suited for this study.

5.4.3 – USING THE FRANK ET AL. (1977) METHOD – VALIDITY OF ASSUMPTIONS

The Frank et al. (1977) method does not depend on the assumption that all heat flux goes into melting ice, and the melting of the annual-mass balance only applies to the glacier-covered area. It is therefore better suited to the particular setting of Sherman Crater. Although the risk of introducing a large error in the calculations from an inaccurate measurement is lower than when applying the Welch et al. (2007) method, the potential for errors for each type of thermal ground and the interaction at their boundaries still exists.

For areas of type A, a standard value of 419 W/m^2 (White, 1969) was applied, but Frank et al. (1977) reported a heat flux for the Central Pit of 2400 W/m^2 . Although this value was collected in 1975 during the unrest event, it suggests that the rate of heat flow for areas of type A could be considerably larger (19 MW instead of 3 MW). With all other areas unchanged, the heat flux for the crater could be as high as $\sim 23 \text{ W/m}^2$ (instead of $\sim 19 \text{ W/m}^2$).

Areas of type B and C depend on annual accumulation and annual mass-balance, respectively. These values are in turn highly dependent on the weather, the timing of collection and the estimated ice density (Section 5.3). Despite these uncertainties, because the method is less reliant on measured mass-balance (only affects areas of type C) or ice density (only affects areas of type B and C) than that of Welch et al. (2007), it seems better suited to Sherman Crater. The heat fluxes calculated using this method are, however, likely underestimates of the actual values because the heat fluxes calculated for areas A and B are only the amount of heat required to melt snow, but venting to the air continues once the ground is bare.

5.4.4 – RECOMMENDATIONS FOR MORE ACCURATE HEAT FLUX CALCULATIONS

Although the Frank et al. (1977) method is well suited to Sherman Crater, the accuracy of the calculated heat flux could be greatly improved with a few changes to the data collection method.

A more detailed and precise map of the geothermal ground type distribution in Sherman Crater is essential. Although the map created in this study based on aerial photographs and field

observations is a good starting point, wide areas around approximate location of fumaroles and fumarole clusters were used for the calculations. Area f (Figure 4.3), for example, measures 1925 m² as drawn, based on visible steam on aerial photographs, but the actual vents in area f could cover only a few square centimeters based on the typical size of vents observed in the NWFF during gas sampling. Fieldwork dedicated to the geolocation and measurement of fumarole vents in the crater could greatly increase the accuracy in the estimated total heat flux for each type of area.

More accurate accumulation and annual-mass balance data are also needed. Accumulation should be measured closer in time to the last snow-fall and snow density measurements should be made at that time. Annual mass-balance would be better determined from snow and ice stratigraphy. This can be accomplished by correlating annual layers related to summer dust and debris deposits on fumarole pit walls to englacial reflectors in GPR profiles.

Finally, continued monitoring of the crater's heat flux would provide a set of data from which exceptional years and general trends could be identified.

5.5 – IMPLICATIONS

5.5.1 – *GLACIER CHARACTERISTICS*

My study provides the first rigorous quantitative assessment of the Sherman Crater glacier: its ice volume, flow direction and velocity, annual mass balance and characteristics of the material below its base. These constraints indicate that although, in the glacier's current state, an increase in volcanic activity similar to the 1975 unrest event would be unlikely to result in a significant hazard, this situation could change rapidly.

The ice volume measured in Sherman Crater (~1.3 and ~2.1 million m³ W.E. for 2009 and 2010, respectively) is less than in pre-1975, despite apparent similarities between values measured in Sherman Crater and those published by Frank et al. (1977). The entire volume measured in 2009 represents ~2/3 of the total ice lost during the 1975 event. Because even this large melt event did not produce a debris flow, it is therefore unlikely that, in the glacier's current state, an increase in heat flux similar to the 1975 event would produce a debris flow.

A comparison of volume estimates for two successive years, however, highlights the sensitivity of the glacier to short term weather patterns, in addition to long-term climate. The glacier mass appears to have grown by ~50% between 2009, a year with both an exceptionally high accumulation and hot ablation season, and 2010, a year with a slightly above average accumulation,

but exceptionally cold ablation season. As local climate changes in response to global conditions, the likelihood of such exceptional years could increase (Houghton et al., 1996). The glacier inside Sherman Crater could see dramatic changes in just a few years; it could completely disappear or it could grow to a size sufficient for meltwater-induced hazards to be significant. Such rapid changes have been observed on other Cascade volcanoes, such as the growth of the Crater Glacier on Mount St. Helens, which thickened at a rate of ~ 15 m/year at the onset of its formation (Walder et al., 2007).

If a combination of increased snowfall and reduced heat flux causes the Sherman Crater glacier to grow, the risk from meltwater-induced hazards would increase with or without sudden renewed volcanic activity. The effects of sudden renewed volcanic activity on a large glacier inside Sherman Crater could range from the creation of a lake of boiling water (e.g., 1975) to the generation of debris flows. If the volcano remains quiescent, as increased snowfall causes the crater glacier to grow, the areas characterized by different types of thermal ground in the crater would likely change. Areas that are currently bare year-round, particularly in the WRFF and NWFF, could become areas only exposed in the summer. The melting of the glacier in those areas, which is currently enhanced by the presence of dark bare ground year-round, could then diminish. The current mass-gradient driving the flow of ice northward could be overwhelmed by an eastward mass-gradient as ice flow towards the East Breach. The East breach has been the source of debris flows since the mid-Holocene ((Hyde and Crandell, 1978; Scott et al., 2003)), including 6 in the past 60 years (Gardner et al., 1995). Although these debris flows have been small, traveling only a few miles, Gardner et al. (1995) estimate the maximum credible volume of debris that could be entrained in a debris flow originating from Sherman Crater to be ~ 1 km³. A large eastward flowing glacier and associated eastward hydraulic head inside Sherman Crater could result in the saturation of the highly hydrothermally altered and pervasively fractured crater rim and produce potentially catastrophic debris flows down the Boulder Glacier towards dammed Baker Lake.

5.5.2 – HEAT FLUX

Despite the substantial uncertainties in my calculations, the range of values for the heat flux in Sherman Crater (~ 18 W/m² to ~ 28 W/m²) is the first estimate of heat flux for the crater since the unrest event of 1975. This range of heat flux calculated for 2009 suggests that the crater is currently more thermally active than it was before the 1975 unrest event, but still in the range for active yet quiescent volcanoes (Frank, 1995; Welch et al., 2007) and substantially less than that estimated for the 1975 event (Frank et al., 1977).

This interpretation is consistent with Crider et al.'s (2011) deduction that the prolonged degassing indicates connection to a deep magma source through a conduit opened in 1975. Heat flux in Sherman crater should be higher than prior to the opening of this conduit, but much lower than the initial 1975 pulse. If the new conduit is slowly being resealed, as waning gas emissions suggest (Crider et al., 2011), heat flux in Sherman Crater should also wane over time. Continued monitoring of heat flux in the crater is therefore essential in assessing changes in Mount Baker's magmatic and hydrothermal system.

The heat flux values presented in my study should provide researchers with an appropriate benchmark against which to compare future heat flux studies of Mount Baker and in the Cascade Volcanic Belt. In addition, my study provides a methodological foundation for studying other small active ice-filled craters. Either the glacier calorimetry method of Welch et al. (2007) or the thermal ground method of Frank et al. (1977) could be applied to other craters in which a volume of ice is largely contained with no outlet or with limited outlets through which ice outflow can be quantified. In the Cascade Range, Mt. Rainier and Mt. Adams in Washington and the South Sister in Oregon present such a situation. The method of Welch et al. (2007) is better suited to craters and calderas in which the ice extends rim to rim with minimal thermally exposed ground; the method of Frank et al. (1977) is best suited to craters with thermally exposed ground, whether year-round, in summer only, or both. Because calculations of annual mass-balance used in my study involve the use of Ground-Penetrating Radar, exceptionally high-altitude volcanoes, such as in the Andes, might prove untenable without greater logistics support.

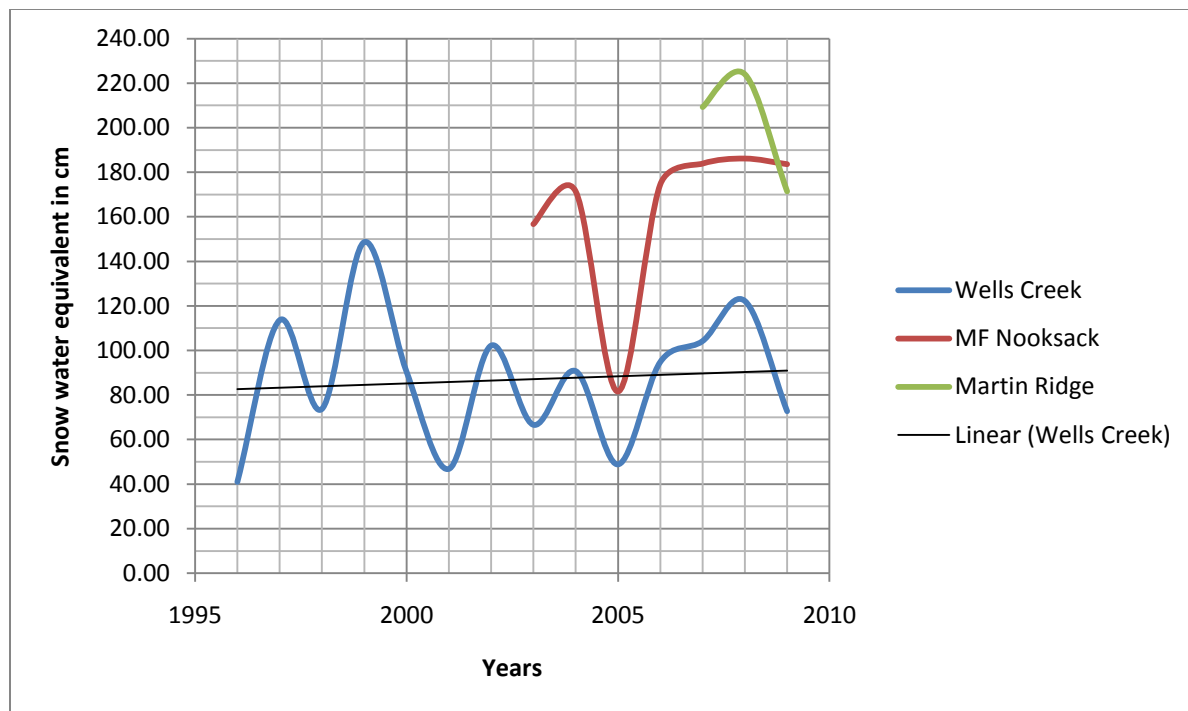


FIGURE 5. 1 – SNOW WATER EQUIVALENT ACCUMULATION FOR MOUNT BAKER

Snotel data for three stations surrounding Mount Baker. Wells Creek is located to the northwest, MF Nooksack is the station closest to the mountain and to the northeast, Martin Ridge is to the southeast (Snotel, 2011)

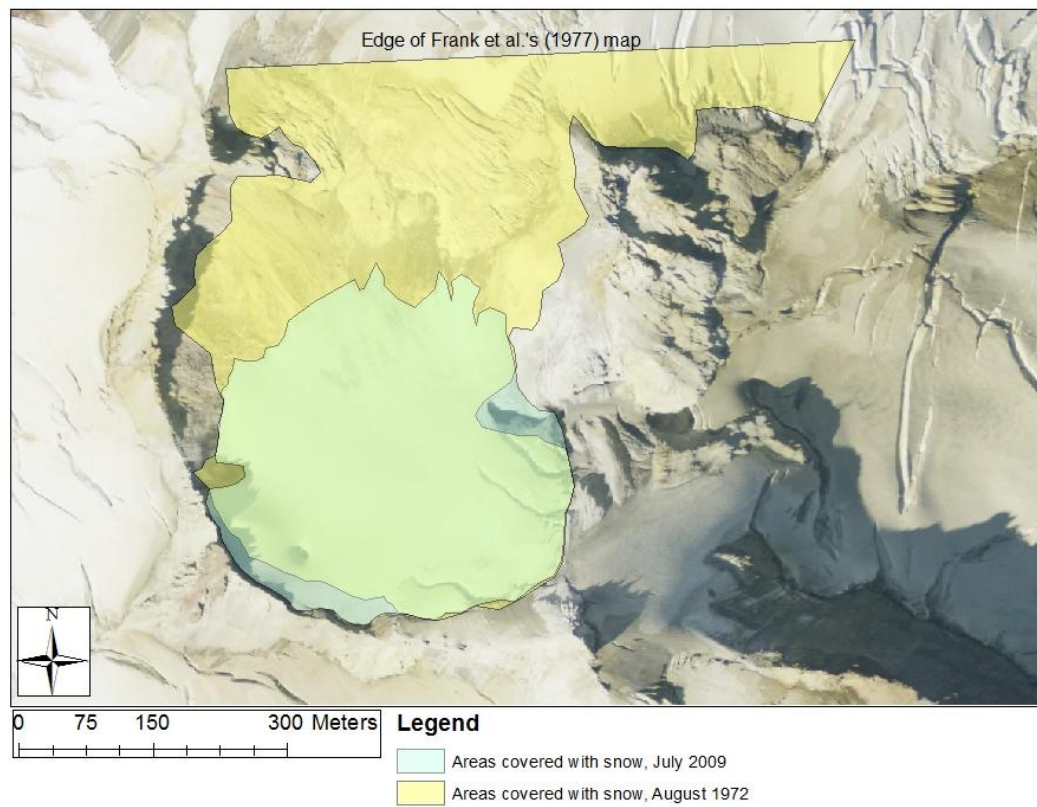


FIGURE 5. 2 – GLACIER SURFACE AREAS IN 1972 AND 2009

A comparison of areas covered in snow in August 1972 (in yellow) and in July 2009 (in blue) highlights the glacier's greater surface area in Frank et al.'s (1977) volume calculations.

6 - CONCLUSIONS

Although the glacier in Sherman Crater is affected both by climatic and geothermal conditions, the balance between the glacier's annual mass balance and the crater's heat flux have enabled the ice in Sherman Crater to remain in apparent dynamic equilibrium for almost a decade. The system's balance is delicate, however. As local climate changes in response to global conditions and as the active magmatic and hydrothermal system beneath Mount Baker evolves, conditions in the crater could change rapidly. My study provides a set of current characteristics for Sherman Crater and its glacier against which changes can be assessed.

The ice thickness and volume of the Sherman Crater glacier were derived from GPR data, providing the first look at the crater's subglacial topography and character. The CMP survey in the approximate center of the glacier suggests a layering of the ice with an upper section rich in air-inclusions and a water-saturated lower section. Survey of the glacier base further supports this hypothesis: most of the glacier rests on hydrothermally altered regolith interrupted by thin layers of meltwater, particularly near the center of the crater and near fumarole pits. Englacial reflectors with a positive polarity likely image buried summer accumulations of dust and debris. These reflectors are, however, too irregular and discontinuous to provide annual mass-balance constraints. Englacial reflectors with a negative polarity appear slightly above the inferred location for the base of the ice and likely represent ice caves and tunnels.

Despite uncertainties in the time-to-depth conversion, the maximum depth revealed in nine GPR profiles collected across the glacier likely approximate the true maximum depth more accurately than the sounding of open pits, which are unlikely to be located in the thickest part of the glacier. The set of ice thickness data derived from these GPR profiles also yields a more accurate estimate of the glacier's volume than the paraboloid approximation previously used in Sherman Crater.

In 2009, a year with an exceptionally high accumulation and an exceptionally hot summer, the maximum glacier depth was ~40 m (W.E), the area ~119000 m² and the volume ~1.3 million m³ (W.E), whereas in 2010, a year with a slightly below average accumulation and exceptionally cold summer, the maximum depth was ~66 m (W.E), the area ~125000 m² and the volume ~2.1 million m³ (W.E). The glacier's current extent, compared to the glacier's outline on Frank et al.'s (1977) map of Sherman Crater, suggests a lesser volume than prior to the 1975 unrest event. I conclude that the risk of a meltwater-induced hazards from Sherman Crater in the glacier's current state,

even if subjected to an increase in heat flux similar to the 1975 event, is low. The wide fluctuation in glacier volume between 2009 and 2010, however, highlights the potential for this situation to change rapidly.

The glacier's annual mass-balance, which must be melted at the base for the glacier to remain in dynamic equilibrium, is susceptible to exceptional years. In 2009, ~6.8 meters of new accumulation were measured in late May and ablation stakes were exposed by an average of ~2.8 meters by mid-August. Although these numbers do not take into account the full accumulation and ablation for 2009, 2009 was exceptional. Because the accumulation season for Sherman Crater typically lasts from late September to early June, these measured data are likely more representative of typical accumulation and ablation data than the estimates for the full 2009 seasons. The derived annual mass-balance of ~4.0 m/yr is therefore likely more accurate than the full-season alternate estimate of 0.6 m/yr. In addition, the surface melting appeared more extensive in Sherman Crater in 2009 than in prior years. Given this apparent greater than normal surface ablation, the value calculated for 2009 probably underestimates the long-term average of basal melt.

The annual-mass balance affects the extent of different types of thermal ground in Sherman Crater. In its current state, because much of the heat flux is concentrated in the WRFF and the NWFF, the northern part of the crater is snow-free in the summer with many subareas snow-free year-round. Higher melting of the glacier in this part of the crater causes a mass gradient in the glacier that drives ice flow northward at an average velocity of 3.0 ± 1.8 m/day. If the annual mass-balance increases or the heat flux decreases, the excess snow and ice would eventually cover much of the northern fumarole fields. The current mass-gradient driving the flow of ice northward could be overwhelmed by an eastward mass-gradient. In addition to the threat posed by a more massive glacier in terms of meltwater-volume, excess snow and ice would likely flow towards the East Breach, the lowest point on the crater rim and a source of debris flow since the mid-Holocene. Water saturation of the hydrothermally altered and fractured crater rim material could increase its susceptibility to fail. The concern of an increase in potential hazard from debris flow to downstream communities and reservoirs is therefore greater if the heat flux decreases (e.g., from the release of a conduit to a magma source at depth) or the annual mass-balance increases (e.g., from greater precipitation at higher elevation due to climate change).

The heat flux measured in Sherman Crater, based on 2009 glaciological data, yields a likely range of ~18-28 W/m². The crater therefore appears more thermally active than it was pre-1975, but substantially less than during the 1975 unrest event. Based on geophysical and geochemical studies

of Sherman Crater over the past three decades, Crider et al. (2011) concluded that the 1975 event resulted from opening of a conduit to a deep source of volatiles. The high heat fluxes measured in Sherman Crater in 1975 likely correspond to the initial release of volatiles as this conduit initially opened (Crider et al., 2011). The range of heat fluxes calculated for Sherman Crater in 2009 suggests continued connection to a heat source. If the new conduit is slowly being resealed, as waning gas emissions suggest (Crider et al., 2011), heat flux in Sherman Crater should decrease over time. As discussed above, a decrease in heat flux could lead to an increase in the potential hazard from debris flows to downstream communities and reservoirs. Sherman Crater might therefore become more of a threat if volcanic activity subsides.

Continued monitoring of Sherman Crater's heat flux is therefore recommended. When thermal-infrared imagery is unavailable and direct measurements impractical, heat flux calculations derived from glaciologically-based methods can provide an important set of data from which exceptional years and general trends can be identified.

REFERENCES

- Baker G.S., T.E. Jordan, J. Pardy, 2007, An introduction to Ground Penetrating Radar (GPR). Geological Society of America Special Paper 432: 1-18
- Benson C.S., D.K. Bingham, G.B. Wharton, 1971, Glaciological and volcanological studies at the summit of Mt. Wrangell, Alaska. Snow and Ice-Symposium - Neiges et Glaces (Proceedings of the Moscow Symposium). IAHS-AISH Publ. No. 104
- Bradford, J. H., J. Nichols, T. D. Mikesell, J. T. Harper, 2009, Continuous profiles of electromagnetic wave velocity and water content in glaciers: An example from Bench Glacier, Alaska, USA, *Annals of Glaciology*, 50, 1–9.
- Burger R.H, A.F. Sheehan C.H. Jones, 2006, Introduction to Applied Geophysics. Published by W. W. Norton, 600 p.
- Caplan-Auerbach, J., W.A. Thelen, S.C. Moran, 2009, An Unusual Cluster of Low-Frequency Earthquakes at Mount Baker, Washington, as Detected by a Local Broadband Network, *Eos Trans. AGU*, 90(52), Fall Meet. Suppl., Abstract V23D-2111
- Clark, G.K.C., G.M. Cross, C.S. Benson, 1989. Radar imaging of glaciovolcanic stratigraphy, Mount Wrangell Caldera, Alaska; interpretation model and results. *Journal of Geophysical Research*, 94(B6): 7237-7249.
- Crider, J., K. Hill-Johnsen, G. Williams-Jones, 2008, Thirty-year gravity change at Mount Baker volcano, Washington, USA: extracting the signal from under the ice; *Geophysical Research Letters* 35: L20304-8.
- Dehn J., K. Dean, K. Engle, 2000, Thermal monitoring of North Pacific Volcanoes from space. *Geology*, v.28; p.755-758.
- Easterbrook, D., 1975, Mount Baker eruptions: *Geology*, v. 3, p. 679-682
- Eder K., C. Reidler, C. Mayer, M. Leopold, 2008, Crevasse detection in alpine areas using Ground penetrating Radar as a component for mountain guide system. *The International Archives of the Photogrammetry. Remote Sensing and Spatial information Sciences*. Vol XXXVII. Part B8.
- Ewert, J. W., M. Guffanti, T.L. Murray, 2005, An assessment of volcanic threat and monitoring capabilities in the United States: Framework for a National Volcano Early Warning System (NVEWS), US Geological Survey Open-File Report 2005-1164, 62 pp., 2005.
- Frank, D., 1975, Subglacial transfer of geothermal fluids in Boulder Glacier, Washington. *EOS*, v. 57 no. 2, p87.
- Frank, D., M.F. Meier, D.A. Swanson, 1977, Assessment of increased thermal activity at Mount Baker, Washington, March 1975-March 1976. U. S. Geological Survey Professional Paper, Report: P 1022-A: 49.
- Geophysical Survey Systems, Inc. (GSSI), 2004, Radan 6 User's Manual, MN43-171 Rev. Published by Geophysical Survey Systems, Inc., North Salem, NH 03073-0097.

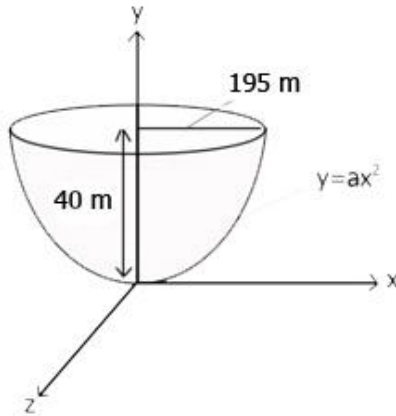
- Guðmundsson, M.T., D. Högnadóttir, A.B. Kristinsson, S. Gudbjörnsson, 2007, Geothermal activity in the subglacial Katla caldera, Iceland, 1999–2005, studied with radar altimetry. *Annals of Glaciology*, 45, 66–72
- Gusmeroli, A., T. Murray, B. Barrett, R. Clark, and A. Booth, 2008, Estimates of water content in glacier ice using vertical radar profiles: a modified interpretation for the temperate glacier Falljokull, Iceland. *Journal of Glaciology*, 54, 188, 939–942.
- Hodge, B.E., 2008. Characterizing surface deformation from 1981 to 2007 on Mount Baker Volcano, Washington (M.S. thesis): Bellingham, Western Washington University, 127 p.
- Hodge, B. and J. Crider, 2010, Investigating mechanisms of edifice deflation, 1981–2007, at Mount Baker volcano, Washington, United States: *Journal of Geophysical Research*, vol. 115, B04401.
- Houghton, J.T., Intergovernmental Panel on Climate Change, 1996, Climate Change 1995: The Science of Climate Change. Cambridge, UK: Cambridge University Press.
- Hildreth, W., J. Fierstein, M. Lanphere, 2003, Eruptive history and geochronology of the Mount Baker volcanic field, Washington. *Geological Society of America Bulletin*, 115: 729–764.
- Hubbard B. and N. Glasser, 2005, Field Techniques in Glaciology and Glacial Geomorphology. Chichester: John Wiley & Sons, Ltd. 400 pp.
- Hyde, J.H., D.R. Crandell, 1978, Postglacial volcanic deposits at Mount Baker, Washington, and potential hazards from future eruptions: U.S. Geological Survey Professional Paper 1022-C, 17 p.
- Jacobel, R., 1982, Short-term variations in velocity of South Cascade glacier, Washington, USA. *Journal of Glaciology*. Vol. 28, no. 99
- Kay, J.E., 2006, Snow density observations in the Washington Cascades. Presentation, 75th Annual Western Snow Conference, Las Cruces, NM.
- Kiver, E.P., 1978, Mount Baker's changing fumaroles. *Ore Bin*, 40: 133–145.
- Kovanen, D., O. Slaymaker, 2005, Fluctuations of the Deming Glacier and theoretical equilibrium line altitudes during the late Pleistocene and early Holocene on Mount Baker, Washington, USA: *Boreas*, vol.34, no.2, pp.157–175
- Malone, S., 1979, Gravity changes accompanying increased heat emission at Mount Baker, Washington: *Journal of Volcanology and Geothermal Research*, vol.6, no.3–4, pp.241–256.
- Muir, J., 1873, On actual glaciers in California. *American Journal of Science and Arts, Third Series*, v:69–71
- NOAA, National Weather Service Forecast Office, Seattle, WA, 2010. <http://www.wrh.noaa.gov/sew/09-pns.pdf>. Created January 2010. Retrieved 02/11/2011
- NOAA, National Climatic Data Center, 2009. <http://www.ncdc.noaa.gov/oa/ncdc.html>. Last Updated 08/26/2009. Retrieved 02/15/2011
- Nye J.F., 1952, The mechanics of glacier flow. *Journal of Glaciology*, Vol. 2, Issue 12, pp.82–93

- Pelto, M.S., 2000, Summer snowpack variations with altitude on Mount Baker, Washington 1990–1999: a comparison with record 1998/1999 snowfall. In Hardy, J.P. and J. Pomeroy, eds. Proceedings of the 57th Annual Eastern Snow Conference, 17–19 May 2000, Syracuse, New York. Hanover, NH, US Army Cold Regions Research and Engineering Laboratory, 79–84.
- Pelto M.S., P.L. Hartzell, 2004, Change in longitudinal profile on three North Cascades glaciers during the last 100 years. *Hydrological Processes* 18: 1139– 1146
- Salamatin, A.N., Y.D. Murav'yev, T. Shiraiwa K. Matsuoka, 2000, Modeling dynamics of glaciers in volcanic craters. *Journal of Glaciology*, 46 (153), 177-187.
- Shikano S., E. Kikuchi, S. Takagi S., H. Doi, 2004, Volcanic heat flux and short-term molomixis during the summer stratification period in a crater lake. *Limnology and Oceanograph*. Vol. 49, No. 6, pp. 2287-2292
- Sinisalo, A., A. Grinsted, J.C. Moore, E. Kärkäs and R. Petterson, 2003, Snow accumulation studies in Antarctica with ground penetrating radar using 50, 100 and 800 MHz antenna frequencies. *Annals of Glaciology*, 37, 194-198.
- SNOTEL Washington. United States department of agriculture, National water and climate center. <http://www.wcc.nrcs.usda.gov/snotel/Washington/washington.html>. Retrieved 05/01/2011
- Scott, K.M., D.S. Tucker, D.S., J. McGeehin, 2003, Holocene History of Mount Baker volcano, North Cascades: XVI INQUA Congress Program with Abstracts, p. 51
- Tabor, R.W., R.A. Haugerud, W. Hildreth, E.H. Brown, 2003, Geologic map of the Mount Baker 30 × 60 minute quadrangle, Washington: U.S. Geological Survey. Map I-2660, scale 1:100,000, 2 sheets.
- Tucker, D.S., K.M. Scott, D.R. Lewis, 2007, Field guide to Mount Baker volcanic deposits in the Baker River valley: Nineteenth century lahars, tephra, debris avalanches, and early Holocene subaqueous lava, in *Floods, Faults, and Fire: Geological Field Trips in Washington State and Southwest British Columbia: Geological Society of America Field Guide* 9, p. 83-98.
- Walder, J.S., S.P. Schilling, J.W. Vallance, R.G. LaHusen, 2007, Emplacement of silicic lava dome through a crater glacier, Mount St. Helens, 2004-2006. *Annals of Glaciology*. Vol. 45, pp. 14-20
- Welch, B.C., K. Dwyer, M. Helgen, C.F. Waythomas, R.W. Jacobel, , 2007. Geophysical survey of the intra-caldera icefield of Mt. Veniaminof, Alaska. *Annals of Glaciology*, 45: 58-65.
- Werner, C., W. Evans, M. Poland, D. Tucker, M. Doukas, 2009, Long-Term Changes in Quiescent Degassing at Mount Baker Volcano, Washington, USA ; Evidence for a Stalled Intrusion in 1975 and Connection to a Deep Magma Source: *Journal of Volcanology and Geothermal Research* vol 186 n. 3-4 pp. 379-386.

APPENDIX A -

CRATER GLACIER VOLUME USING A PARABOLOID APPROXIMATION

Example for 2009, water-equivalent ice volume.



We fit a paraboloid to the known quantities: glacier crater radius and maximum water equivalent ice depth.

Glacier crater radius:

Glacier area, measured in ArcGIS: 119,000 m²

$$\pi r^2 = 119,000$$

$$r = \sqrt{\frac{119000}{\pi}} \cong 195 \text{ m}$$

Maximum water equivalent ice depth

Maximum depth measured in GPR profile: 58 ± 5 m.

Assuming a density for the ice pack of 700 kgm⁻³ (Frank, 1977), the water-equivalent max depth is ~40 m ± 4 m

- 1) Find a, in the parabola equation $y = ax^2$

$$40 = a(195^2) \Rightarrow a = 40/(195^2) \Rightarrow y = 40/(195^2) x^2$$

- 2) Find the equation of the glacier surface area for any given depth x

$$A(y) = \pi x^2 \Rightarrow A(y) = \pi((195^2)/40)y$$

- 3) Integrate the area over the range of depths: $V(y) = \int_{bottom}^{top} A(y) dy$

$$V = \int_0^{40} \pi((195^2)/40)y dy = \pi((195^2)/40) \int_0^{40} y dy \rightarrow V = 2.4 \text{ million m}^3$$

- 4) Uncertainty

The water equivalent max depth is ±4 m, based on potential errors in picking the depth in Radan. The radius was calculated from an assumed circular surface of 119,000 m². The glacier, however, is not perfectly spherical; its edges are irregular and its overall shape more of an oval than a circle (with a length of 430 m along its major axis and 340 m along its minor axis as measured in ArcGIS). When the surface area is measured to include all outward protruding edges, it can be as much as 126,000 m² (radius of 200 m). When the protruding edges of the glacier are excluded, its surface area can be as small as 112,000 m² (radius of 188 m).

This yields a range of volumes from ~2.0 million m³ (radius 188m, depth 36 m) to ~2.8 million m³ (radius 200m, depth 44 m). The crater glacier volume is therefore:

V = 2.4±0.4 million m³. I use this range of error for other volume calculations